Experimental Study on Turbulence Intermittency with Microwave Reflectometer in a Linear Magnetized Plasma

張, 博宇

https://doi.org/10.15017/2534474

出版情報：Kyushu University, 2019, 博士（工学）, 課程博士
バージョン：
権利関係：

Experimental Study on Turbulence Intermittency with Microwave Reflectometer in a Linear Magnetized Plasma

Boyu Zhang

Interdisciplinary Graduate School of Engineering Sciences
Kyushu University
2019

Abstract

This thesis aims to study the intermittent turbulence feature in a linear magnetized laboratory plasma with newly developed microwave reflectometer. Turbulence intermittency, which is enhanced particle bursts propagating across the open magnetic field region, has been observed and studied during the past three decades. The intermittency has significant impacts on controlling fusion and industrial plasmas and on understanding astrophysical phenomena. However, the generation mechanism of turbulence intermittency is still unknown. The purpose of this thesis is to have a better understanding of turbulence intermittency in a laboratory magnetized plasma.

To realize this purpose, turbulence experiment is performed in a linear magnetized plasma device, PANTA. In order to detect the turbulence intermittency, multi-point density measurement with high temporal and spatial resolution is required. Therefore, two microwave reflectometers, frequency comb reflectometer and comb sweep reflectometer, are newly developed. The comb reflectometer is used to detect density fluctuations at many different radii simultaneously. The comb sweep reflectometer is developed for equilibrium density profile measurement.

A frequency comb microwave reflectometer has been installed in PANTA, which has a frequency range from 12 GHz to 26 GHz with a

frequency interval of 0.5 GHz. This reflectometer can measure density fluctuation at 29 radial positions simultaneously with 1 μs temporal resolution and 0.5 mm radial resolution. A comb sweep microwave reflectometer is developed to eliminate the half-wavelength uncertainty while reconstructing the density profile. This system covers a frequency range from 15.5 GHz to 26 GHz with 17 channels. Each channel sweeps a frequency range of around 0.4 GHz with a sweep period of 2 μs and the repetition frequency is 0.5 GHz. This system is succeeded in reconstructing the radial profile of electron density, which is consistent with that measured by the Thomson scattering system.

A global turbulence intermittency is observed with microwave reflectometers and characterized by the statistical analysis in PANTA for the first time. A quasi-coherent density fluctuation is excited locally in the region of $r = 3 - 4.5\ \mathrm{cm}$, where the density gradient is largest. Intermittent events are observed in the whole radial region of plasma. Conditional averaging reveals that positive and negative density bursts are driven at the outer and inner radial regions, respectively. The inversion layer is located at around $r = 4$ cm. The positive density bursts propagate from the quasi-coherent fluctuation region to peripheral region with a velocity of approximately 1.0 km/s and have a large radial scale. The exponentially decaying auto-correlation function and large Hurst exponents (>0.5) of the perturbation at the quasi-coherent fluctuation

region reveal that the intermittent bursts have long-range time correlation. The waiting time for large bursts follows power-law distribution. The power spectrum of fluctuation shows a $1/f$ -scale at intermediate frequency range. These evidences indicate the existence of self-similar behavior and self-organized criticality (SOC) dynamics. The long-range radial correlation is observed across the inversion layer at the quasi-coherent fluctuation frequency. Cross-bicoherences of the density fluctuation at different radii show the strong nonlinear three-wave coupling between the quasi-coherent fluctuation and micro-turbulence not only across the inversion layer but also far away from the quasi-coherent fluctuation region.

The generation mechanism of observed global intermittency is discussed. The quasi-coherent fluctuation, which is driven by the large density gradient, perturbs the background density. The positive and negative density bursts are generated and propagate outward and inward, respectively, due to the SOC dynamics. Because of the nonlinear three-wave coupling with the quasi-coherent fluctuation, the distant turbulence is modulated and enhances the propagating density burst. The radial-scale of the propagation is thus elongated and the global intermittency is formed.

Contents

Abstract i

Chapter 1 Introduction 1

1.1 Magnetic confinement fusion...2

1.2 Turbulence intermittency in magnetized plasma 4

1.2.1 Definition and characteristics of turbulence intermittency 4

1.2.2 Effects of turbulence intermittency................................7

1.2.3 Generation mechanisms of turbulence intermittency 8

1.3 Purpose of this thesis..14

Chapter 2 Development of microwave reflectometer diagnostics in PANTA 16

2.1 Introduction of PANTA...16

2.2 Microwave in plasma..19

2.2.1 Dispersion equations..19

2.2.2 Wave scattering and Doppler shift...............................21

2.3 Development of frequency comb microwave reflectometer in PANTA..24

2.3.1 Introduction of frequency comb microwave reflectometer 24

2.3.2 System design and signal processing...........................27

2.3.3 Benchmark test 31

2.3.4 Density profile reconstruction 32

2.3.5 Density perturbation measurement 34

2.3.6 Azimuthal velocity measurement 36

2.4 Development of frequency comb sweep microwave reflectometer in PANTA 38

2.4.1 Introduction of frequency modulation continuous wave reflectometer 38

2.4.2 System design and signal processing 41

2.4.3 Benchmark test 45

2.4.4 Density profile reconstruction 46

Chapter 3 Development of data analysis methods for turbulence intermittency study 48

3.1 Spectral analysis 48

3.1.1 Fourier transform 49

3.1.2 Auto-power spectrum 50

3.1.3 Cross-power spectrum and cross-coherence 52

3.1.4 Bispectrum and bicoherence 55

3.2 Hilbert Transform 58

3.3 Long-range correlation analysis 60

3.3.1 Auto-correlation function 60

3.3.2 R/S analysis 61

3.3.3 Structure functions analysis 63

3.4 Conditional averaging 64

3.4.1 Threshold method 65

3.4.2 Template method 65

Chapter 4 Study of Turbulence intermittency 67

4.1 Quasi-coherent fluctuation condition 68

4.2 Evaluation of intermittency 73

4.2.1 Spatial-temporal evolution of intermittency 73

4.2.2 Long-range correlation of intermittency 80

4.2.3 Discussion 84

4.3 Ambient turbulence behaviors and nonlinear coupling 86

4.3.1 Turbulence envelope behaviors 87

4.3.2 Nonlinear three-wave coupling between quasi-coherent fluctuation and turbulence 90

4.3.3 Discussion 92

4.4 Conclusion 92

Chapter 5 Summary 94

Acknowledgement 98

Bibliography 100

Appendix 108

Chapter 1

Introduction

Nowadays, the energy problem is becoming a global issue. The most common energy source in the world today is fossil fuels, such as oil, coal and natural gas, which cause several problems. On the one hand, the demand for energy is now rapidly increasing, especially in less developed countries, while the fossil fuels are unrenewable and their reserves are finite. It is reported that at the current rate of human consumption of energy, the oil will be exhausted in 40 years, and that figure is 50 years for natural gas and 250 years for coal [1]. On the other hand, the environment problems caused by the use of fossil fuels are getting more serious, especially the global warming problem [1]. Therefore, developing a renewable and clean energy source is becoming more urgent.

Controlled nuclear fusion is regarded as the most viable next-generation energy source, which has lots of advantages compared with other new energies. Controlled nuclear fusion is much more abundant than other energy sources. For example, fusion reaction releases nearly four million times more energy than chemical reaction and four times more energy than fission reaction with the same mass of fuel [2]. Besides, the fuels of controlled nuclear fusion, deuterium and tritium, can be extracted from seawater and produced from lithium through nuclear conversion, respectively. The energy released by the fusion reaction of deuterium contained in 1 liter of seawater is equal to the energy produced by the combustion of 300 liters of gasoline [3], which means the fusion fuels are almost limitless. Furthermore, controlled nuclear fusion is clean and safe, which produces no greenhouse gases or long lived nuclear waste, and has little risk of a meltdown scenario. Thus, the development of controlled nuclear fusion is strongly required.

1.1 Magnetic confinement fusion

Controlled nuclear fusion is the reaction in which several light atomic nuclei are combined to form heavier nuclei and release energy due to mass defect. The best proposal for future fusion reaction is D-T reaction [4], which means the fuels are deuterium and tritium,

$$ {}_1\mathrm{D}^2 + {}_1\mathrm{T}^3 \rightarrow {}_2\mathrm{He}^4(3.5\ \mathrm{MeV}) + {}_0\mathrm{n}^1(14.1\ \mathrm{MeV}) \tag{1.1} $$

To realize the fusion reaction, fuels are required to be ionized and become plasma. The ignition condition for controlled fusion is known as Lawson criterion [5], which requires that the plasma has a high temperature (~10 keV), high density (~10^{20} m^{-3}) and long confinement time (~1 s).

There are two methods to confine plasma. The first method is called inertial confinement, which is to compress the fuel strongly to reach ignition condition by inertia. The second method is magnetic confinement, which is to confine plasma with the Lorentz force of the magnetic field.

Magnetic confinement fusion has been widely studied for around 70 years and been proved to be the most likely way to realize controlled fusion.

According to the different configurations of magnetic field, there are different types of magnetic confinement devices, e.g. magnetic mirror, stellarator, tokamak, etc. Among all the devices, tokamak is considered to be the most promising device for obtaining net energy output. To promote research on tokamak plasma, an international project, International Thermonuclear Experimental Reactor (ITER) project (shown as Fig. 1.1) was established in 1985. The ITER device is now under construction in France and is planned to achieve first plasma in 2025 [6], which is expected to realize a Q value of 10, where Q is the energy gain factor.

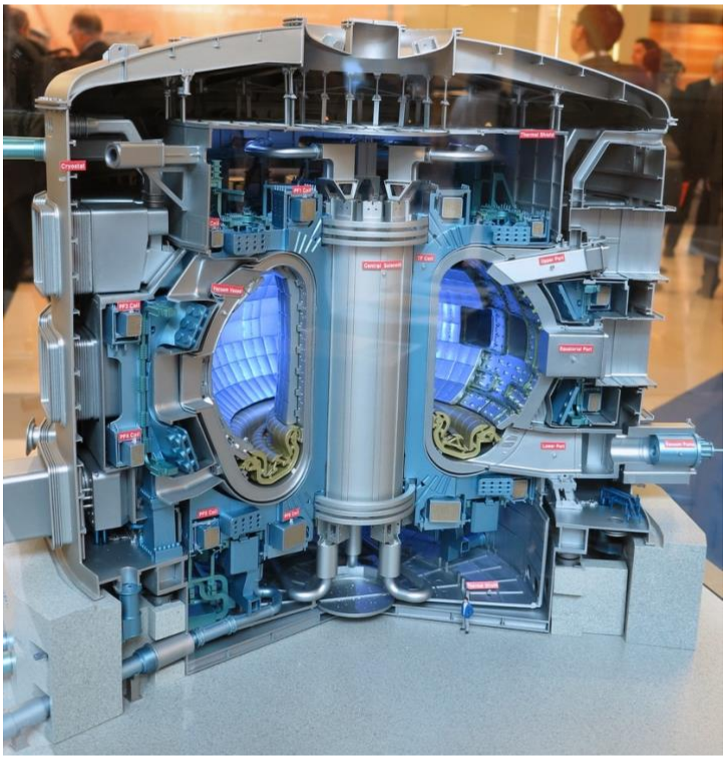

Figure 1.1: The schematic of ITER [7].

However, it is difficult to keep good confinement of plasma and realize the ignition condition, as turbulence increases the radial transport and disturb the confinement. Since more than 30 years ago, a radial convection of coherent plasma structure, intermittency [8, 9], has drawn attention. As mentioned in next section, intermittency is widely observed in different devices and destructs the plasma confinement. Thus, a lot of researches have been conducted on turbulence intermittency.

1.2 Turbulence intermittency in magnetized plasma

1.2.1 Definition and characteristics of turbulence intermittency

Turbulence intermittency, also called as ‘blobs’, ‘filaments’ or ‘avaloids’ [10], has been studied during the last two decades. A simplified robust theoretical mechanism for intermittency generation is as follows [11, 12]. A filament of enhanced density is formed firstly and then polarized by a net species-summed force $\vec{b} \cdot \nabla \times \vec{F}$ $(\neq 0)$, where $\vec{b} \equiv \vec{B}/B$ is the unit vector along magnetic field $\vec{B}$, and $\vec{F}$ is an arbitrary force density. Some examples for $\vec{F}$ are the curvature and ∇B forces, centrifugal force and neutral wind frictional force [13]. After charge polarization, a poloidal electric field is formed inside the filament, and the whole filament is drift by the $\vec{E} \times \vec{B}$ force. Thus, the definition of an intermittency from the ideal theory is the structure that has the following properties [12],

i) it is a single peak with the value higher than the root-mean-square

(RMS) of the background fluctuation;

ii) the variation of the structure vertical to the magnetic field is much stronger than that in the parallel direction;

iii) the radial propagation is dominated by the $\vec{E} \times \vec{B}$ velocity due to the charge-polarizing force.

Experimentally, intermittency has been widely observed in different devices, including tokamaks [10, 14–25], stellarators [26–28], linear devices [29, 30], reserved-field pinch [31], basic toroidal devices [32, 33], and even in space plasma [34, 35]. For example, Figure 1.2 shows the 2-D density fluctuation obtained with beam emission spectroscopy (BES) system in DIII-D, where red parts indicate high density and blue low density. The radially outward propagation of enhanced density is clearly observed with a velocity of 1.5 km/s [15].

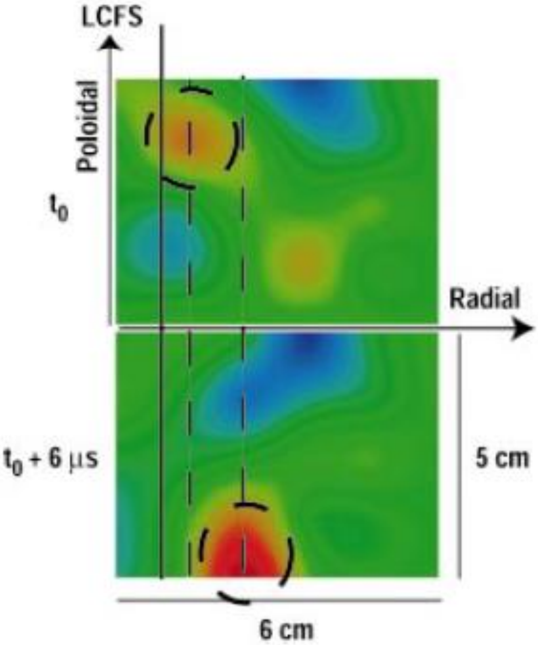

Figure 1.2: The 2-D plots of electron density from BES in DIII-D Tokamak, which shows an outward motion of high density (red) [15].

Because of the density burst, the probability distribution function (PDF) is deviated from Gaussian function. Figure 1.3 shows results from HL-2A Tokamak [22]. The blue lines in the left are temporal evolutions and PDFS of ion saturation current around the last closed flux surface (LCFS), and the red dots are Gaussian fitting for the PDF. It is clear that inside the LCFS, there are more negative burst events (also called as density holes), resulting to the PDF dominated by negative values. It shows an opposite result out of the LCFS, where bursts are positive and positive values are dominant in the PDF. The turning point is located a little inside the LCFS where the PDF is close to Gaussian distribution. To evaluate the deviation of distribution, skewness and kurtosis (see section 4.3) are calculated and the profiles are shown in the right of Fig. 1.3. The skewness and kurtosis tend to increase from the edge to far SOL, indicating the fluctuation at far SOL is dominated by the density bursts. This result agrees with that of the most devices.

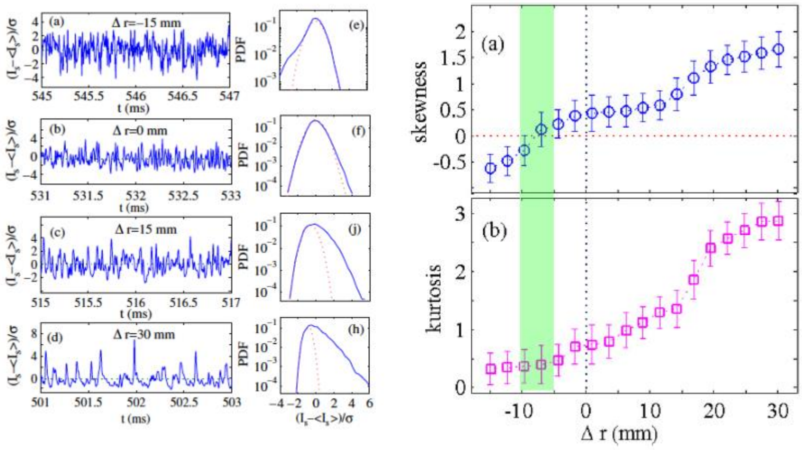

Figure 1.3: The temporal evolution and distribution of ion saturation current (left) and the radial profiles of skewness and kurtosis of PDF (right) [22].

1.2.2 Effects of turbulence intermittency

The direct effect of the turbulence intermittency is the increase of non-diffusive radial particle transport. Figure 1.4 shows that the ratio of the flux caused by intermittent events detected with a threshold of $2.5 \times \mathrm{RMS}$ (see subsection 3.4.1) to the total $E_\theta \times B_T$ flux in TEXTOR is around 40%, and the contribution of the intermittency in the open magnetic field region is larger than that inside LCFS [10]. As the result, if the cross-field particle flux is sufficiently large compared with the particle flow along field lines into the divertor volume, the “main chamber recycling regime” [36, 37] will be dominant, and the profiles of electron density and temperature in SOL are flattened while core density increases, as shown in Fig. 1.5 [38]. All these phenomena will result in the increase of unwanted interaction with limiters, radio frequency antennas [12] and the enhanced erosion of the wall [10, 39].

Besides, intermittency can also increase the interaction of plasma with the far SOL [40, 41], affecting the SOL width [23]. Furthermore, the intermittent convective transport is also found to have an influence on the density limit in some tokamaks [42]. Thus, a full understanding of intermittency generation mechanism is necessary.

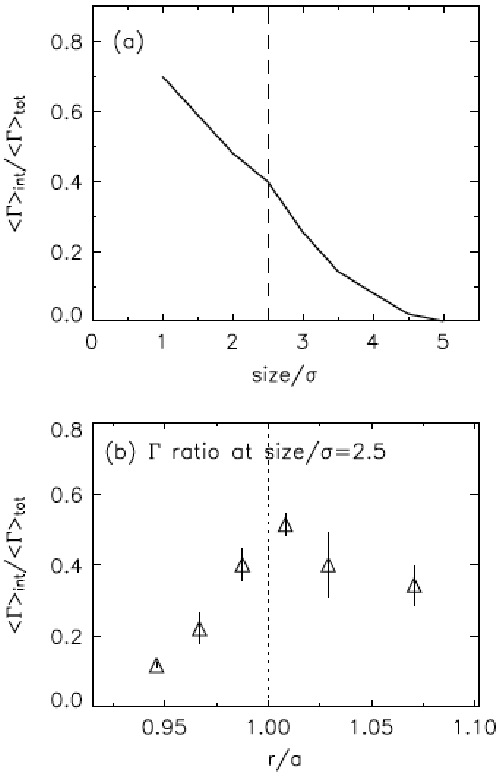

Figure 1.4: The ratio of the intermittent particle flux to the total $E_\theta \times B_T$ flux in TEXTOR [10].

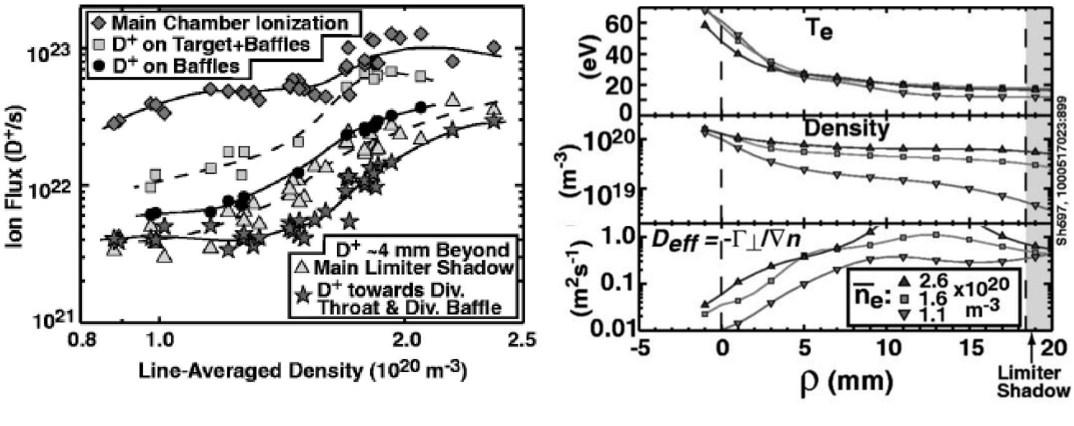

Figure 1.5: Main chamber recycling regime (left) and the flat profiles of electron density and temperature in SOL (right) in C-MOD [38].

1.2.3 Generation mechanisms of turbulence intermittency

Because of its significant influence on edge transport and confinement of plasma, it is necessary to understand the generation process of the turbulence intermittency. By now, different mechanisms have been proposed to interpret the formation of the intermittent structures, such as SOC dynamics [10, 12, 17, 31], interchange mode [32], coherent structures [33, 43], zonal flow [19] and others [17, 24, 25].

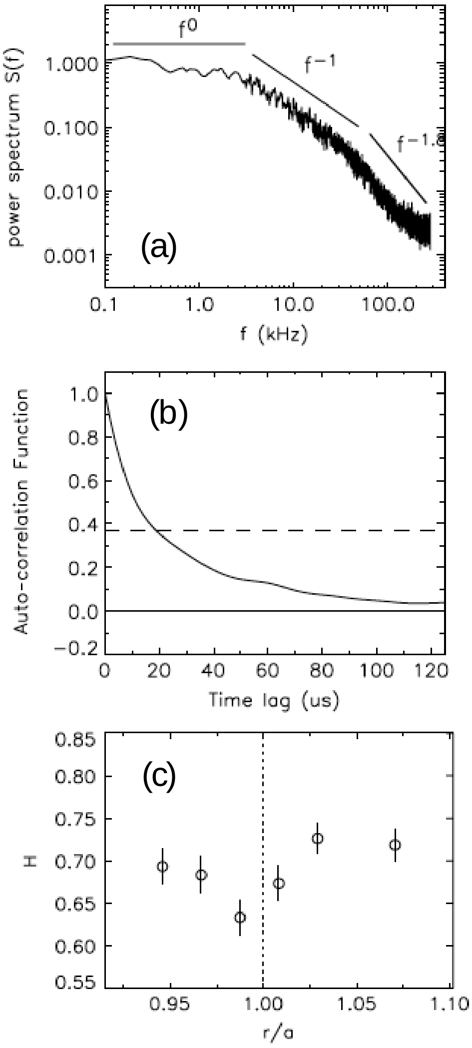

Figure 1.4: (a) The f^{-1}-scale power spectrum, (b) long-tail-like auto-correlation function and (c) large Hurst profile of the intermittent perturbation in TEXTOR [10].

In TEXTOR, the intermittency is observed having the properties similar with avalanche-like transport. Avalanche-like transport has the characteristics of intermittent bursts, radial propagation, f^{-1}-scale spectrum and long-range time correlation [44], and SOC dynamics is suggested to explained avalanche phenomenon [45–50]. Figure 1.4 displays the characteristics of intermittency obtained in TEXTOR [10]. Fig. 1.4(a) shows the existence of f^{-1}-scale at intermediate range in the power spectrum. Figs. 1.4(b) and 1.4(c) give the auto-correlation function (ACF) and Hurst profile (see section 3.3). The long-tail in ACF and the Hurst exponents greater than 0.5 indicate the self-similarity and long-range correlation of the intermittency. These evidences suggest the intermittent bursts are avalanche-like, and SOC dynamics may contribute to the generation of intermittency.

In TORPEX, an interchange wave driven production is found to be the dominant factor during the generation process of intermittency [32]. As shown in Figs. 1.7(a) and 1.7(b), the interchange mode, identified by solving a linearized Hasegawa-Wakatani model [51], is localized in the main plasma region ($r \leq 5$ cm). For the intermittent events detected by $4.5 \times \mathrm{RMS} \leq \tilde{I}_{ref} \leq 4.7 \times \mathrm{RMS}$, the results of 2D profile with conditional averaging technique (see subsection 3.4.1) at different times during the intermittency generation process are shown in Figs. 1.7(c) – 1.7(f). At first, a coherent structure is formed as shown in Fig. 1.7(c). Then, Figure 1.7(d) shows the amplitude increase and radial elongation of the mode structure, which is caused by the increase of the local pressure gradient. After that, the structure is cut into two parts by the $\vec{E} \times \vec{B}$ shear flow, and the part on the low field side thus propagates outward as an intermittent event, as shown in Figs. 1.7(c) and 1.7(d).

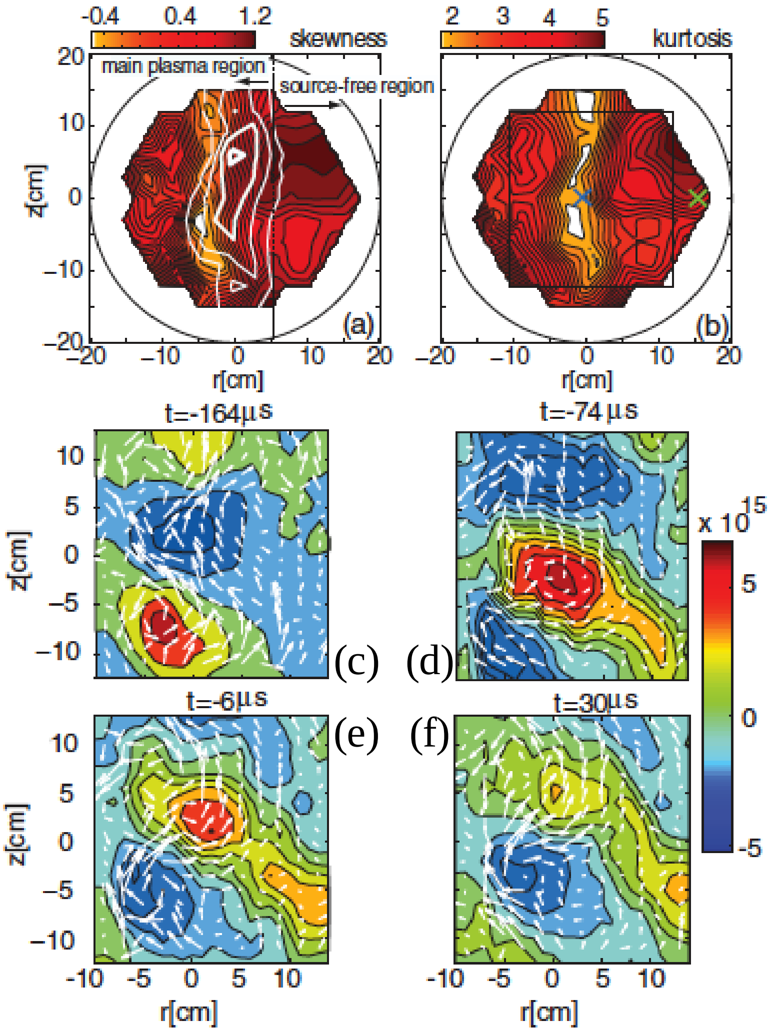

Figure 1.7: 2D profiles of (a) skewness and (b) kurtosis of ion-saturation signals in TORPEX. The contours corresponding to 90%, 60%, 30% and 10% of the maximum of the interchange wave spectral power in the frequency range 3.9 ± 1 kHz are shown in (a). The 2D profiles of density fluctuation calculated with conditional averaging technique at different times during intermittency burst are shown in (c) – (f). The arrows are the instantaneous $\vec{E} \times \vec{B}$ velocity [32].

While the experiments in TORPEX reveal that the intermittency is driven by interchange mode, experiments in Blaamann torus gives another explanation [33]. A coherent structure for both floating potential and electron saturation current is found to be associated with the intermittency.

The temporal evolution of the coherent structure for floating potential repeats a cycle of dipole-like and monopole-like vortex. The time scale of a cycle is around 112 μs, during which the dipole appears for about 68 μs. Meanwhile, the density fluctuation is correlated with the potential fluctuation. Figure 1.8 shows the conditional averaging results of floating potential and electron saturation current at a time delay of -16 μs from intermittency burst in Blaamann. The dipole structure for both floating potential and electron saturation current (which indicates the electron density perturbation) is clearly displayed with a phase-shift of about $\pi/2$. An electric filed $\vec{E}$ is generated because of the separate of the dipole potential vortex, and the $\vec{E} \times \vec{B}$ force drives the positive part of the dipole density vortex move outward. The intermittent outward particle flux is thus generated as shown in Fig. 1.8(c). Such coherent-structure-driven mechanism is also observed in other devices [43].

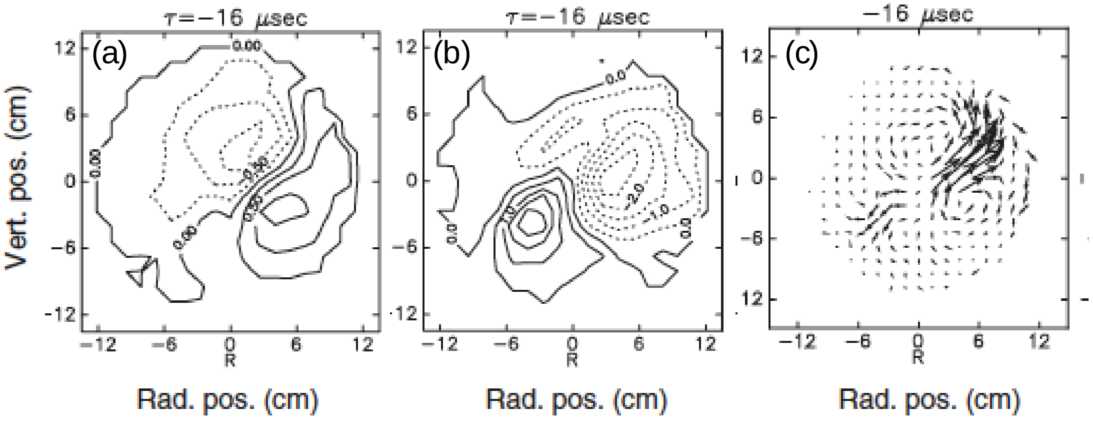

Figure 1.8: The 2D profiles of (a) floating potential, (b) electron saturation current and (c) particle flux in Blaamann at a time delay of -16 μs with conditional averaging technique [33].

Experiments in JET offers another mechanism for intermittency generation, which is zonal flow [19]. Positive and negative intermittent density bursts are generated in the edge shear layer, where zonal flow shear off the meso-scale coherent structures, as shown in Fig. 1.9. In Figure 1.9, the shear layer is located between $\Delta r = -15$ and $\Delta r = -3$ mm where $\Delta r = r - r_{LCFS}$ is the radial distance to LCFS. The conditional averaging results of ion saturation I_s, radial $\vec{E} \times \vec{B}$ fluctuating velocity $v_r = E_\theta / B$ and poloidal $\vec{E} \times \vec{B}$ fluctuating velocity $v_\theta = E_r / B$ for positive bursts are shown in Figs. 1.9(a), 1.9(c) and 1.9(e), respectively, and Figs. 1.9(b), 1.9(d) and 1.9(f) show the corresponding results for negative bursts. Figs. 1.9(a) and 1.9(b) give the initial meso-scale coherent structures with positive and negative perturbations in the edge shear layer. The positive and negative perturbations have similar amplitudes. However, because of the E_θ caused by interchange drive, their radial movement directions are opposite as shown in Figs. 1.9(c) and 1.9(d). Moreover, as the meso-scale structures are strongly titled in the shear layer, the internal polarization direction is thus modified and a spontaneous E_r is generated, which also drives positive and negative perturbations move in different poloidal directions, as shown in Figs. 1.9(e) and 1.9(f). As a result, the structures are sheared off, and the positive and negative intermittent bursts are thus generated.

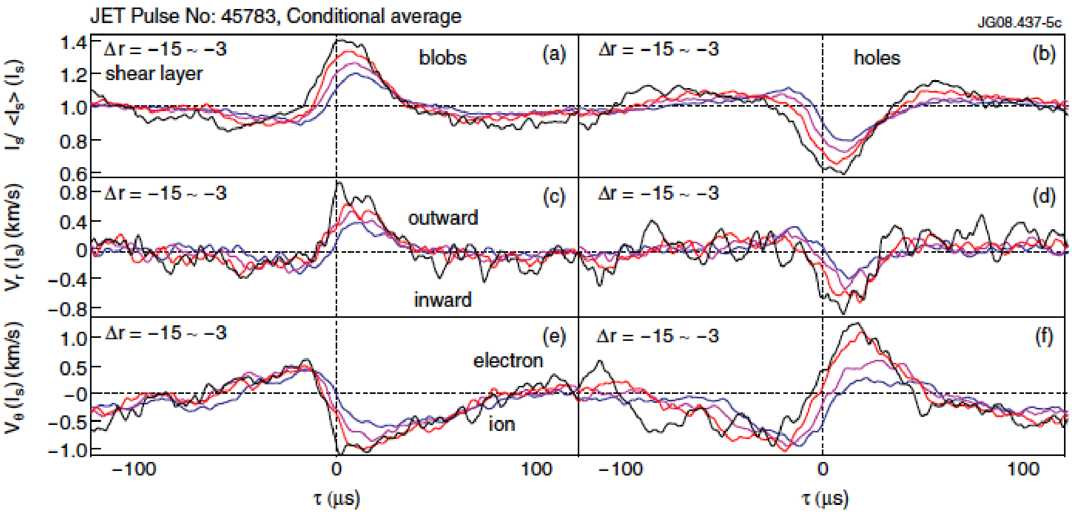

Figure 1.9: The conditional averaging results of (a) I_s, (c) v_r and (e) v_θ for positive intermittent bursts in shear layer in JET. (b), (d) and (f) are corresponding results for negative bursts [19].

Except for the examples introduced above, there are some other mechanisms for intermittency generation, such as gradient-driven mechanism [24]. However, none of the mechanism is widely accepted for plasma in other devices.

1.3 Purpose of this thesis

Since the intermittent density bursts have a significant influence on particle transport, plasma confinement and material interaction, and there is still no widely accepted and applicable mechanism to explain its generation, it is necessary to have a further investigation on it.

Laboratory plasma is very useful to study the turbulent intermittency, because it has excellent reproducibility and controllability and allows multi-point simultaneous measurement. This study was made to reveal the generation mechanism of the turbulence intermittency through the laboratory plasma experiment. Recently, a quasi-coherent fluctuation has been excited in the central region of linear magnetized laboratory plasma in the PANTA through large density gradient. The fluctuation is nonstationary and its amplitude varies in time intermittently. Impact of the intermittent event is observed in the whole plasma region including peripheral region where density gradient is weak. There is, however, still little understanding on it. Thus, the purpose of this thesis is to study the intermittent phenomenon in PANTA. The important studies of the intermittency are remained that i) how does the quasi-coherent mode behave, ii) what are the characteristics of the intermittency and iii) how is the quasi-coherent mode correlated to the intermittency.

To achieve the purpose, the advanced microwave reflectometers are developed, which can simultaneously measure the density perturbations at radial multi-point. The turbulence intermittency experiment is thus performed with the reflectometers.

This thesis is organized as follows: The development of microwave reflectometers in PANTA are presented in Chapter 2. The development of data analysis methods for intermittency study are described in Chapter 3. In Chapter 4, the experiment results and corresponding discussion on intermittency are shown. The summary of the thesis is in Chapter 5.

Chapter 2

Development of microwave reflectometer diagnostics in PANTA

Diagnostic techniques are essential for experimental plasma study. In PANTA, many different types of diagnostic systems have been developed, and the most commonly used diagnostics are probes. However, the use of probe will disturb the plasma as it is inserted into plasma. Recently, microwave diagnostic has become an important and widely used tool in the field of plasma research. The advantage of microwave diagnostic is that it does not disturb the plasma and has high spatial-temporal resolution. Thus, microwave diagnostics is also developed in PANTA. In my study, a frequency comb reflectometer and a frequency comb sweep reflectometer are used as the main diagnostic tools. These two systems along with device PANTA will be described in this chapter.

2.1 Introduction of PANTA

PANTA (Plasma Assembly for Nonlinear Turbulence Analysis) is a cylindrical device which focuses on plasma turbulence study. In PANTA, lots of works on basic turbulence have been carried out, such as the basic processes of turbulence [52, 53], turbulence transport [54, 55], nonlinear turbulence interaction [56, 57], etc. Figure 2.1 illustrates the schematic view of PANTA. The cylindrical vacuum vessel has a diameter of 450 mm and a length of 4050 mm. The axial magnetic field produced by 17 magnetic coils ranges up to 1500 Gauss, which is almost constant along the axis. Argon gas which is used as the main fueling gas is injected into the vacuum vessel from the source region at the top. The pressure of neutral gas is 0 − 3 mTorr. Helicon wave (7 MHz) produced by a double-loop antenna is used to excite the neutral gas and produce the plasma, and its power varies from 2 kW to 6 kW. The cylindrical is thus produced with a diameter of around 10 cm, and its central electron density and temperature are approximately 1.0×10^{19} m^{-3} and 3 eV, respectively. The typical experimental conditions and parameters are listed in Table 2.1 [58].

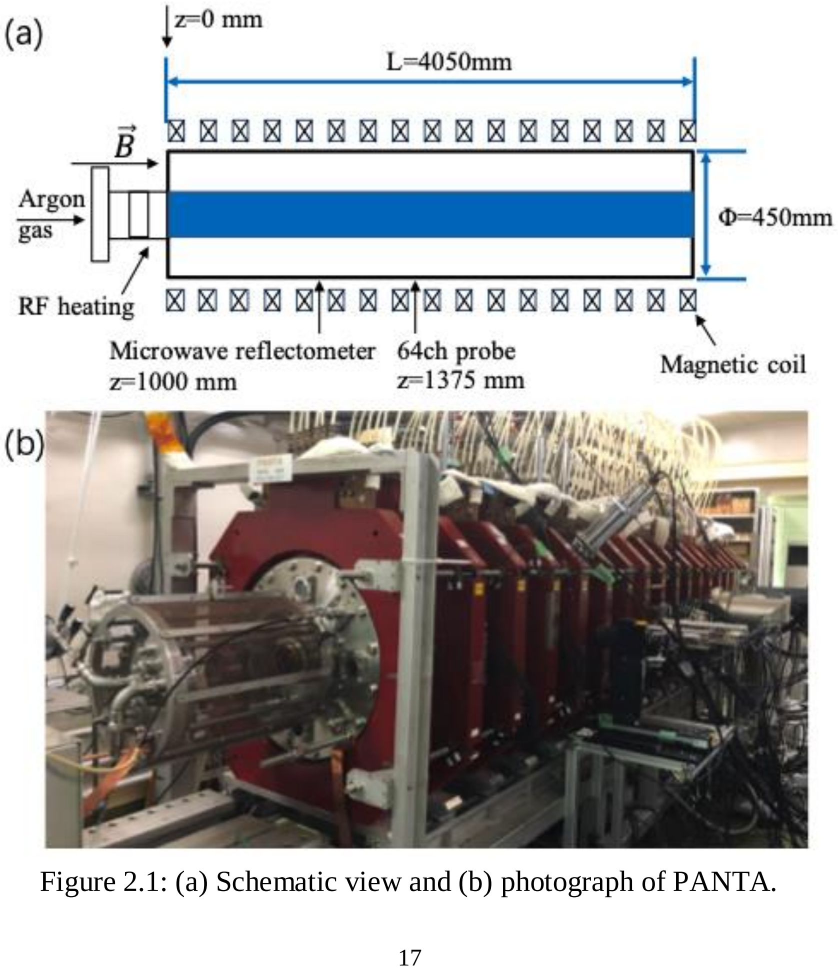

Figure 2.1: (a) Schematic view and (b) photograph of PANTA.

Parameters	Typical Value	Range
Background Pressure	9.0×10^{-5} Pa	$8.0\times10^{-5} - 1.0\times10^{-4}$ Pa
Filling Gas Pressure	1.5 mTorr	1.0 − 3.0 mTorr
Magnetic Field	0.09 T	0.04 − 0.15 T
RF Power	3 kW	2 − 6 kW
Peak Electron Density	1.0×10^{19} m^{-3}	$1.0\times10^{18} - 1.0\times10^{19}$ m^{-3}
Electron Temperature	3 eV	1.5 − 3 eV
Ion Temperature	0.3 eV	0.2 − 0.4 eV

Table 2.1: Typical plasma parameters in PANTA and available ranges.

The main adjustable control plasma parameters in PANTA are helicon wave heating power (2–6 kW), magnetic field strength (400–1500 Gauss) and neutral gas pressure (1.0–3.0 mTorr).

In my experiment, the microwave reflectometer is installed at 1 meter in the axial direction of PANTA as shown in Fig. 2.1(a). The cross section of the vacuum chamber and reflectometer antennas is shown in Fig. 2.2. The distance from the antennas to the center axis of plasma column is 225 mm, as shown in Fig. 2.2.

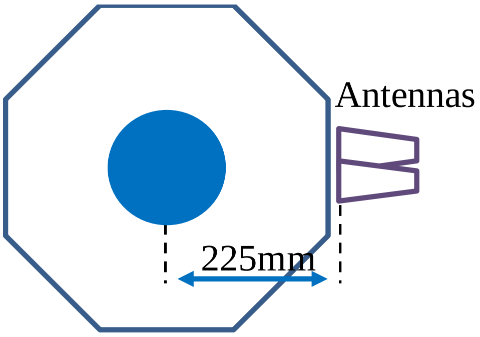

Figure 2.2: Arrangement of the comb reflectometer in PANTA.

2.2 Microwave in plasma

2.2.1 Dispersion equations

In a uniform magnetized cold plasma, the electric displacement $\vec{D}$ is expressed as [59],

$$\vec{D} = \varepsilon_0 \vec{E} + \frac{i}{\omega} \vec{j} \equiv \varepsilon_0 \overleftrightarrow{K} \cdot \vec{E} \tag{2.1}$$

where ε_0 is dielectric constant of the vacuum, $\vec{E}$ is the electric intensity, $\vec{j}$ is the current and $\overleftrightarrow{K}$ is called the dielectric tensor. In cold plasma, the current is mainly due to the electron motion,

$$\vec{j} = e n_e \vec{v}_e \tag{2.2}$$

where e is the elementary charge and n_e is electron density. Here, the motion velocity $\vec{v}_e$ can be represented by electric intensity $\vec{E}$, magnetic field $\vec{B}$ (the z axis is taken along the direction of $\vec{B}_0$) and a plane-wave $\exp\left(i\vec{k} \cdot \vec{r} - i\omega t\right)$ [59]. By replacing the $\vec{j}$ in Eq. (2.1) with Eq. (2.2), the dielectric tensor $\overleftrightarrow{K}$ is solved as,

$$\overleftrightarrow{K} \cdot \vec{E} = \begin{pmatrix} K_\perp & -iK_\times & 0 \\ iK_\times & K_\perp & 0 \\ 0 & 0 & K_\parallel \end{pmatrix} \begin{pmatrix} E_x \\ E_y \\ E_z \end{pmatrix} \tag{2.3}$$

where

$$\begin{cases} K_{\perp} \equiv 1 - \sum_{k} \dfrac{{\omega_{pe}}^2}{\omega^2 - {\omega_{ce}}^2} \\ K_{\times} \equiv - \sum_{k} \dfrac{{\omega_{pe}}^2}{\omega^2 - {\omega_{ce}}^2} \dfrac{\omega_{ce}}{\omega} \\ K_{\parallel} \equiv 1 - \sum_{k} \dfrac{{\omega_{pe}}^2}{\omega^2} \end{cases} \tag{2.4}$$

where ${\omega_{pe}}^2 = n_e e^2 / \varepsilon_0 m_e$ is the electron plasma frequency and $\omega_{ce} = eB/m_e$ is electron cyclotron frequency. From the Maxwell's equation,

$$\begin{cases} \nabla \times \vec{E} = -\dfrac{\partial \vec{B}}{\partial t} \\ \nabla \times \vec{H} = \vec{j} + \varepsilon_0 \dfrac{\partial \vec{E}}{\partial t} = \dfrac{\partial \vec{D}}{\partial t} \end{cases} \tag{2.5}$$

the following equation is obtained,

$$\vec{k} \times \left(\vec{k} \times \vec{E}\right) + \frac{\omega^2}{c^2} \vec{K} \cdot \vec{E} = 0 \tag{2.6}$$

Here, we define a dimensionless vector,

$$\vec{N} \equiv \frac{c\vec{k}}{\omega} \tag{2.7}$$

where c is light velocity in vacuum, and the absolute value $N = \left|\vec{N}\right|$ is the wave index of refraction. Thus, Eq. (2.6) is rewritten as,

$$\vec{N} \times \left(\vec{N} \times \vec{E}\right) + \overleftrightarrow{K} \cdot \vec{E} = 0 \tag{2.8}$$

In the case that wave propagates in the direction perpendicular to the magnetic field, the solution of the equation above is

$$N^2 = K_{\parallel} \tag{2.9}$$

or

$$N^2 = \frac{{K_{\perp}}^2 - {K_{\times}}^2}{K_{\perp}} \tag{2.10}$$

Eq. (2.9) and Eq. (2.10) are called the dispersion equations. For the wave that satisfies Eq. (2.9), the electric field is $E_x = E_y = 0,\ E_Z \neq 0$ and the wave is called ordinary wave (O-mode wave). The electric field of the wave satisfying Eq. (2.10) is $iE_x/E_y = -K_\times/K_\perp,\ E_x = 0$ and the wave is called extraordinary wave (X-mode wave).

When the refractive index becomes zero $N^2 = 0$, the wave is said to be cut-off, i.e., the wave is reflected at the cut-off layer. The cut-off frequency of O-mode wave is as follows,

$$\omega_{O,cut} = \omega_{pe} \tag{2.11}$$

while the cut-off frequency of X-mode wave is

$$\omega_{X,cut} = \left({\omega_{ce}}^2/4 + {\omega_{pe}}^2\right)^{1/2} \pm \omega_{ce}/2 \tag{2.12}$$

The idea of microwave reflectometer is thus to launch microwave into plasma, which is reflected at the cut-off layer. The time delay of the reflected wave and the frequency of incident wave contains the location and density information of the cut-off layer, respectively. Thus, the density profile and density fluctuation can be obtained.

2.2.2 Wave scattering and Doppler shift

The phase difference (i.e., time delay) between reflected and incident waves is expected to fluctuate around a mean value, which is due to the fluctuation of the cut-off layer. However, since the early 1990s, it was found that the phase difference monotonically increased or decreased [60].

Such phenomenon was called phase runaway (PRA). After the heterodyne reflectometer was developed for plasma diagnosis, the asymmetric spectra were found to be the cause for PRA [61], and the idea to evaluate the plasma rotation and density fluctuation with PRA and the asymmetries of spectra was then proposed [62]. The first measurement of Doppler shift and the perpendicular wavenumber spectrum were presented by Hirsch and Zou in 1999 [63, 64]. Since then, Doppler reflectometer have been widely designed and developed for different devices [65–73].

Different from normal reflectometer, the incident wave of Doppler reflectometer is obliquely launched into plasma, as shown in Figure 2.3 [74]. In Figure 2.3, the plasma density gradient is along z-direction, and there is no plasma for the region of $z < 0$. The microwave is launched at an angle of θ_0 to the normal of cut-off layer. Figure 2.3(a) shows the case of flat cut-off layer without turbulence. In this case, the microwave is reflected without scattering.

Figure 2.3(b) shows the situation that the turbulence exists and the cut-off layer is corrugated where scattering take place. According to Bragg's rule [64], the turbulence wavenumber $\vec{k}_{\perp}$, incident wavenumber $\vec{k}_i$ and scattering wavenumber $\vec{k}_s$ satisfies,

$$\vec{k}_{\perp} = \vec{k}_s - \vec{k}_i \tag{2.13}$$

If the turbulence wavenumber at the cut-off layer matches the condition,

$$k_\perp = 2k_i \sin\theta_0 \tag{2.14}$$

the -1st order scattering returns to the antenna (Bragg backscattering), which is shown as the pink line in Fig. 2.3(b).

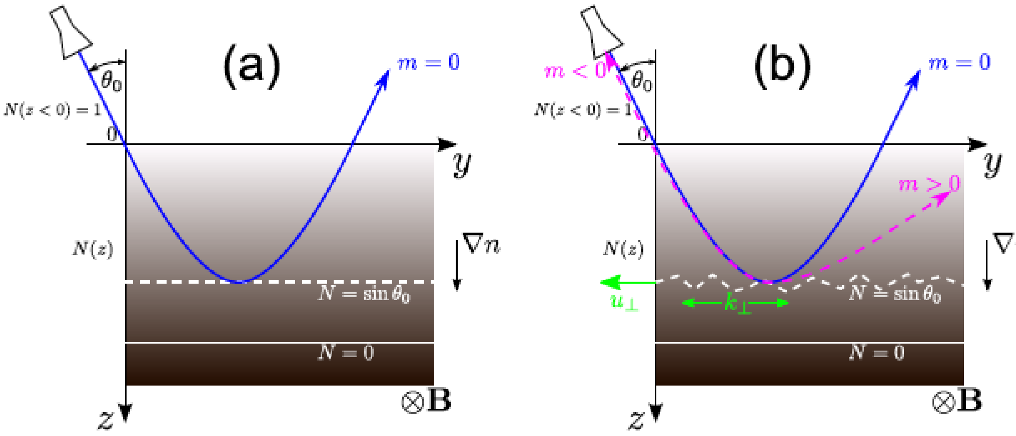

Figure 2.3: Oblique incident wave in a slab plasma (a) without and (b) with the existence of turbulence [74].

The backscattering wave contains the Doppler shift information due to the rotation of plasma turbulence. The Doppler shift frequency ω_D is written as,

$$\omega_D = \vec{u}\cdot\vec{k} = u_\perp k_\perp + u_\parallel k_\parallel + u_r k_r \tag{2.15}$$

where $\vec{u}$ is the velocity of the turbulence at the cut-off layer. In magnetically confined plasma, it is normal that $k_\perp \gg k_\parallel$, and Doppler reflectometers are only sensitive to $k_\perp$ as they are aligned perpendicular to the magnetic field. Thus, the second term on the right side of Eq. (2.15) is neglected [74]. In addition, as the radial spectrum is normally centered around 0, the radial term is neglected as well [70]. Eq. (2.15) is thus rewritten as,

$$\omega_D = 2u_\perp k_i \sin\theta_0 \tag{2.16}$$

The azimuthal rotation velocity of plasma thus can be obtained by from the Doppler shift of the scattering wave in oblique incidence case.

2.3 Development of frequency comb microwave reflectometer in PANTA

2.3.1 Introduction of frequency comb microwave reflectometer

Microwave reflectometer diagnostic for plasma electron density profile and density fluctuation measurement, which is realized by measuring the time of flight of microwave reflected by the plasma cut-off layer, is proved to be feasible [75, 76]. The simplest design is to launch a single fixed frequency signal into plasma, which will be reflected at cut-off layer as described in subsection 2.2.1. By receiving the reflected signal and calculate the time of flight in plasma, the location of the cut-off layer is determined. The fluctuation of flight time also gives information of density fluctuation.

To raise efficiency and improve spatial resolution, it is necessary to simultaneously output an array of fixed-frequency signals and such system is called multi-channel microwave reflectometer. If the array of frequencies are equally spaced, such multi-channel reflectometer is called as frequency comb microwave reflectometer. The waves with different frequencies are reflected by cut-off layers at different radial points, the profile of density and fluctuation is thus obtained.

The difficulty of multi-channel reflectometer is the generation of multi-frequency signals, and there are several different methods to solve the problem.

i) The easiest way is to combine the signals of several independent microwave sources, such as Gunn oscillators [76–79]. However, this method is usually costly.

ii) A novel filter-based feedback loop microwave source (FFLMS) method is recently developed to generator multi-frequency [67–69]. As shown in Fig. 2.4(a), the broadband electronic noise is amplified by the amplifier. Because of the response functions of bandpass filter and amplifier, the signal with chosen frequency is self-reinforced in the loop and a pure sinusoid waveform is obtained. Moreover, this method can be optimized by multiplexer-based frequency array source (MFAS) as shown in Fig. 2.4(b). The array of bandpass filters is replaced by two multiplexers with bandpass response, and comb frequency signal can also be obtained by arranging the bandpass frequencies of filters equally spaced. The multi-frequency signal obtained in this way has not only good phase noise performance but also larger and uniform output power for each channel.

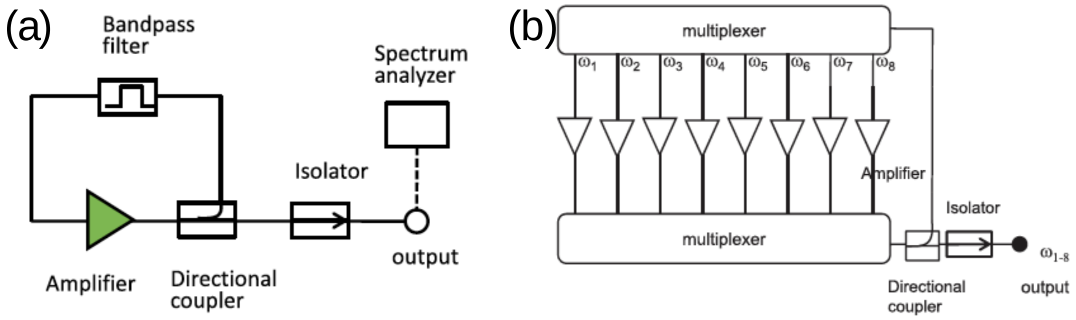

Figure 2.4: The schematic of (a) FFLMS and (b) MFAS [67, 69].

iii) Another widely used method is the nonlinear transmission line (NLTL) [65, 66]. As shown in Fig. 2.5, a stable internally phase-locked 2.5 GHz source is passed into a NLTA after amplified. Due to the nonlinear effect of the NLTL, an array of frequencies are generated. It is noted that the frequencies generated in this way are equally spaced ($\Delta f = 2.5$ GHz here), which means this method can only generate the comb-frequency signal. With this method, the output signal has an excellent phase noise performance and a very wide band up to ~ 100 GHz. Compared with the two methods before, the advantage of NLTL is that it can generator more frequency channels at lower cost. However, the power is usually decayed at high frequency, which needs to be optimized by E-H tuner.

As mentioned in subsection 2.2.2, the comb reflectometer can also be used as Doppler reflectometer [65–73], which aims to measure the poloidal rotation velocity and wavenumber spectrum of plasma turbulence. The Doppler reflectometer inject the microwave oblique to the plasma and is sensitively to the fluctuation with certain wavenumber associated with incident angle. The turbulence spectrum with different wavenumber can be measured by scanning the incident angle. With frequency comb Doppler reflectometer, the radial profile of turbulence poloidal velocity and spectrum can be obtained.

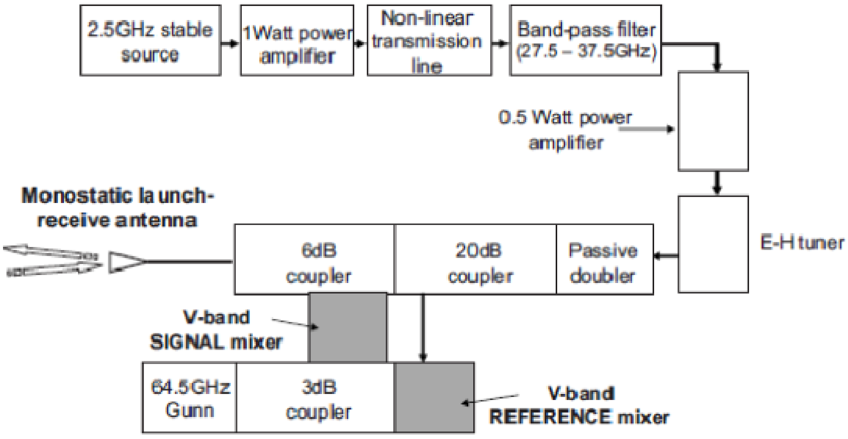

Figure 2.5: The schematic of frequency comb reflectometer [65].

2.3.2 System design and signal processing

In PANTA, a frequency comb microwave reflectometer, which has up to 29 frequency channels, has been developed [80]. This system uses NLTL as the comb frequency signal generator. Figure 2.6 illustrates the circuit of the comb microwave reflectometer. The incident wave is generated by the NLTL frequency comb generator. After filtered and amplified, one channel is directly transferred to the digital storage oscilloscope (DSO) as reference signal, and another channel is launched into plasma by a dual-band rectangular horn antenna as O-mode wave. The reflected wave is received by another antenna and transferred to the DSO as well.

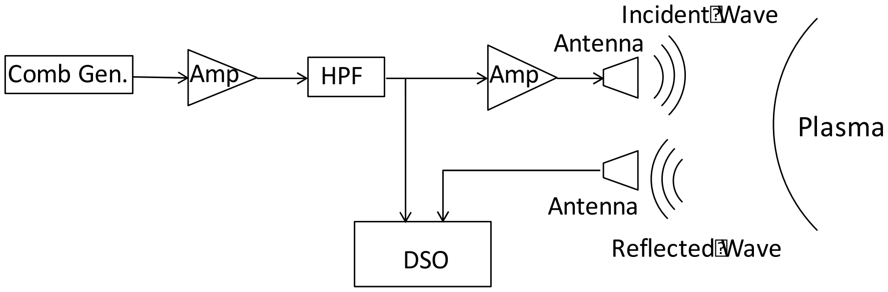

Figure 2.6: Block diagram of the frequency comb microwave reflectometer system.

The typical incident wave signals and its power spectrum density (PSD, see section 3.1) spectrum are shown in Figs. 2.7(a) and 2.7(b), respectively. It is clear that the repetition period of the incident wave envelope is 2 ns, which is corresponding to a repetition frequency of 0.5 GHz, as shown in Fig. 2.7(b). The frequency of large power components range from 12 GHz to 26 GHz, with an interval of 0.5 GHz. Thus, totally 29 channels are used for experiments.

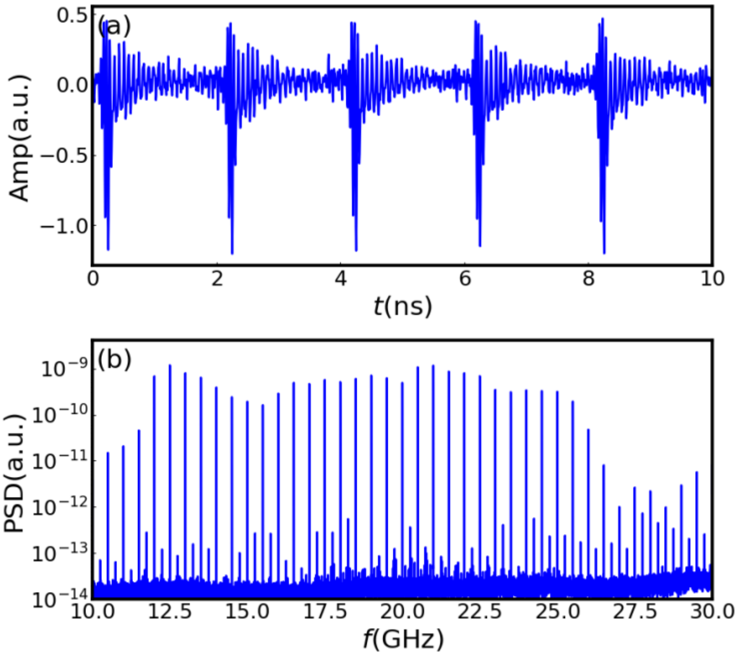

Figure 2.7: (a) Typical incident wave signal. (b) PSD of incident wave.

The reflected and incident wave signals are shown in Figure 2.8. It is clear that a time delay τ exists between incident and reflected waves. The phase difference ϕ can be extracted by cross-spectrum analysis, and the time delay is thus calculated from the phase difference.

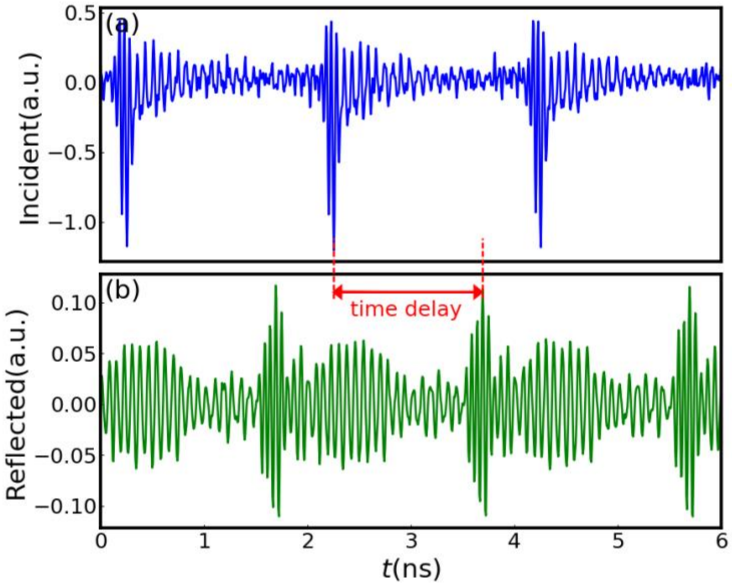

Figure 2.8: Typical (a) incident wave signal and (b) reflected wave signal.

To increase the precision and reduce the error, the template method of conditional averaging technology (see subsection 3.4.2) is applied to the signal. The initial template is obtained by assemble averaging the original signal according to the window length (2 ns). The initial template (averaged with 500 ensembles [81]) and the cross-correlation function between the template and original signal are shown in Figs. 2.9(a) and 2.9(b), respectively. Due to the stable frequency component, the peaks of cross correlation function are more than 0.9. Thus, the new template is obtained according to the peaks. By iteration, the final averaged signals of incident and reflected waves are shown in Figure 2.10.

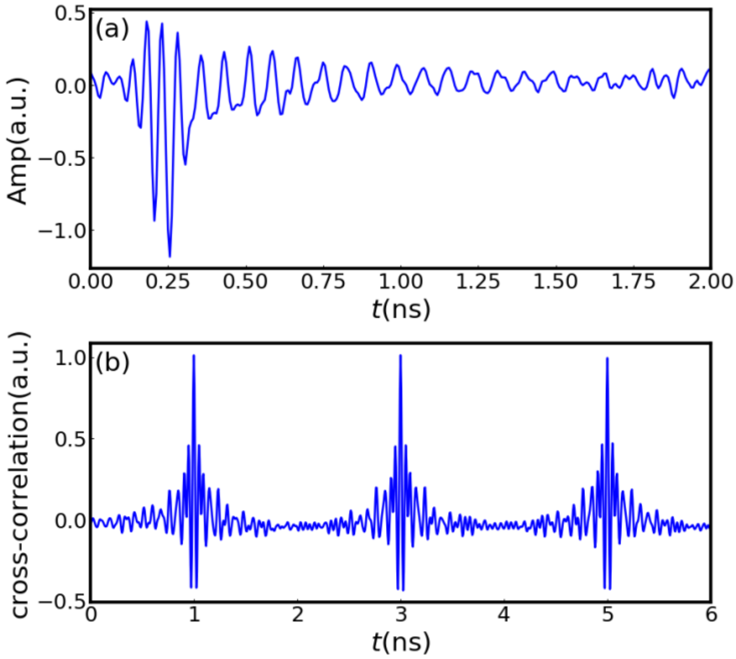

Figure 2.9: (a) Initial template of incident wave. (b) Cross-correlation between template and original signal.

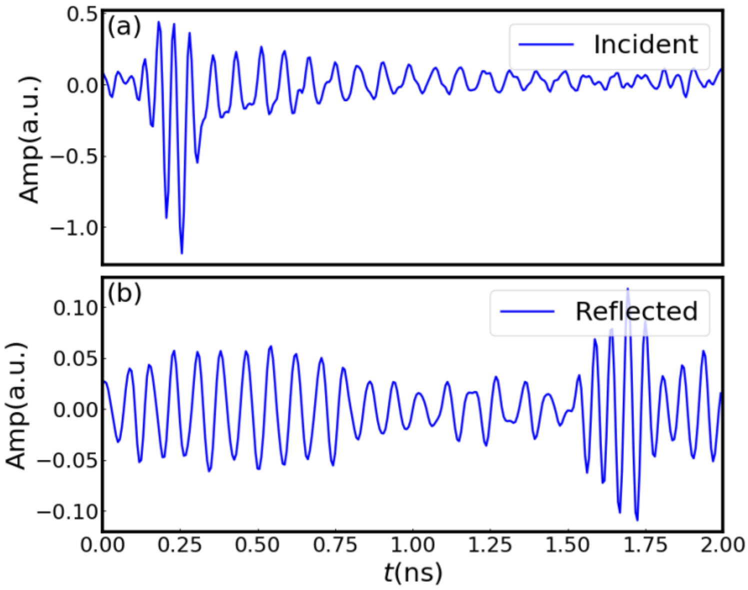

Figure 2.10: Conditional averaging results of (a) incident wave and (b) reflected wave.

The comparison of the PSD of the signal with and without conditional averaging is shown in Figure 2.11. It is clear that the level of noise with the frequency lower than 12 GHz or higher than 26 GHz is effectively decreased by conditional averaging.

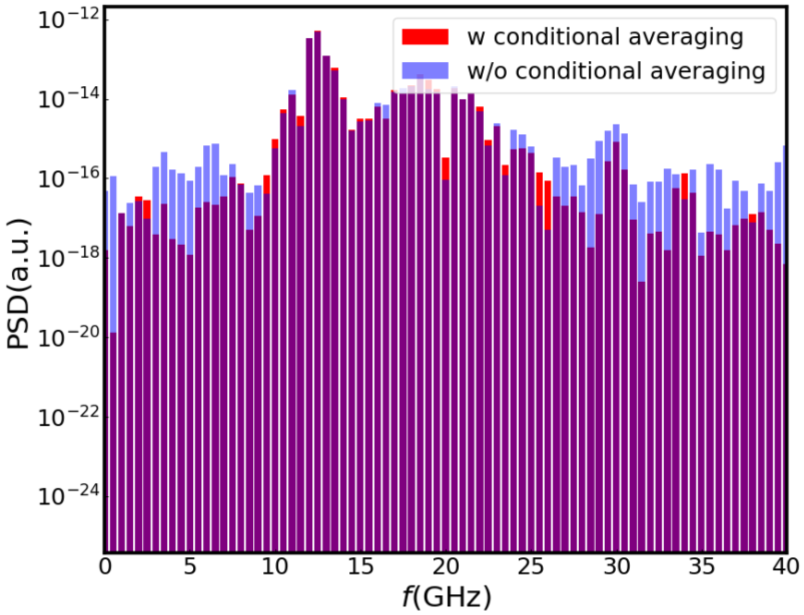

Figure 2.11: Comparison of the PSD of the signal with and without conditional averaging.

2.3.3 Benchmark test

The benchmark test of the system is performed with a metal reflector which is vertical to the antenna. Move the reflector to change the distance L between reflector and antenna, and the relationship of phase difference ϕ versus L is obtained as shown in Fig. 2.12(a). Here, three typical frequency (12 GHz, 18 GHz and 25 GHz) components are selected, and the solid lines are linear fitting of them. It can be seen that all ϕ have a good linear relation with L for all frequency components as expected. It is also noted that the slope of the linear fitting equals to the injection frequency. Besides, the relationship between ϕ and incident frequency

f_{in} while the reflector is fixed ($L = 10$ cm) is shown in Fig. 2.12(b), which also reveals a good linear relation. Both of the results indicates the reliability of the system.

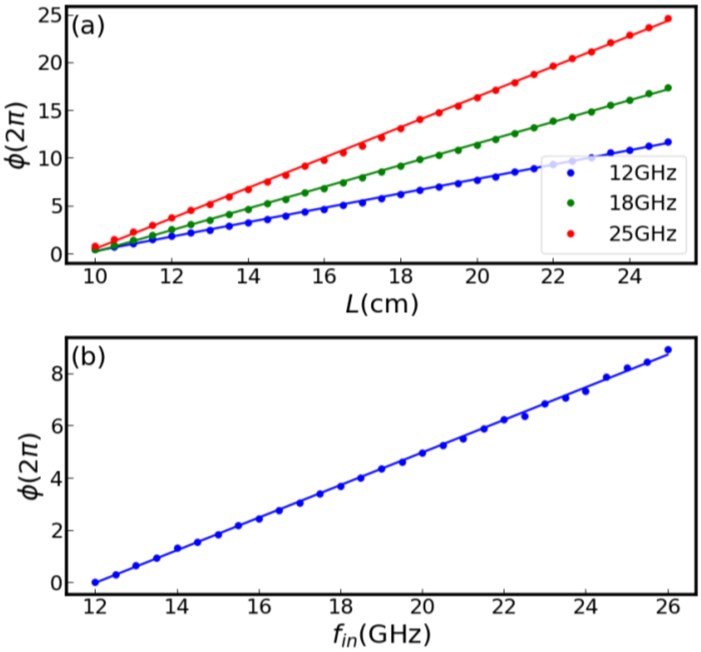

Figure 2.12: Relationship between (a) ϕ and L and (b) ϕ and f_{in}.

2.3.4 Density profile reconstruction

Since the phase difference ϕ is obtained, the time delay τ is thus obtained by $\phi = 2\pi f_{in}\tau$. If the time delay of frequency lower than incident frequency are known, the radial location of cut-off layer is calculated with Abel inversion,

$$r_{cut}(f) = \frac{c}{\pi}\int_0^{f_{in}} \frac{\tau(f)df}{\sqrt{{f_{in}}^2 - f^2}} \tag{2.17}$$

However, while the frequency of incident wave starts from 12 GHz, there is no data of time delay for low frequency. In this case, the change of the wave length inside dense plasma is neglected, and the phase difference is rewritten as,

$$2L_i = \lambda_i(N_i + \phi_i) \tag{2.18}$$

where i denotes the i-th frequency component ($f_i = 11.5 + 0.5$ GHz, $i = 1, 2, \ldots, 29$), L_i and λ_i are the path length and wavelength respectively, ϕ_i is the phase difference normalized by 2π and N_i is integer. The path length difference for two adjacent frequency components is thus written as,

$$2\left(\frac{L_{i+1} - L_i}{\lambda_{i+1}} + \frac{L_i}{\lambda_{eff}}\right) = \phi_{i+1} - \phi_i + m \tag{2.19}$$

where $\lambda_{eff} = 1/(1/\lambda_{i+1} - 1/\lambda_i) = c/(f_{i+1} - f_i)$ and m is integer. In the experiments, L_i is usually much smaller than λ_{eff}. Because the adjacent cut-off layer is close, we assume $0 < L_{i+1} - L_i < \lambda_{i+1}$. Thus, $\phi_{i+1} - \phi_i + m$ is usually smaller than 2, which means m is 1 or 2. Therefore, L_{i+1} is obtained from

$$\frac{L_{i+1}}{\lambda_{i+1}} = \frac{L_i}{\lambda_i} + \frac{\phi_{i+1} - \phi_i + m}{2} \tag{2.20}$$

This means that the location of $i + 1$-th cut-off layer can be calculated from the i-th cut-off layer positon. The initial cut-off layer is determined from assumption or the maximum cut-off frequency. While the incident frequency is higher than the cut-off frequency for the maximum density, the incident microwave transmits the plasma and the received microwave power decreases. In this case, the maximum density and its location is determined.

The electron density profile in PANTA is reconstructed at the following discharge parameters: a heating power of 6 kW, a magnetic field of 0.09 T and a natural argon pressure of 1 mTorr. m is determined with the smooth density profile condition. The density profile is shown in Fig. 2.13.

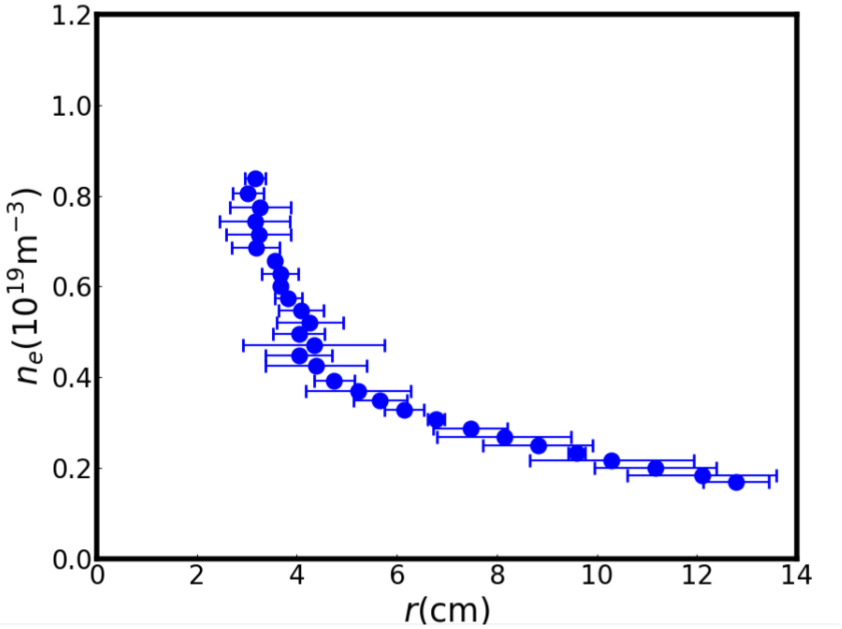

Figure 2.13: Electron density profile reconstructed with comb reflectometer.

2.3.5 Density perturbation measurement

The fluctuation of electron density, or in other words the fluctuation of cut-off layer, causes perturbation of phase difference $\tilde{\phi}$. Since no radial-coherent fluctuation is excited in the low density gradient region, the radial wavenumber (k_r) is considered to be close to zero, which satisfies the small radial wavenumber condition ($k_r < k_{in}^{2/3} L_N^{-1/3}$ where k_{in} is the wavenumber of incident wave and L_N is the density gradient length) [82, 83]. In this case, the back-scattering from such low-k_r structures in this region is weak and has little effect on the reflected wave from the cut-off layer. In the large-gradient region where coherent fluctuation is easily excited, the back-scattering occurs and leads to an increase in the error of radial location. However, as such structure is localized inside the narrow large-gradient region (discussed later), the error-bars of the locations are almost the same as those of the density profile which are shown in Fig. 2.13. Therefore, the effect of back-scattering can be neglected. In the case of low-k_r condition, the equation between the fluctuation of electron density and phase difference is as follows [83],

$$\tilde{n}_e = \frac{\lambda \nabla n_e \tilde{\phi}}{n_e} \tag{2.21}$$

where λ is a constant for a certain fluctuation. This means that the density fluctuation strength at the cut-off layer is proportional to the phase difference strength, and the phase perturbation can thus be used to study the density perturbation. A typical time series of phase difference is shown in Figure 2.14, and the perturbation is obvious, which indicates the perturbation of density.

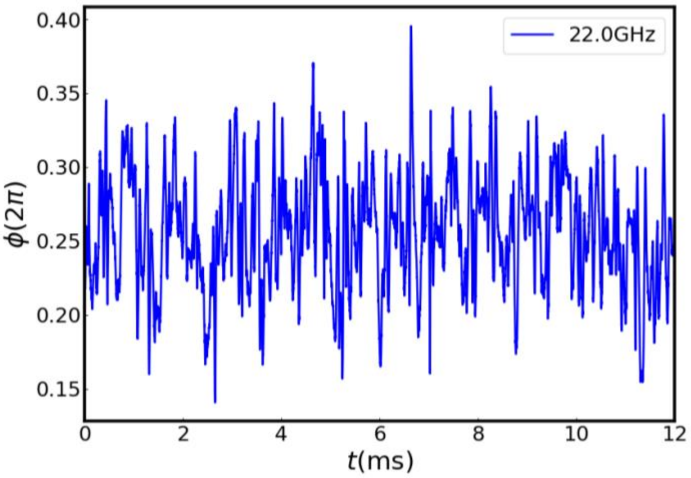

Figure 2.14: Temporal evolution of phase difference of 22 GHz component.

2.3.6 Azimuthal velocity measurement

As mentioned in subsection 2.2.2, microwave reflectometer can be used to measure the plasma azimuthal velocity while oblique incidence. In PANTA, the comb microwave reflectometer is aligned with a maximum angle of 4° to the middle plane of the plasma column. A typical Doppler shift frequency spectrum at the incident frequency $f_{in} = 21.5\ \mathrm{GHz}$ is shown in Fig. 2.15. Figure 2.15 obviously shows two components in the spectrum: the zero-frequency broad spectrum $S_1(f)$ which is directly reflected by the cut-off layer and the finite $f = f_D$ spectrum $S_2(f)$ which is due to the plasma rotation. Ideally, both of the two components are Gaussian distribution, and there are two methods to extract the Doppler shift f_D.

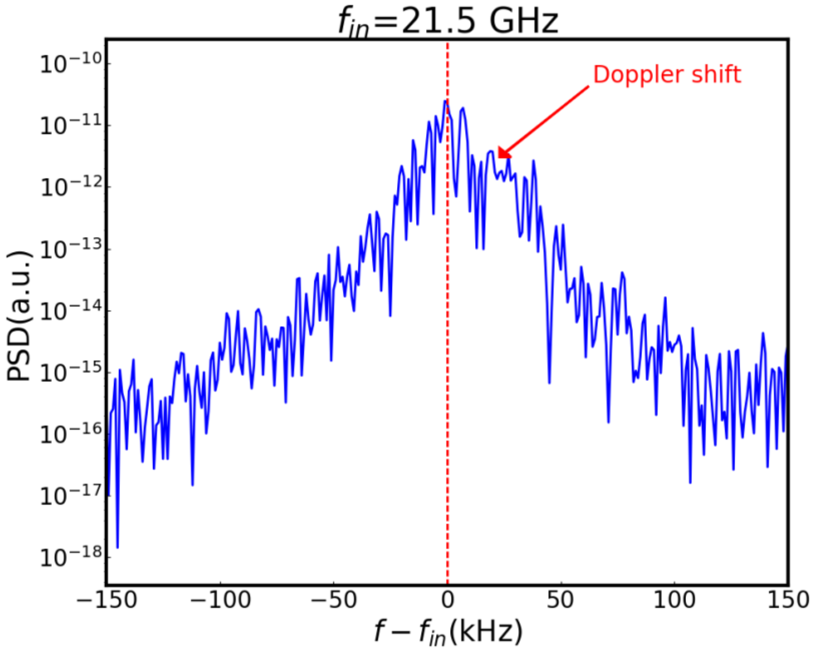

Figure 2.15: Frequency Doppler shift of 21.5 GHz component.

The first way is the weighted average algorithm. f_D is calculated as,

$$f_D = \frac{\int_{-f_1}^{f_1} f \cdot S(f - f_{in}) df}{\int_{-f_1}^{f_1} S(f - f_{in}) df} \tag{2.22}$$

where $S(f) = S_1(f) + S_2(f)$ is the total power spectrum density (noise neglected) and f_1 is the limit of integration. Due to the symmetry of $S_1(f)$ on $f = f_{in}$, $\int_{-f_1}^{f_1} f \cdot S_1(f - f_{in}) df = 0$, thus Eq. (2.22) can be used to calculate Doppler shift. However, as $\int_{-f_1}^{f_1} S(f - f_{in}) df = \int_{-f_1}^{f_1} S_1(f - f_{in}) df + \int_{-f_1}^{f_1} S_2(f - f_{in}) df > \int_{-f_1}^{f_1} S_2(f - f_{in}) df$, an error is introduced to the calculation which makes f_D smaller than true Doppler shift.

Another method is decomposition and fitting. Since $S_1(f)$ is symmetric on $f = f_{in}$, i.e., $S_1(f')$ is an even function, where $f' = f - f_{in}$. $S(f')$ can thus be rewritten as the sum of even and odd function,

$$S(f') = S_e(f') + S_o(f') \tag{2.23}$$

where

$$\begin{cases} S_e(f') = \dfrac{S(f') + S(-f')}{2} \\ S_o(f') = \dfrac{S(f') - S(-f')}{2} \end{cases} \tag{2.24}$$

Fitting $S_o(f')$ where $f' > 0$ with a Gaussian function gives f_D [84]. However, as the spectrum of Doppler shift $S_2(f')$ is not odd function, this method brings an error in estimating the Doppler shift as well. W. L. Zhong evaluated the influence of error [84]. He found that the error of f_D mainly depends on $f_D/FWHM$, where $FWHM$ is the full width half maximum of the Doppler spectrum. The error decreases as $f_D/FWHM$ increases, and it can be neglected when $f_D/FWHM > 0.75$. By improving the arrangement of reflectometer (e.g., adjust the angle of antenna), $f_D/FWHM$ can be increased and error can be decreased.

2.4 Development of frequency comb sweep microwave reflectometer in PANTA

2.4.1 Introduction of frequency modulation continuous wave reflectometer

Another widely used design of microwave reflectometer is frequency modulation continuous wave (FMCW) reflectometer, which is mainly used for density profile measurement [85–97]. FMCW reflectometer sweeps frequency rapidly which is usually achieved with a voltage control oscillator (VCO) and thus the time of flight appears as beat frequency or phase difference between incident and reflected waves, eliminating the 2π ambiguity of phase difference for comb reflectometer. Therefore, FMCW can obtain density profile with high temporal and spatial resolution and is considered to have the potential to be used in ITER and future fusion reactors.

Nowadays, the sweep time of the FMCW reflectometer has reached an order of magnitude of microsecond. For example, the sweep time of reflectometer in Tore Supra is shortened to 2 μs with 1 μs dead time as shown in Fig. 2.16 [89]. In this case, the time response delay of VCO will be significant, as shown in Fig. 2.16(b). The time delay is 40 ns, which causes an error of 60 MHz for VCO's frequency and should be taken into account while dealing with the trigger time.

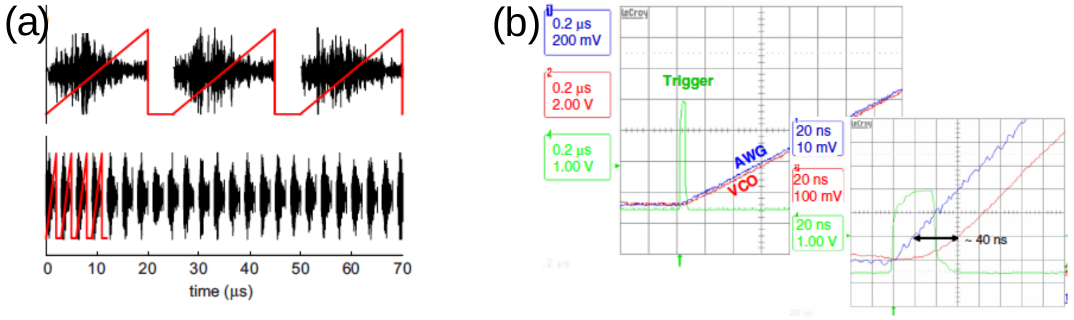

Figure 2.16: (a) Control voltage (red) and reflected signal (black). (b) A time delay between control voltage and VCO output [89].

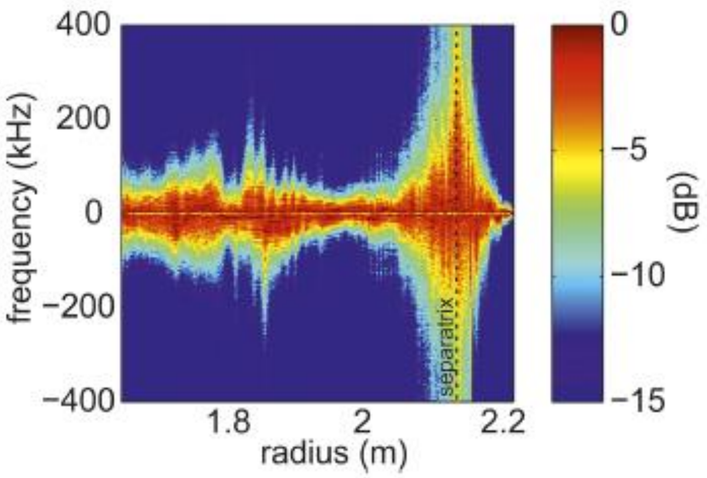

Figure 2.17: Radial evolution turbulence spectrum measured with a FMCW reflectometer in AUG [93].

Furthermore, as the signal of FMCW reflectometer can be seen as the equivalent of thousands of hopping frequencies, it can also provide the density fluctuation at high sweep rate. Figure 2.17 shows the turbulence spectrum obtained with FMCW reflectometer in ASDEX-Upgrade (AUG) of which sweep time is 1 µs with 0.25 µs dead time [93]. Since the sweep repetition of the system is 1.25 μs, the sampling rate of each probing frequency is 800 kHz and the observation frequency width of fluctuation is 400 kHz. The benefit of this method is not only wide band of frequency but also continuous radial measurement from the edge to the core.

In some big size tokamak, it is difficult to cover the whole density profile with only one band reflectometer. Thus, it is normal to use several reflectometers with different bands, or one system consisting of several independent reflectometers. In JET, for instance, a system consisting of four reflectometers which cover Q-, V-, W-, D-bands has been installed and the whole density profile is successfully reconstructed [91].

Another important application of the FMCW reflectometer is to realize real-time feedback control of the plasma position [98, 99]. Since the O-mode FMCW reflectometer doesn't rely on magnetic field, it can be used to measure edge density profile and control plasma positon in real time. A reflectometer-based plasma position feedback control demonstration has been accomplished in AUG [99], which uses the FMCW reflectometer to automatically reconstruct edge density profile and estimate the position of the LCFS. Figure 2.18 shows a demonstration experiment in which reflectometer based control was performed, and the reflectometer positon estimate shows a good overall match with magnetic separatrix.

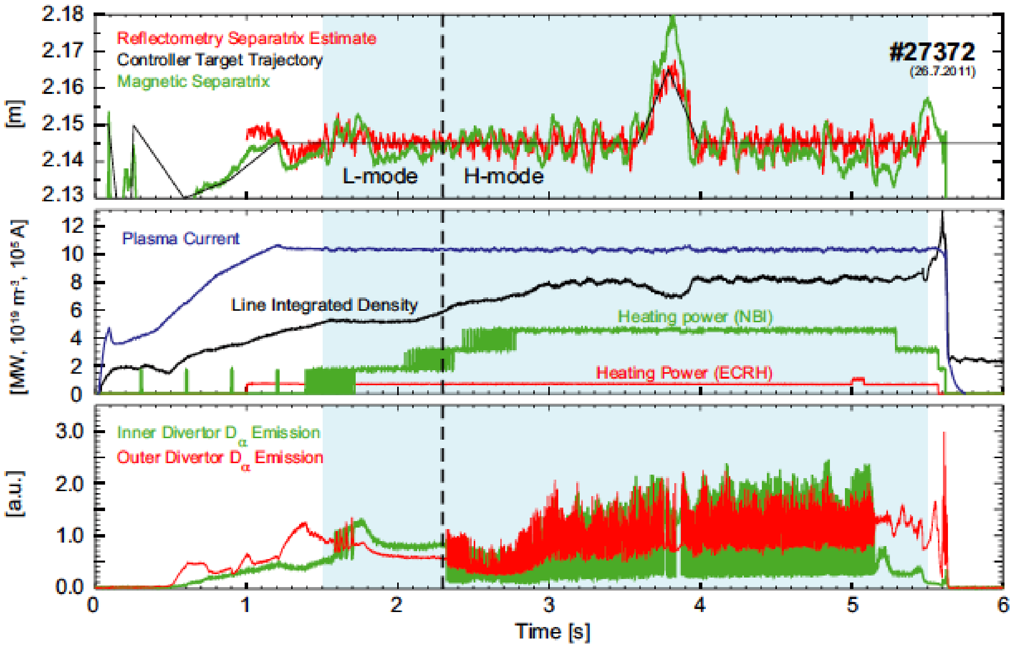

Figure 2.18: Time traces of the position controller target trajectory and of the magnetic and reflectometric separatrix positions (reflectometry based control was performed during the shaded period) [99].

2.4.2 System design and signal processing

Even though the temporal resolution of the FMCW reflectometer in Tore Supra is improved to several microseconds, how to increase the sweep rate and shorten the sweep period still remains a challenge for other FMCW reflectometers. To solve this problem, a comb sweep reflectometer, which is based on both FMCW reflectometer and comb reflectometer, has been developed in PANTA [100]. Compared with the FMCW reflectometers employed in other devices [85–97], the comb sweep reflectometer has the advantage of narrow frequency sweep range for each channel. Thus, the sweep period is short at the condition of same sweep rate. i.e., the temporal resolution is improved. Besides, as mentioned in Eq. (2.20), the absolute value of phase difference of comb reflectometer has an ambiguity of 2π

(m equals 1 or 2), which leads to the half-wavelength uncertainty of the cut-off layer location. This frequency comb sweep microwave reflectometer can also solve this problem.

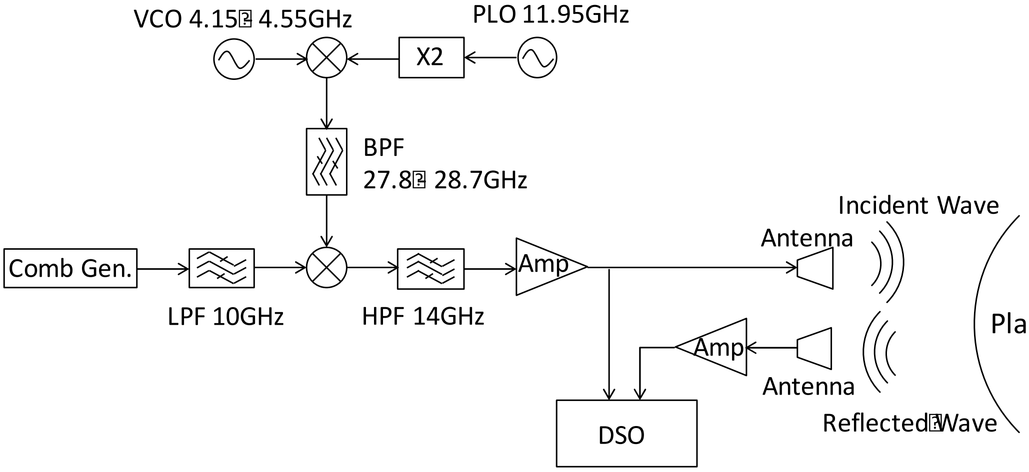

Figure 2.19: Block diagram of the frequency comb sweep microwave reflectometer system.

Figure 2.19 illustrates the circuit diagram of the comb sweep microwave reflectometer. The system is similar with the comb reflectometer except for the part where microwave signal is generated. The sweep frequency signal is generated by a VCO with a maximum sweep range of 0.5 GHz. After being mixed with a high-frequency (23.9 GHz) wave generated by a phase locked oscillator (PLO), the high-frequency sweep signal (28.0–28.5 GHz) is again mixed with the comb frequency signal and the comb sweep frequency microwave is generated. After being filtered and amplified, the signal is divided into two channels (reference channel and detecting channel), just as the comb reflectometer does.

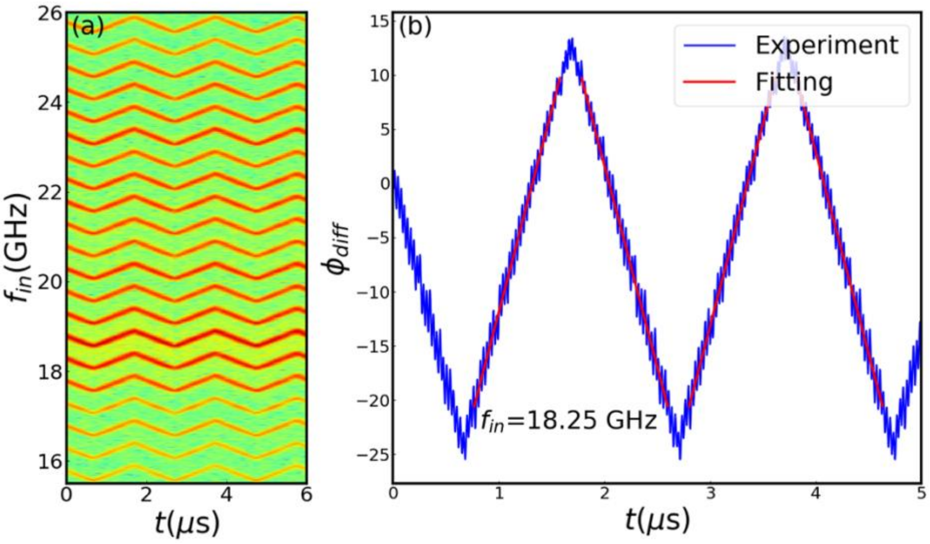

Fig. 2.20: (a) Time-frequency spectrum of incident wave. (b) Phase difference between incident and reflected waves and its linear fitting.

The time-frequency spectrum of the incident wave is presented in Fig. 2.20(a). It is clear that the entire frequency range of the system is from 15.5 to 26 GHz, with a frequency interval of 0.5 GHz. The output frequency of each channel is swept as triangular-wave. To distinguish the adjacent channels, the frequency sweep range of each channel is set to approximately 0.4 GHz (e.g., 18.05–18.45 GHz), and the incident frequency is regarded as the center of the sweep range (e.g., 18.25 GHz) for the calculations. The sweep period is approximately 2 μs, during which all incident channels share the same phase. The highest temporal resolution is therefore 2 μs.

Due to the time of flight of the incident wave, the frequency of the incident wave is different from that of the reflected wave at the antennas, and the beat frequency f_b between incident and reflected waves is finite. The time of flight can therefore be evaluated from f_b via the following process. A digital bandpass filter corresponding to the frequency sweep range of each channel (e.g., 18–18.5 GHz) is firstly applied to the original signal to obtain the single frequency channel signal $x_k(t)$, where k denotes the incident (in) or reflected (ref) wave. The instantaneous phase $\phi_k(t)$ is then obtained by applying Hilbert transform (see section 3.2) to $x_k(t)$. The phase difference between the incident and reflected waves is

$$\phi_{diff}(t) = \phi_{ref}(t) - \phi_{in}(t) \tag{2.25}$$

Fig. 2.20(b) presents the temporal evolution of $\phi_{diff}(t)$ at the incident frequency of 18.25 GHz. The absolute value of time derivate of ϕ_{diff} represents the beat frequency,

$$2\pi f_b = \frac{\left(\frac{d\phi_{diff}}{dt}\right)_{up} - \left(\frac{d\phi_{diff}}{dt}\right)_{down}}{2} \tag{2.26}$$

where $(d/dt)_{up}$ and $(d/dt)_{down}$ denote the time derivative of ϕ_{diff} in the frequency-rising and frequency-dropping phases, respectively, of the incident wave and are assumed to be constant during the sweeping period. In fact, $\phi_{diff}(t)$ appears to be linearly swept. To obtain the beat frequency more accurately, data of two sweep periods (i.e., 4 μs) are used to extract the beat frequency, and the red lines shown in Fig. 2.20(b) are obtained via linear fitting of $\phi_{diff}(t)$. The time of flight is therefore calculated as,

$$\tau = \frac{f_b}{df_{in}/dt} \tag{2.27}$$

where $2\pi f_{in} = d\phi_{in}/dt$ and $^{-}$ denotes an average over the period of incident frequency sweep ($\overline{df_{in}/dt}$ is typically $0.4\ \text{GHz}/1\ \mu\text{s} = 4 \times 10^{14}\ \text{Hz/s}$). The location of cut-off layer is determined according to the τ and the radial profile of electron density is thus reconstructed.

It is noted that the system can also be used to measure the azimuthal velocity while oblique incidence, and the Doppler shift is calculated as,

$$2\pi f_D = \frac{\left(\frac{d\phi_{diff}}{dt}\right)_{up} + \left(\frac{d\phi_{diff}}{dt}\right)_{down}}{2} \tag{2.28}$$

The azimuthal velocity is calculated according to f_D and the incident angle.

2.4.3 Benchmark test

The time of flight τ usually includes effects of unnecessary flight paths, e.g., distribution cables. Therefore, calibration is necessary to determine the distance between the target and the antenna, L. The microwave is injected toward a metal target. The value of f_b is found to be nearly the same and independent of the incident wave frequency f_{in} within a certain frequency range ($15.5\ \text{GHz} < f_{in} < 24\ \text{GHz}$, 17 channels), as shown in Fig. 2.21(a). Figure 2.21(b) illustrates the relationship between f_b and L at the incident frequency of 18.25 GHz. The result shows that f_b has a good linear relationship with L as expected.

While performing comb sweep reflectometer for plasma experiments, eliminate the beat frequency measured via benchmark test from the entire beat frequency of plasma experiment, and the rest part denotes the flight time of incident wave propagating the distance between the cut-off layer and the metal target. The location of the plasma cut-off layer is thus determined and density profile can be reconstructed.

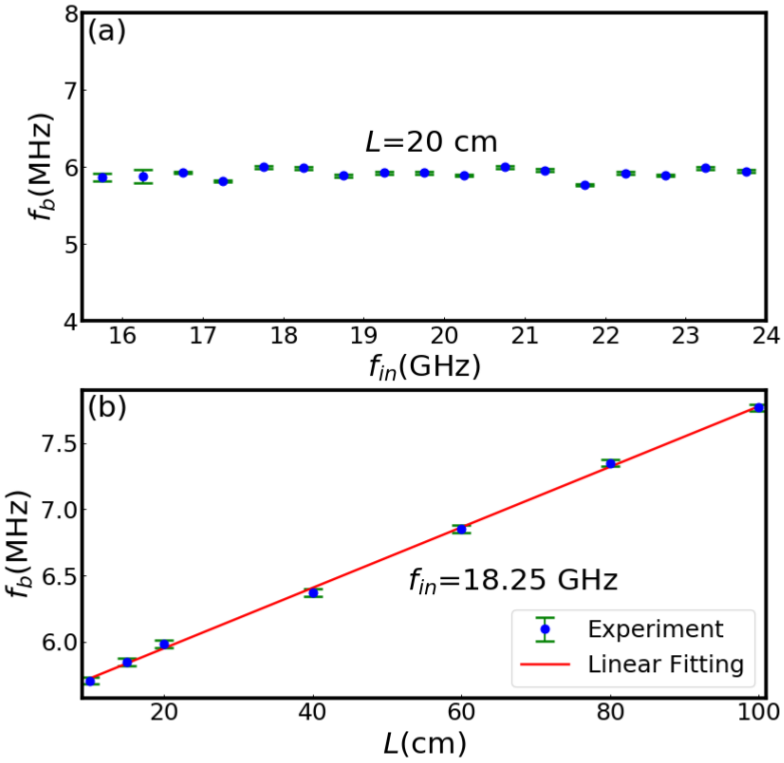

Figure 2.21: Relationship between (a) ϕ_{diff} and f_{in} and (b) ϕ_{diff} and L.

2.4.4 Density profile reconstruction

The density profile reconstructed with comb sweep reflectometer at the same condition with that of Fig. 2.13 ($P_{Heating} = 6$ kW, $B = 0.09$ T, $P_{gas} = 1$ mTorr) is shown as the green dots in Fig. 2.22. To fit the new profile, the density profile in Fig. 2.13 is modified and shown as the blue dots in Fig. 2.22. The modified density profile measured with comb reflectometer agrees well with the one measured with comb sweep reflectometer, and they are both consistent with the red dots which are measured with Thomson scattering. All the three profile reveal an extremely large density gradient at around $r = 4$ cm. This result indicates the reliability of comb sweep reflectometer.

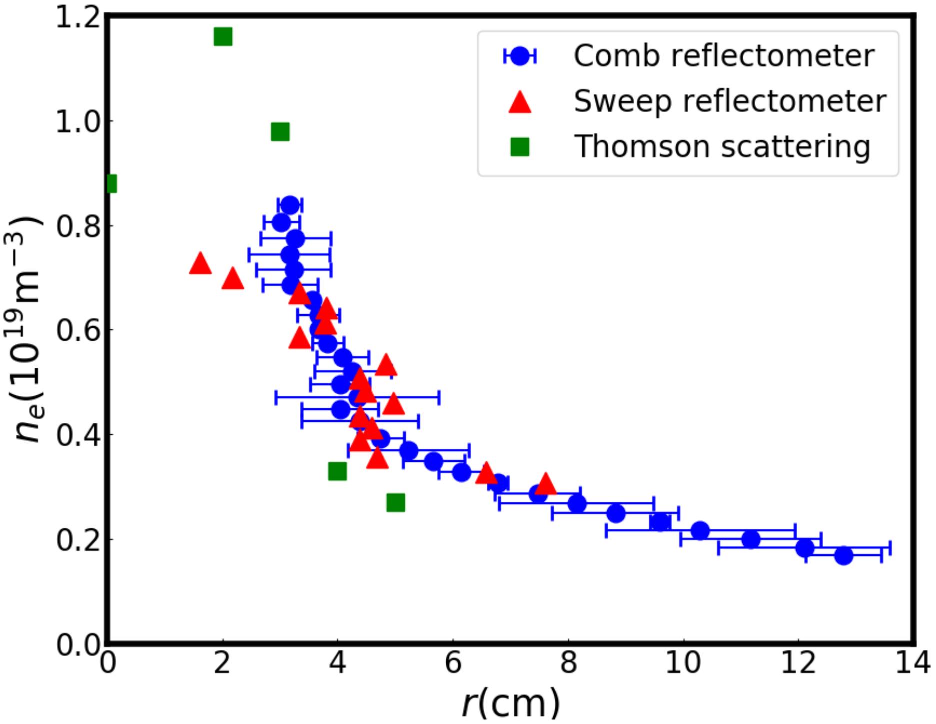

Figure 2.22: Profiles of electron density reconstructed with comb reflectometer, comb sweep reflectometer and Thomson scattering system.

Chapter 3

Development of data analysis methods for turbulence intermittency study

In experimental magnetized plasma research, different types of data are obtained from diagnostic systems, which contain the information we need. However, on the one hand, important information is hidden in raw signal and special processing is required to extract it. On the other hand, raw data contains noises as well. Thus, scientific and effective data analysis methods which can extract the information and reduce the impact of noises are essential. In this chapter, several data analysis methods developed for turbulence intermittency study are introduced.

3.1 Spectral analysis

Spectral analysis is one of the most used methods for analyzing time series data. The basic idea of spectrum analysis is that temporal signal can be decomposed into infinite series of trigonometric functions. Thus, the time-domain signal can be rewritten as frequency-domain signal, and frequency characteristics of raw signal can be studied. In this section, Fourier transform and spectral analysis methods are explained.

3.1.1 Fourier transform

Discovered by J. B. J. Fourier in 1807, Fourier transform of time series data $x(t)$ is defined as,

$$X(\omega) = \int_{-\infty}^{+\infty} x(t)e^{-i\omega t}dt \tag{3.1}$$

Here $\omega = 2\pi f$ is the frequency and $X(\omega)$ is the Fourier expression of $x(t)$ at frequency f. In general, $X(\omega)$ is a complex number, which contains the information of both amplitude and phase of frequency f. Thus, the original signal is decomposed into infinite series of trigonometric functions after performing Fourier transform, as shown in Figure 3.1 [101].

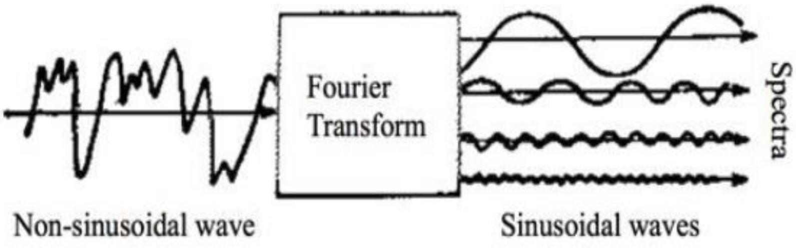

Figure 3.1: Image of Fourier transform [101].

The inverse Fourier transform is thus defined as,

$$x(t) = \frac{1}{2\pi}\int_{-\infty}^{+\infty} X(\omega)e^{i\omega t}d\omega \tag{3.2}$$

Since real experiment data is discrete and has finite length, discrete Fourier transform (DFT) is used to replace normal Fourier Transform. DFT of finite-time-length series data x_n $(n = 0, 1, \dots, N-1)$ is defined as,

$$X_m = \sum_{n=0}^{N-1} x_n e^{-\frac{i2\pi}{N}mn} \tag{3.3}$$

Here X_m $(m = 0, 1, \ldots, N-1)$ indicates the Fourier component of frequency $f_m = mf_s/N$, where f_s is the sampling frequency of raw data. The inverse discrete Fourier transform is defined as,

$$x_n = \sum_{m=0}^{N-1} X_m e^{\frac{i2\pi}{N}mn} \tag{3.4}$$

DFT of N-size data requires N^2 complex multiplications and $N(N-1)$ complex additions, which takes large time when N is large. Thus, fast algorithm for DFT is required. The history of the fast Fourier transform (FFT) algorithm can be traced to Gauss's work in 1805. Between 1805 and 1965, different versions of FFT algorithms were developed. In 1965, J. W. Cooley and J. W. Tukey developed a more versatile algorithm, which is generally credited to be the modern generic FFT algorithm and widely used in computation time [102]. Compared with the original DFT, Cooley and Tukey's FFT algorithm requires only $N/2 \log_2 N$ $(N = 2^M)$ complex multiplications and $N \log_2 N$ complex additions, which increases the calculation speed and brings smaller burden to computer.

3.1.2 Auto-power spectrum

The energy E of a temporal signal $x(t)$ is

$$E = \int_{-\infty}^{\infty} |x(t)|^2 dt \tag{3.5}$$

According to Eqs. (3.1) and (3.2), it is easy to obtain the following equation,

$$\int_{-\infty}^{\infty} |x(t)|^2 dt = \frac{1}{2\pi}\int_{-\infty}^{\infty} |X(\omega)|^2 d\omega \tag{3.6}$$

Thus, $|X(\omega)|^2$ indicates the energy of every frequency component. Since the energy of an infinite stochastic process is unintegrable, the power of sample signal with the time-length of T is finite:

$$\lim_{T\to\infty} \frac{1}{T}\int_{-T/2}^{T/2} |x(t)|^2 dt < \infty \tag{3.7}$$

Combined with Eq. (3.6), the power function $S_{xx}(\omega)$ is defined as,

$$S_{xx}(\omega) = \lim_{T\to\infty} \frac{1}{T}\langle X(\omega)X^*(\omega)\rangle \tag{3.8}$$

where $\langle\cdot\rangle$ denotes ensemble average and $X^*(\omega)$ is the complex conjugate of $X(\omega)$. Eq. (3.8) is thus called the auto-power spectrum density (PSD).

It is noted that the real experimental signal contains noise, which brings error to the PSD. An essential way to decrease the influence of noise is ensemble averaging. Large number of ensemble reduces the error contributed from noise effectively. Here gives an example. Figure 3.2(a) shows a test signal of $x(t) = \sin(2\pi f_1 t) + 2\sin(2\pi f_2 t) + \text{noise}$, where f_1, f_2 are 3 Hz and 9 Hz respectively, and noise denotes the white Gaussian noise with a standard deviation σ of 1. The PSDs of the signal, calculated with different numbers of ensembles, are given in Fig. 3.2(b). It is clear that two peaks exist at frequencies of 3 Hz and 9 Hz. At other frequency range, the influence of noise reduces when ensemble number increases. Figs. 3.2(c) and 3.2(d) give the convergence curves of the PSDs at different frequency. The horizontal axis is the inverse of the ensemble number. It is clear that at two frequencies where the trigonometric function is performed, the PSDs keep almost constant as the ensemble number increases. On the contrary, the PSDs at noise frequencies points (e.g. 5Hz and 15Hz) are proportional to the inverse of the ensemble number, and converge when the ensemble number increases until infinite. This result suggests that the increase of ensemble number has a significant effect on reducing the error of noise.

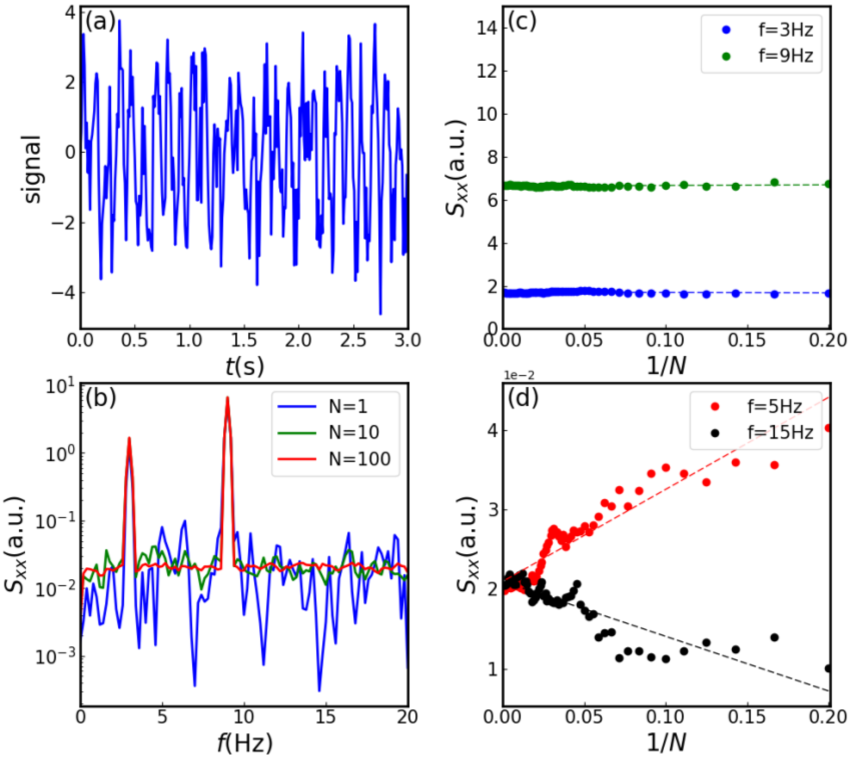

Figure 3.2: (a) Image of test signal. (b) Auto-power spectrum density of raw signal with different ensemble numbers. (c) and (d) Corresponding convergence curves of auto-power spectrum.

3.1.3 Cross-power spectrum and cross-coherence

Similar with auto-power spectrum, the cross-power spectrum density

(CSD) of two different signal $x(t)$ and $y(t)$ is defined as,

$$S_{xy}(\omega) = \frac{1}{T}\lim_{T\to\infty}\langle X^*(\omega)Y(\omega)\rangle \tag{3.9}$$

where $X(\omega)$ and $Y(\omega)$ are the Fourier expressions of $x(t)$ and $y(t)$, respectively. The squared cross-coherence is then defined as,

$$\gamma_{xy}^2 = \frac{\left|S_{xy}(\omega)\right|^2}{S_{xx}(\omega)S_{yy}(\omega)} \tag{3.10}$$

where $S_{xx}(\omega)$ and $S_{yy}(\omega)$ are the auto-power spectrum density of $x(t)$ and $y(t)$, respectively. This quantity γ_{xy}^2, which varies from 0 to 1, is used to evaluate the correlation intensity between the two signals. If the phase difference between two signals are constant, γ_{xy}^2 reaches 1, which indicates an ideal linear system between two signals.

Since the cross-power spectrum $S_{xy}(\omega)$ is complex, the cross phase is thus defined as,

$$\theta_{xy} = \tan^{-1}\frac{\mathrm{Im}\left[S_{xy}(\omega)\right]}{Re\left[S_{xy}(\omega)\right]} \tag{3.11}$$

The cross phase indicates the phase difference between two signals at frequency ω. The value of θ_{xy} is an ensemble averaged result.

Similar with auto-power spectrum, ensemble averaging can reduce the influence of noise effectively.

Here gives an example. $x(t)$, $y(t)$ and $z(t)$ are three test signals, $x(t) = 4\cos(2\pi f t) + \text{noise}$ ($f = 2$ Hz , $-20 < t < 20$), $y(t) = 2\cos(2\pi f t + \pi/2) + \text{noise}$, and $z(t) = 2\cos\left(2\pi f t + \pi/2 \times \mathrm{sgn}(t)\right) + \text{noise}$. Here, $\mathrm{sgn}(x)$ is a sign function,

$$\mathrm{sgn}(x) = \begin{cases} +1 & x \geq 0 \\ -1 & x \leq 0 \end{cases} \tag{3.12}$$

This means $y(t)$ is phase $\pi/2$ ahead of $x(t)$, while $z(t)$ is phase $\pi/2$ ahead of $x(t)$ for $t > 0$, and $\pi/2$ behind $x(t)$ for $t < 0$, i.e., the phase difference between $x(t)$ and $z(t)$ inverses at $t = 0$.

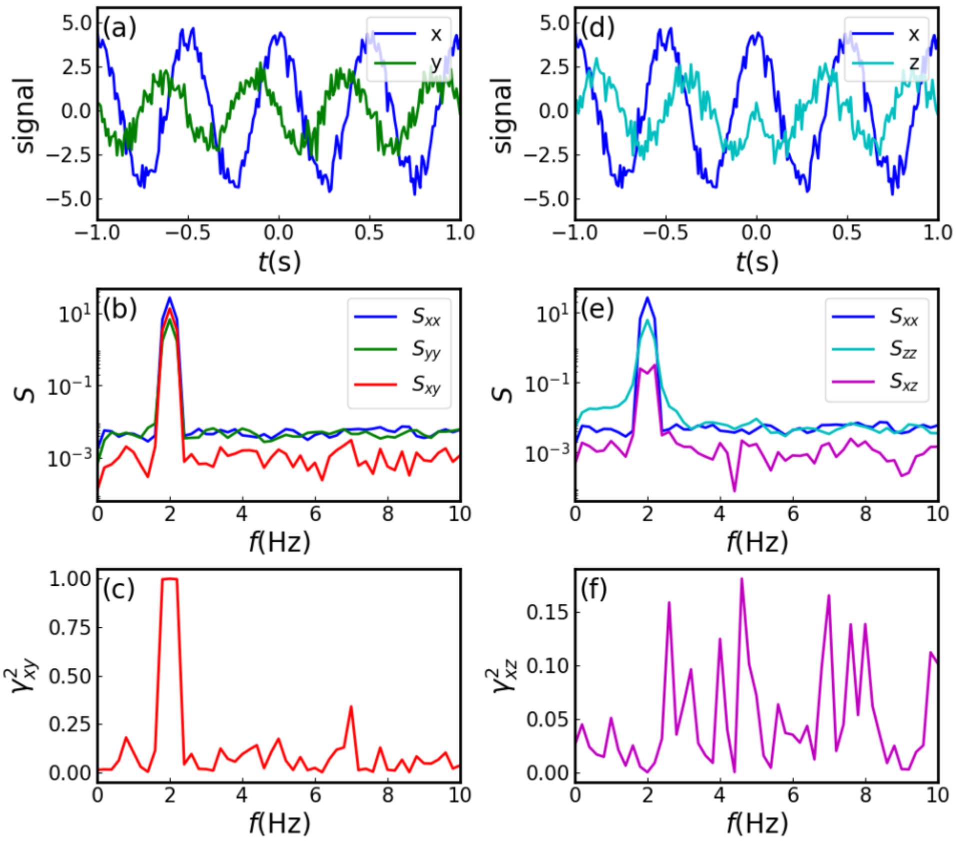

Figure 3.3: (a) Image of test signal $x(t)$ and $y(t)$. (b) Auto- and Cross-power spectrum density of $x(t)$ and $y(t)$. (c) Cross-coherence between $x(t)$ and $y(t)$. (d), (e) and (f) are corresponding results for $x(t)$ and $z(t)$.

The raw signals are shown in Figs. 3.3(a) and 3.3(d), respectively. Figure 3.3(b) shows the auto- and cross-power spectrum of $x(t)$ and $y(t)$, and Fig. 3.3(c) is the cross-coherence between $x(t)$ and $y(t)$. The power spectrums and cross-coherence of $x(t)$ and $z(t)$ are shown in Figs. 3.3(e) and 3.3(f), respectively. As shown in Figs. 3.3(b) and 3.3(c), the cross-power spectrum between $x(t)$ and $y(t)$ is strong at 2 kHz, and the cross-coherence is almost 1, indicating a strong correlation between the two signals at this frequency point. However, due to the inverse of phase difference at $t = 0$, the cross-power spectrum between $x(t)$ and $z(t)$ is weak at 2 kHz, and the cross-coherence is lower than 0.2, even though the auto-power spectrum density of $z(t)$ is almost the same as $y(t)$.

3.1.4 Bispectrum and bicoherence

The linear and quadratic statistics are the most important and basic tools for data analysis in science research. However, some signals have nonlinear processes which cannot be analyzed with linear and quadratic statistics, therefore high order statistics technology is required. In plasma research, the three-wave nonlinear coupling is essential for studying the interaction between turbulence and instabilities (e.g. geodesic acoustic mode/zonal flow) [103, 104]. To study the three-wave coupling, the bispectrum method was developed and applied to plasma turbulence by Y. C. Kim in 1979 [105].

The bispectrum is defined as,

$$B(f_1, f_2) = \langle X_1(f_1) X_2(f_2) X_2^*(f_1 + f_2) \rangle \qquad (3.13)$$

where X_1 and X_2 are the Fourier expressions of time series $x_1(t)$ and $x_2(t)$, respectively. If the phase between $X_1(f_1)$, $X_2(f_2)$ and $X_2(f_1 + f_2)$ is constant, the bispectrum becomes finite. On the contrary, if the phase is randomly changed, the bispectrum becomes zero.

The squared bicoherence is thus defined as,

$$b^2(f_1, f_2) = \frac{|B(f_1, f_2)|^2}{\langle |X_1(f_1) \times X_2(f_2)|^2 \rangle \langle |X_2(f_1 + f_2)|^2 \rangle} \tag{3.14}$$

and summed bicoherence is defined as,

$$b_{sum}^2(f_3) = (1/N) \sum_{f=f_1+f_2} b^2(f_1, f_2) \tag{3.15}$$

where $N = \sum_{f_3=f_1+f_2} 1$ is the ensemble number of $f_3 = f_1 + f_2$. Similar with cross-coherence, bicoherence varies from 0 to 1. If there is strong three-wave coupling, i.e. the phase of frequency component f_1, f_2 and f_3 meet the condition $\theta_3 = \theta_1 + \theta_2$, the bicoherence is close to 1.

It is noted that if X_1 and X_2 are calculated from the same signal (i.e. $x_1(t)$ and $x_2(t)$ are same), Eqs. (3.13) and (3.14) are called auto-bispectrum and auto-bicoherence, otherwise they are called cross-bispectrum and cross-bicoherence.

Here gives an example of bicoherence. Firstly, two cosinusoidal signals, $w_1(t) = \cos(2\pi f_1 t + \theta_1)$ and $w_2(t) = \cos(2\pi f_2 t + \theta_2)$, are given, where $-20 < t < 20$, $f_1 = 3\,\mathrm{kHz}$, $f_2 = 15\,kHz$, and θ_1 and θ_2 are two randomly chosen constants. If nonlinear three-wave coupling exists, the new wave has the following form:

$$\begin{aligned} w_3(t) &= \cos(2\pi f_1 t + \theta_1)\cos(2\pi f_2 t + \theta_2) \\ &= 0.5\cos(2\pi(f_1 + f_2)t + \theta_1 + \theta_2) \\ &\quad + 0.5\cos(2\pi(f_1 - f_2)t + \theta_1 - \theta_2) \end{aligned} \tag{3.16}$$

Thus, another wave without three-wave coupling is generated as well,

$$w_4(t) = 0.5\cos\big(2\pi(f_1 + f_2)t + \theta_3 \times sgn(t)\big) \\ + 0.5\cos\big(2\pi(f_1 - f_2)t + \theta_4 \times sgn(t)\big) \quad (3.17)$$

Two series of test data are generated by combining the four waves:

$$x(t) = w_1(t) + w_2(t) + w_3(t) + noise \quad (3.18)$$

$$y(t) = w_1(t) + w_2(t) + w_4(t) + noise \quad (3.19)$$

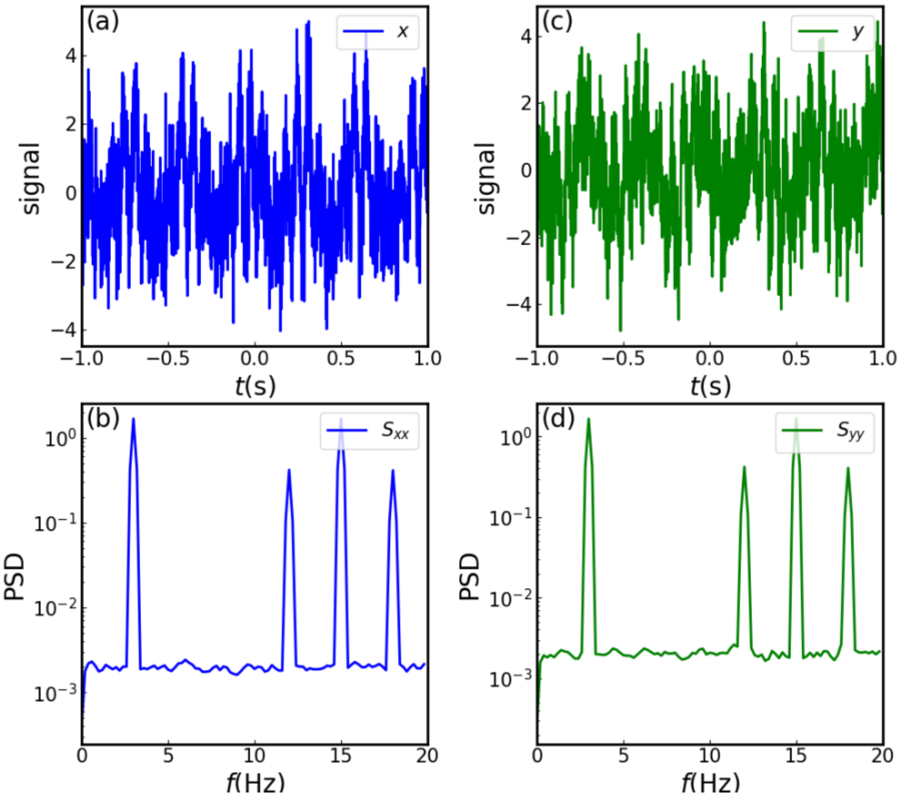

Figure 3.4: Image of test signal (a) $x(t)$ and (c) $y(t)$. (b) and (d) are corresponding auto-power spectrum density.

The pattern of the two test signals are shown in Figs. 3.4(a) and 3.4(c), respectively. Obviously, x and y have similar auto-power spectrum density, as shown in Figs. 3.4(b) and 3.4(d). The auto-bicoherence of $x(t)$ and $y(t)$ are presented in Figs. 3.5(a) and 3.5(b), respectively. The auto-bicoherence of $x(t)$ shows three-wave coupling at some frequency points, while auto-bicoherence of $y(t)$ shows no three-wave coupling. It is noted that a set of points in Fig. 3.5(a) are prominent, which is due to the symmetry of auto-bicoherence.

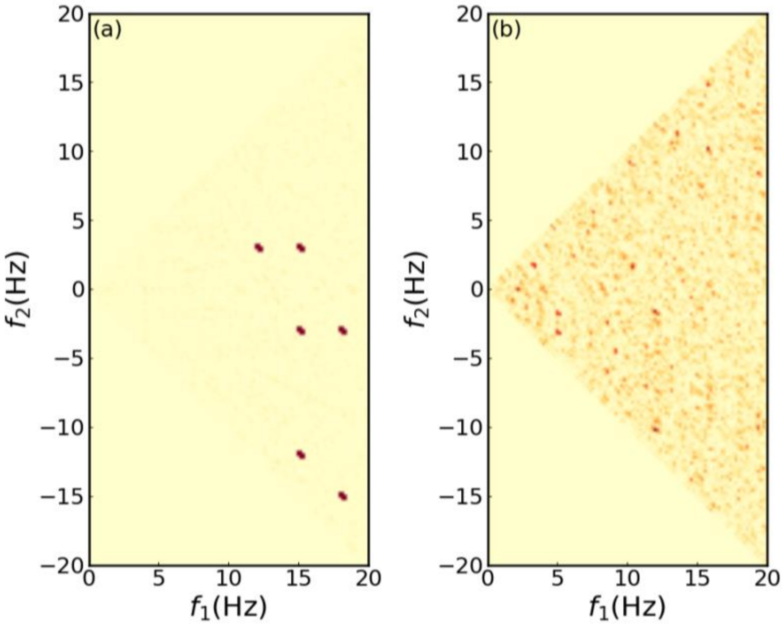

Figure 3.5: Auto-bicoherence of test data (a) $x(t)$ and (b) $y(t)$.

3.2 Hilbert Transform

The behavior of coherent envelopes of turbulence is important as it contains the information of interaction between ambient turbulence and instability [106]. There are several methods to extract the envelope from the signal, and the most common method is Hilbert transform.

The Hilbert transform of temporal signal $x(t)$ is defined as,

$$\hat{x}(t) = \mathcal{H}[x(t)] = \frac{1}{\pi}\int_{-\infty}^{\infty} \frac{x(\tau)}{t-\tau} d\tau \qquad (3.20)$$

The inverse Hilbert transform is thus written as,

$$x(t) = \mathcal{H}^{-1}[\hat{x}(t)] = -\frac{1}{\pi}\int_{-\infty}^{\infty} \frac{\hat{x}(\tau)}{t-\tau} d\tau \tag{3.21}$$

It is noted that the Hilbert transform is the convolution of the original signal $x(t)$ with $h(t)$,

$$h(t) = \frac{1}{\pi t} \tag{3.22}$$

Thus, the Hilbert transform is regarded as a linear filter with the impulse response $h(t)$. Conducting Fourier transform to $h(t)$ makes the following transmission function,

$$H(\omega) = -i\mathrm{sgn}(\omega) \tag{3.23}$$

Here, $\mathrm{sgn}(x)$ is the sign function defined as Eq. (3.12). The transmission function shows that Hilbert transform is to multiply the positive frequency component by $-i$, and to multiply the negative frequency component by i. In other words, Hilbert transform equals to a linear filter with phase shift of $\pi/2$, which shifts the phase of positive and negative frequency components by $-\pi/2$ and $\pi/2$, respectively. Thus, the analytical signal $y(t)$ is obtained by Hilbert transform,

$$y(t) = x(t) + i\hat{x}(t) \tag{3.24}$$

Since the phase difference between $x(t)$ and $\hat{x}(t)$ is $\pi/2$, according to Euler's formula, the instantaneous amplitude ($A(t)$) and phase ($\theta(t)$) of original signal $x(t)$ is obtained,

$$A(t) = \sqrt{x(t)^2 + \hat{x}(t)^2} \tag{3.25}$$

$$\theta(t) = \tan^{-1}\frac{\hat{x}(t)}{x(t)} \tag{3.26}$$

where $A(t)$ is the envelope of $x(t)$. The instantaneous frequency of original signal is also obtained,

$$f(t) = \frac{d\theta(t)}{2\pi dt} \tag{3.27}$$

3.3 Long-range correlation analysis

Long-range correlation (also called 'long-term storage' or 'persistence') and self-similarity are the key ingredients of the SOC dynamics, which may exist in turbulence intermittency [10]. In this subsection, several methods to evaluate the correlation and self-similarity are introduced.

3.3.1 Auto-correlation function

It is found that the characteristic of long-range correlation is associated with the long tail of auto-correlation function (ACF) of the raw fluctuation signal. The ACF, which evaluates the correlation of a signal with a delay copy of itself, is defined as,

$$R(\tau) = \overline{x(t+\tau)x(t)} \tag{3.28}$$

where $x(t)$ is the temporal signal and $\overline{x(t)}$ indicates the time average of $x(t)$. In real practice, it is more common to use normalized auto-correlation coefficient to replace auto-correlation function, which is defined as,

$$\rho(\tau) = \frac{\overline{\left[x(t) - \overline{x(t)}\right]\left[x(t+\tau) - \overline{x(t+\tau)}\right]}}{\sigma^2} \tag{3.29}$$

where σ^2 is the variance of $x(t)$. It is noted that the auto-correlation coefficient is an even function, and has a value between -1 and 1, where 1 indicates perfect correlation and -1 indicates perfect anti-correlation.

For real experiment data, auto-correlation coefficient equals 1 at $\tau = 0$, and decays as time lag increases. In some cases, the auto-correlation function decreases rapidly for short time lag, and decays slowly for long time lag. The figure of auto-correlation of this kind shows a sharp peak around $\tau = 0$ and a long decay tail as τ increases. This phenomenon is found to be associated with the long-range correlation and self-similarity characteristics of SOC behavior. However, it is difficult to evaluate the long-range correlation by auto-correlation function, and Hurst parameter is thus proposed. In the next two subsections, two methods to obtain Hurst parameter are introduced.

3.3.2 R/S analysis

Hurst parameter was firstly proposed to characterized the self-similarity of hydrological observations that do not obey Brownian motion by H. E. Hurst in 1951 [107]. Then B. B. Mandelbrot found the relationship between self-similarity and Hurst parameter, and developed the rescaled range (R/S) analysis to calculate Hurst parameter [108, 109]. In 1990s, B. A. Carreras improved the method and applied it to plasma turbulence research to study the self-similarity of the plasma fluctuations [110, 111].

The process of R/S analysis is carried out as follows. Firstly, given a time series x, $x = \{x_i: i = 1, 2, \dots, n\}$, which corresponds to a stationary process. The mean value and variance are $\bar{x}$ and $S^2(n)$, respectively. Thus, the R/S ratio is defined as,

$$\frac{R(n)}{S(n)} = \frac{\max(0, W_1, W_2, \dots, W_n) - \min(0, W_1, W_2, \dots, W_n)}{\sqrt{S^2(n)}} \tag{3.30}$$

where,

$$W_k = x_1 + x_2 + \cdots + x_k - k\bar{x} \tag{3.31}$$

The ratio $R(n)/S(n)$ is expected to scale as,

$$E\left[\frac{R(n)}{S(n)}\right] \xrightarrow{n\to\infty} \lambda n^H \tag{3.32}$$

where $E[x]$ denotes the expected value of x, and H is called Hurst parameter. H has a value between 0 and 1. $0.5 < H < 1$ indicates the existence of long-range correlation, while $0 < H < 0.5$ indicates long-range anticorrelation. The process is deterministic if $H = 1$, and the process is uncorrelated random if $H = 0.5$.

The robustness of R/S analysis has been considered by B. B. Mandelbrot [109] and B. A. Carreras [110]. A statistic process is considered to be robust if the statistic has strong anti-interference ability and does not drastically depend on the specific assumptions, i.e., the statistic process is reproducible. Carreras used the data of edge Langmuir probe to calculate Hurst parameters, and found that the profile of Hurst parameter was reproducible, which indicated the robustness of R/S analysis.

Besides, the accuracy of R/S analysis is considered as well. As mentioned before, the data sample to which R/S analysis is applied should be stationary. Concerning the non-stationary process data, W. H. Wang tested the result of R/S analysis [112]. A deterministic data generated by cosine function generator ($T = 0.1$ ms) was stacked to the stationary ion saturation current signal in HT-6M Tokamak, and R/S analysis was performed to the new series of data and Fig. 3.6 was obtained. It is clear that $H = 1$ for time delay $\tau < 0.1$ ms, and $H < 1$ for $\tau > 0.1$ ms. This result indicates that the non-stationarity of data has a significant influence on Hurst parameter obtained by R/S analysis, making H close to 1. Thus, testing the stationarity of data is necessary, and structure functions (SFs) analysis technology is developed.

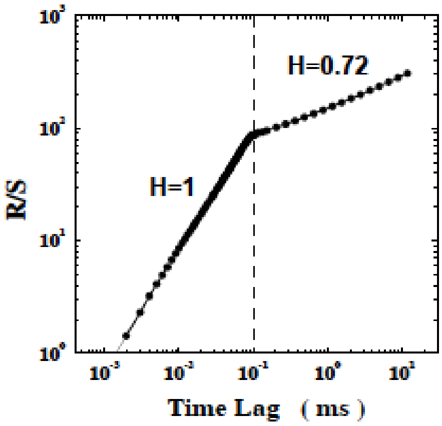

Figure 3.6: R/S analysis upon the stationary ion saturation current signal in HT-6M Tokamak, which was stacked by a cosine function ($T = 0.1$ ms) [112].

3.3.3 Structure functions analysis

Structure functions analysis was developed by C. Y. Xu [113], and the definition is as follows,

$$S_{x,q}(\tau) = \langle |x(t_i + \tau) - x(t_i)|^q \rangle \tag{3.33}$$

where $x(t)$ is a time series data of signal of interest, τ is the time lag, q is the order of structure function and i denotes the ith time point. If $x(t)$ is self-similar over a certain range of time lags $\tau_1 < \tau < \tau_2$, then the qth-order structure function is expected to scale as,

$$S_{x,q}(\tau) = \lambda_q \tau^{qH(q)} \tag{3.34}$$

where λ_q is constant and $H(q)$ is the Hurst parameter. The SFs analysis can be applied to either non-stationary process with stationary increments, or cumulative sums of stationary self-similar processes such as fractional Gaussian noise. In the latter case, $S_{x,q}(\tau)$ exhibits no scaling with time lag τ, i.e., $qH(q) = 0$ and $S_{x,q}(\tau)$ is constant. This phenomenon can be used to test the stationarity of the data [114]. In this case, Eq. (3.33) is rewritten by cumulative-summed structure function as,

$$S_{W,q}(\tau) = \langle |W(t_i + \tau) - W(t_i)|^q \rangle \tag{3.35}$$

where $W(t_k) = \sum_{i=1}^{k} x(t_i)$ is the cumulative value of $x(t_i)$. Replace $S_{x,q}(\tau)$ in Eq. (3.34) with $S_{W,q}(\tau)$, the Hurst parameter is determined.

3.4 Conditional averaging

For signals which are non-periodic (e.g. intermittent burst), Fourier transform is invalid, and conditional averaging is useful to extract the certain signal segments where events of interest exist. Different conditional averaging methods are based on different ways to determine the events. Here, two typical conditional average methods are introduced.

3.4.1 Threshold method

Threshold method is one of the easiest and most widely used methods of conditional averaging. To perform threshold method, a threshold is firstly set, which is usually several times the RMS of the reference signal. The events of interest, which are above the threshold, are thus discriminate. Then the maxima (or minima) peaks of all intermittent events are detected. As the peak is used as trigger to discriminate the timing of event of interest, it is called trigger function. Conditional average is achieved by accumulating and averaging the time series data around the triggers. If the maxima (or minima) detection and data averaging are applied on the same signal, it is called auto-conditional averaging. Otherwise it is called cross-conditional averaging.

Threshold method is widely used to obtain the intermittent burst signal in Plasma research, such as edge localized mode (ELM) [115] and blobs [116].

In my research, threshold method is used to extract the intermittent density burst, which is described in chapter 4.

3.4.2 Template method

Template method is firstly used for heartbeat analysis [117] and then applied in plasma research [118]. To perform template method, an initial template (written as $x_{k=0}(\tau)$, where i is the number of iterations,

$-T/2 < \tau < T/2$) is firstly constructed, which is usually obtained by choosing a trigonometrical function with a fundamental period T of the raw fluctuation signal $x(\tau)$. The cross-correlation $\rho_{k=0}(t)$ between the row signal and the initial template is thus calculated,

$$\rho_{k=0}(t) = \frac{\overline{\left[x(t+\tau) - \overline{x(t+\tau)}\right]\left[x_k(\tau) - \overline{x_k(\tau)}\right]}}{\sigma_x \sigma_{x_\mathrm{k}}} \tag{3.36}$$

where σ_x^2 and $\sigma_{x_k}^2$ are variances of $x(t+\tau)$ and $x_k(\tau)$, respectively. The cross-correlation is larger where the pattern of $x(\tau)$ is similar with the template. Therefore, by determining a threshold value, the peaks of correlation are detected. The peaks are used as trigger function as mentioned in last subsection, and the averaged signal (written as $x_{k=1}(\tau)$) is thus obtained by accumulating and averaging the time series data around the triggers, which is in the same way as template method. This is the initial iteration process. By using the averaged signal $x_{k=1}(\tau)$ as the new template, the iteration continues until the template converges. The last converged template is the signal after conditional averaging.

Threshold method is used to average the microwave signal in this research, which is described in Chapter 2.

Chapter 4

Study of Turbulence intermittency

As mentioned in Chapter 1, study of intermittency phenomenon is important for understanding the transport and improving the confinement of fusion plasma. Recently, a quasi-coherent fluctuation has been found excited in the central region of plasma in PANTA, where the density gradient is large. Although the fluctuation is localized and has a narrow structure, a global intermittent event can be observed in the whole plasma column including the peripheral weak-density-gradient region. To study the intermittent density bursts and quasi-coherent fluctuation, experiment has been performed in PANTA. The special advantage for studying intermittency in PANTA is that the magnetic field in PANTA is open, which is similar with the SOL region in torus device. Therefore, the physical mechanism of intermittency in PANTA is typical. This chapter will introduce the characteristics of the quasi-coherent fluctuation and the intermittent event and study its generation mechanism with microwave reflectometer.

The most important parameters for intermittent events in PANTA is the heating power, and the intermittent events are only observed in the case of high heating power. Thus, the parameters in this experiment are as follows: a heating power of 6 kW, a magnetic field of 0.09 T and a natural argon pressure of 1 mTorr. The duration of the discharge is 500 ms, and the microwave reflectometer starts the data acquisition from 100 ms of the discharge. Fig. 4.1 shows the signal of ion saturation current obtained by a 64-channel probe array at the mid-plane of 1875 mm in the axial direction and indicates that the plasma is stationary at the time during which the reflectometer collects data, as the red dashed lines denote. The density profile reconstructed by comb reflectometer in this condition is shown in Fig. 2.22, and a large density gradient exists around $r = 4$ cm.

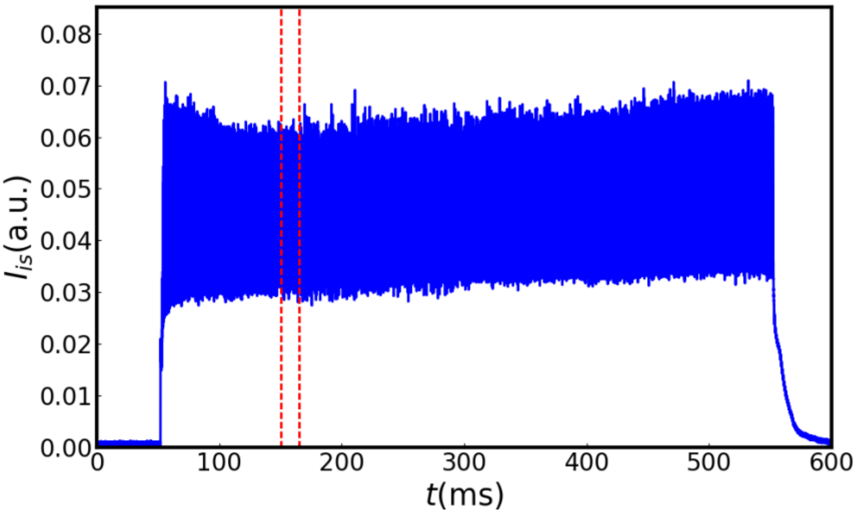

Figure 4.1: Ion saturation current obtained by probe.

4.1 Quasi-coherent fluctuation condition

A high frequency intermittent fluctuation for the phase difference of comb reflectometer is observed in this experiment. Figure 4.2 shows the spectrums of the phase difference perturbation $\tilde{\phi}$ at incident frequency $f_{in} = 22$ GHz ($r = 3.67$ cm). The results are obtained at high heating power ($P = 6$ kW) and low heating power ($P = 3$ kW), respectively. Both cases show the low frequency fluctuation component ($f \sim 2$ kHz). However, an intermittent component appears only at high heating power case, which has a higher frequency ($f \sim 10$ kHz). This component is called as quasi-coherent fluctuation hereafter. This quasi-coherent fluctuation is only excited in the case of high power heating (≥ 6 kW), and has a higher frequency than the drift wave frequency (which is usually < 5 kHz).

Fig. 4.3 shows the power spectrum in the whole frequency domain in log-log plot, which is similar with other experimental observations [10, 121]. Different regions of power spectra scale as power lows, indicating correlations on different time-scales. The f^{-2} decay of the power spectrum indicates a temporal process composed of uncorrelated increments (e.g. Brownian motion) [46, 122]. Actually, in the magnetized plasma turbulence, the high-frequency components (scaled as f^{-2}) in the time series correspond to small-size transport events. While the f^{-1} decay of the power spectrum is the distinctive feature of processes with long-range temporal correlations and often appears in conjunction with avalanche-like dynamics. In the PANTA, the f^{-1} decay of the power spectrum indicates correlation between large-scale bursts and small-scale fluctuations. Owing to similarity between the temporal and spatial spectra of turbulence in magnetized plasma, it is considered that spatial spectra of the PANTA plasma also indicate the power-laws within the corresponding range. These power laws are important signatures of the SOC systems [46].

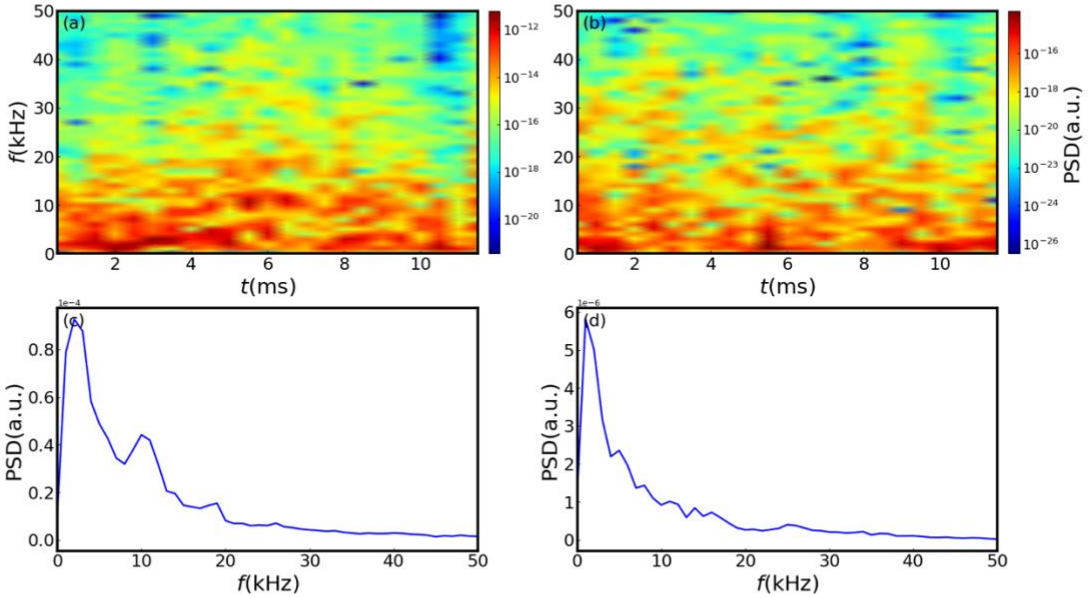

Figure 4.2: Time-frequency spectrum of $\tilde{\phi}$ at (a) $P = 6$ kW and (b) $P = 3$ kW. PSD of $\tilde{\phi}$ at (c) $P = 6$ kW and (d) $P = 3$ kW.

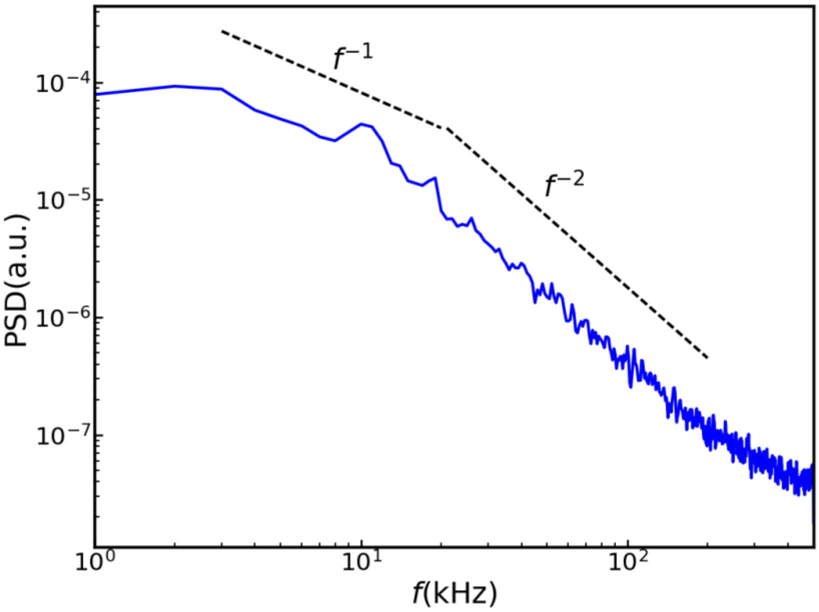

Figure 4.3: PSD of $\tilde{\phi}$ in log-log plot.

The radial profile of the quasi-coherent fluctuation strength is shown in Fig. 4.4. Figs. 4.4(b) and 4.4(c) are the radial profile of phase difference fluctuation level and density fluctuation level (calculated according to Eq. (2.21)), respectively. It is noted that because of the back-scattering in the fluctuation region, Eq. (2.21) no long works well in this narrow region [83] and a big error of the amplitude can exist in Fig. 4.4(c). In both Figs. 4.4(b) and 4.4(c) it is clearly shown that the strongest density fluctuation at $f = 11\ \mathrm{kHz}$ is located between $r = 3\ \mathrm{cm}$ and $r = 4.5\ \mathrm{cm}$ (denoted by the pink region), and this region is highly coincident with the large density gradient region. It is noted that the fluctuation strength decreases rapidly at the boundary of the large density gradient region. In addition, the formation of the strong gradient and excitation of the localized 11 kHz fluctuation in this region are confirmed by Langmuir probe measurement [120]. Thus, it is reasonable to conclude that the fluctuation is excited by the gradient.

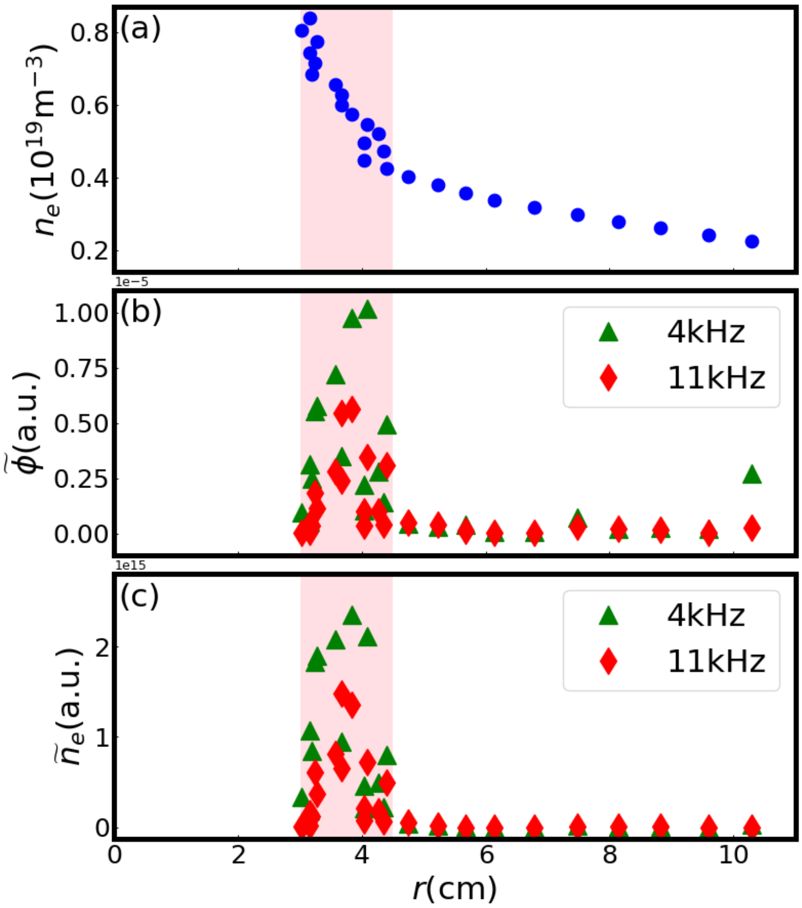

Figure 4.4: Radial profile of (a) electron density, (b) phase difference perturbation and (c) density perturbation.

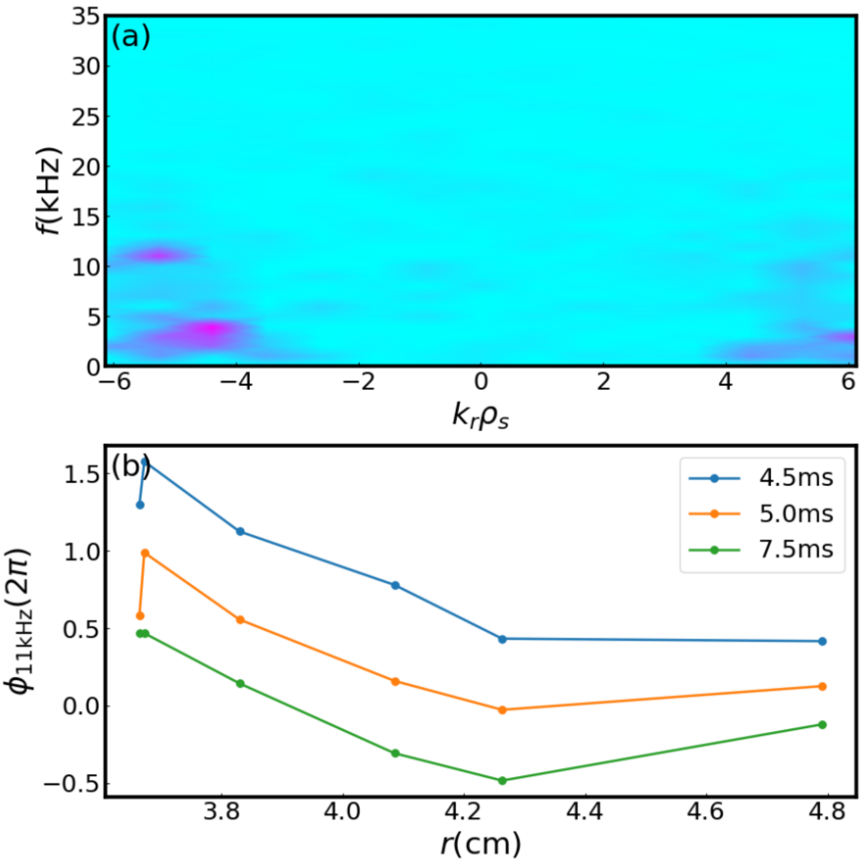

Figure 4.5: (a) Wavenumber spectrum. (b) Radial phase decay.

Figure 4.5 gives the radial wavenumber of the quasi-coherent fluctuation. Figure 4.5(a) is the radial wavenumber (k_r) spectrum calculated according to the cross phase of two radial channels at $r = 3.83$ cm and $r = 4.09$ cm [123]. In this analysis, the time window is 1 ms and 23 ensembles with an overlapping of 0.5 ms are used. The $\mathrm{k_r}$ is normalized by ion sound Larmor radius ρ_s ($\rho_s \sim 0.5$ cm in the PANTA). The k_r spectrum reveals an extremely large wavenumber of the quasi-coherent fluctuation, which is around -5.5 (i.e. -11 cm^{-1} without normalization), indicating that the fluctuation has a small scale and is a pure inward propagating mode rather than a standing wave propagating in two opposite directions. It is noted that negative indicates inward propagation of the fluctuation. Figure 4.5(b) shows the detailed results of radial phase decays of $f = 11\ \mathrm{kHz}$ fluctuation at different time, which is consistent with the k_r spectrum in Fig. 4.5(a). This may help to identify the fluctuation, however, what the quasi-coherent fluctuation still remains unknown by now.

4.2 Evaluation of intermittency

During the quasi-coherent fluctuation experiment, the intermittent density burst is observed as well. As mentioned in subsection 2.3.2, density fluctuation is represented by phase difference perturbation $\tilde{\phi}$, and a decrease in the phase (i.e., distance between antenna and cut-off layer shortens) denotes an increase in the electron density. Thus, we study the density intermittency with the phase perturbation in this subsection.

4.2.1 Spatial-temporal evolution of intermittency

The spatiotemporal evolution of $\tilde{\phi}$ is shown in Fig. 5. In the region of $3.0 \leq r \leq 4.3\ \mathrm{cm}$, amplitude of $\tilde{\phi}$ is dominated by the quasi-coherent fluctuation. Amplitude of the quasi-coherent fluctuation changes abruptly with short time-scale (~ 0.1 ms). It is observed that sudden increases/decreases in the amplitude of the $\tilde{\phi}$ are radially synchronized beyond the outward boundary of the quasi-coherent fluctuation. There is a phase jump around $r = 4.3\ \text{cm}$ close to the outward boundary of the quasi-coherent fluctuation. A ballistic propagation or avalanche-like propagation can be observed at outer region. A decrease of $\tilde{\phi}$ starts from around 6.1 ms, and propagates from the central region ($r = 4.3\ \text{cm}$) to peripheral region ($r = 9\ \text{cm}$), indicating the intermittent burst is a global event. It is noted that a decrease in the phase (i.e. the distance between antenna and cut-off layer shortens) denotes an increase in the local electron density. The density burst originates from the outward boundary of quasi-coherent fluctuation region, which indicates that the fluctuation may contribute to the generation of intermittency. It is also noted that the $\tilde{\phi}$ associated with the intermittent event in the peripheral region ($4.3 \le r \le 9\ \text{cm}$) has an anti-phase to the $\tilde{\phi}$ in the quasi-coherent fluctuation region.

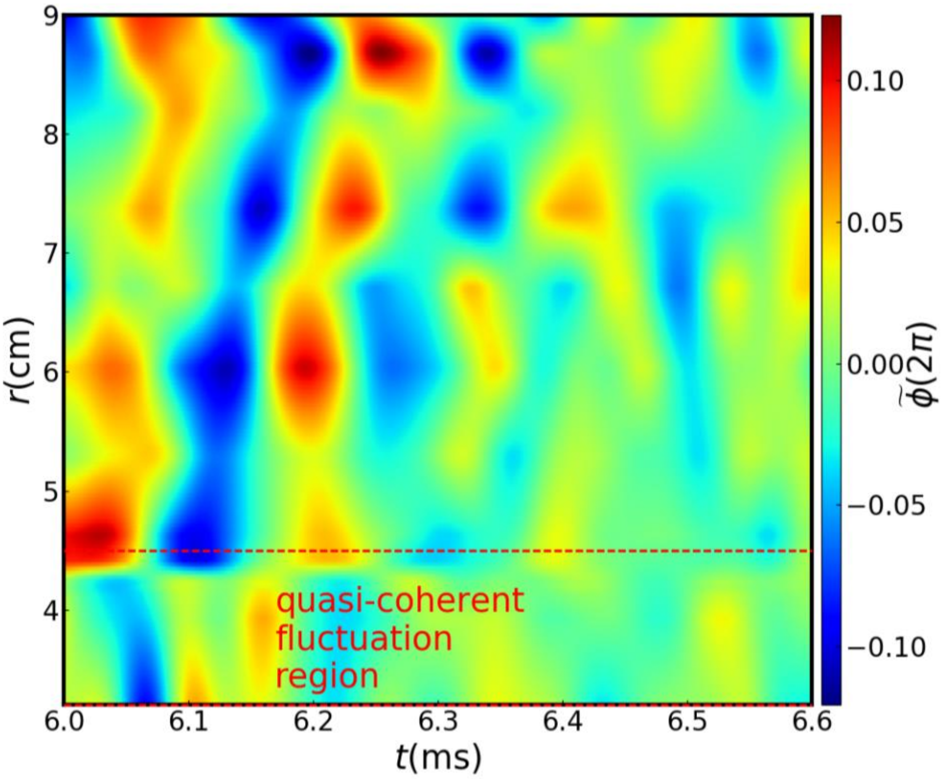

Figure 4.6: Spatial-temporal evolution of phase difference perturbation.

To investigate the transport of intermittency, it is necessary to separate the intermittent bursts from background turbulence. Threshold conditional analysis mentioned in subsection 3.4.1 is thus used to extract these intermittent features. In this experiment, a threshold of $-1.5 \times \mathrm{RMS}$ of $\tilde{\phi}$ at $r = 5.67$ cm is used to discriminate the intermittent events and to detect the minima. The peaks of the bursts which are smaller than the threshold are used as triggers, as shown in Fig. 4.7. The time window for conditional averaging is 160 μs, which is several times the decorrelation time of intermittent bursts (discussed later). It is noted that the detected adjacent two triggers are separated at least 80 μs (half the time window for averaging) to avoid overlapping of two adjacent bursts. The $\tilde{\phi}$ of all channels at different radii are averaged based on the triggers of reference channel and the time window, and the auto- and cross-conditional averaging results at different radii are shown in Fig. 4.8.

Similar with Fig. 4.6, the phase difference decreases, i.e., density increase, is observed formed in the central region and propagating outward in the peripheral region. This means that density bump associated with intermittent event propagates outward from $r = 4.5$ cm and has a global structure. It is also noted that inside the $r = 4.3$ cm, the phase difference increases before intermittency bursts, indicating the density hole is generated in the inner region before the outward propagation of the density bump.

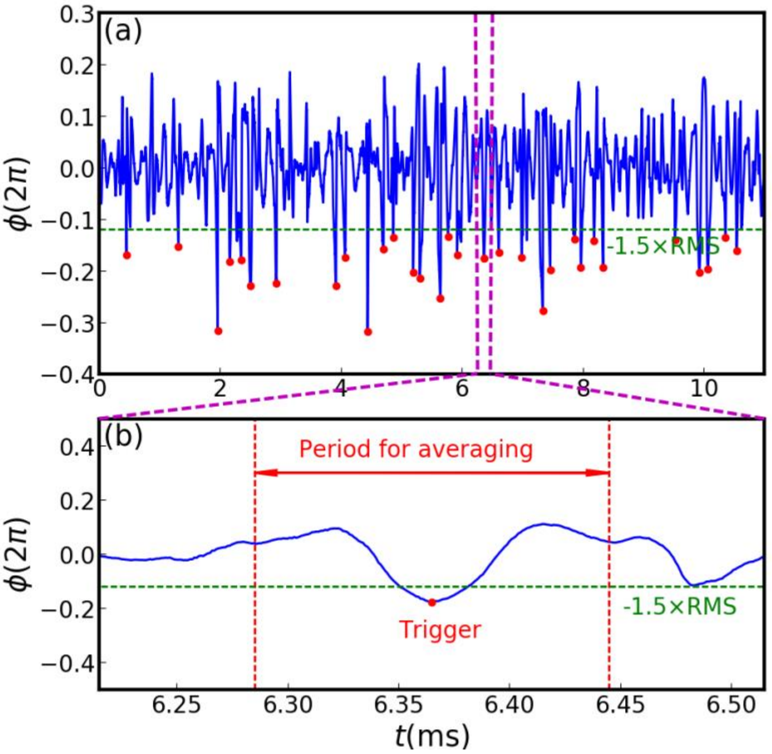

Figure 4.7: (a) Threshold and triggers for conditional averaging. (b) is the magnified one.

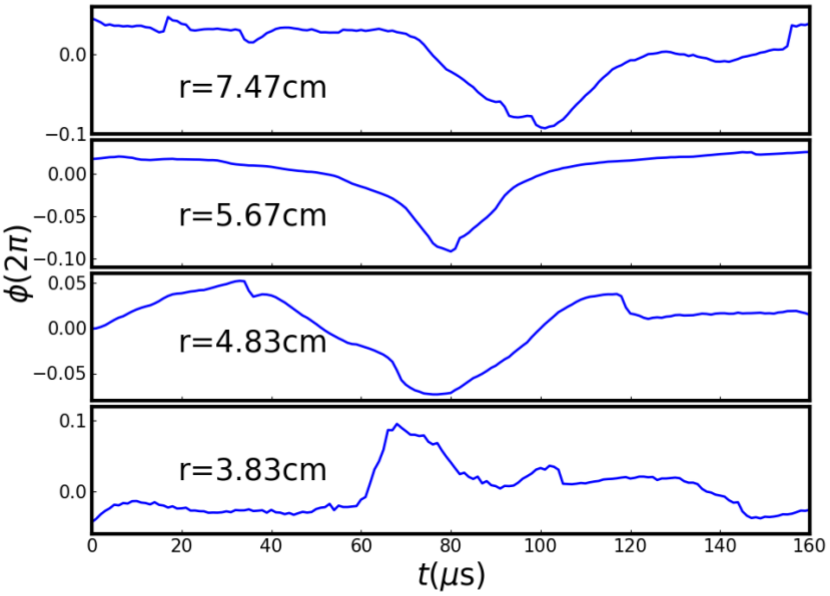

Figure 4.8: Conditional average of $\tilde{\phi}$ at different radial positions.

It is also noted that the outward propagation velocity of the intermittent density burst, which is calculated according to the time delay of phase holes at different radii in peripheral region. The velocity between $r = 4.5$ cm and $r = 7.5$ cm is much larger, revealing a velocity of around 1 km/s, which is consistent with that in other devices [11, 12, 16–19, 25–27, 30]. However, at the region outside of $r = 7.5$ cm, the outward propagation of the intermittency slows down, which reveals a velocity of around 500 m/s as shown in Fig. 4.6.

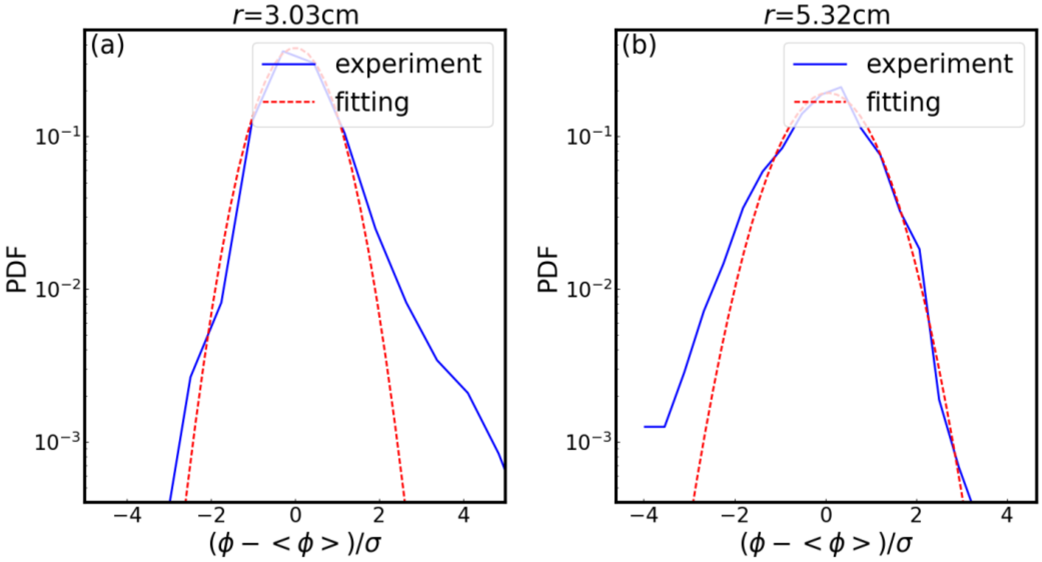

Figure 4.9: Distributions of phase perturbation $\tilde{\phi}$ at (a) inner and (b) outer regions.

To get the statistic properties of the intermittent bursts, the technique of probability distribution function (PDF) is performed to the phase perturbation $\tilde{\phi}$. The distributions of the $\tilde{\phi}$ at different radii are calculated, which is shown in Fig. 4.9. Figs. 4.9(a) and 4.9(b) show the distributions at the inner ($r < 4$ cm) and outer ($r > 5$ cm) regions, respectively. It is clear that at inner region, the positive phase perturbation (corresponding to density hole) are dominant. On the contrary, the PDF at outer region deviates to a negative value, indicating the density burst events exist in the peripheral region.

To evaluate the deviation of PDFs from Gaussian distribution, the skewness and kurtosis are calculated. The definition of skewness S and kurtosis K are,

$$S = \langle \tilde{x}^3 \rangle / \langle \tilde{x}^2 \rangle^{3/2} \tag{4.1}$$

$$K = \langle \tilde{x}^4 \rangle / \langle \tilde{x}^2 \rangle^2 - 3 \tag{4.2}$$

where $\tilde{x}$ is the fluctuation of time series data $x(t)$. S is the third-order moment of the PDF which describes the asymmetry of PDF, and K is the fourth-order moment of the PDF, evaluating the tail weight of PDF. For the data which obeys ideal Gaussian distribution, both S and K are close to 0. In this experiment, the skewness and kurtosis of phase perturbation are calculated.

Fig. 4.10(a) shows the profile of skewness, which illustrates a positive value at inner region and a negative value at outer region. Figure 4.10(b) gives the kurtosis profile, which, as radius increases, decreases at inner region and increases at outer region. It is noted that the inversion layer of skewness, located around $r = 4.3$ cm, is highly coincident with the origin position of outward propagation of intermittent bursts in Fig. 4.6, which indicates the birth region of intermittency. Moreover, the birth region is located inside the quasi-fluctuation region (denoted by the pink region), which suggests that the quasi-coherent fluctuation contributes to the generation of intermittency. At the inversion layer, the kurtosis values are close to zero aw well, indicating the PDF of perturbation at inversion layer is close to Gaussian distribution. This result again suggests that the fluctuation is correlated with the birth of density bumps and holes.

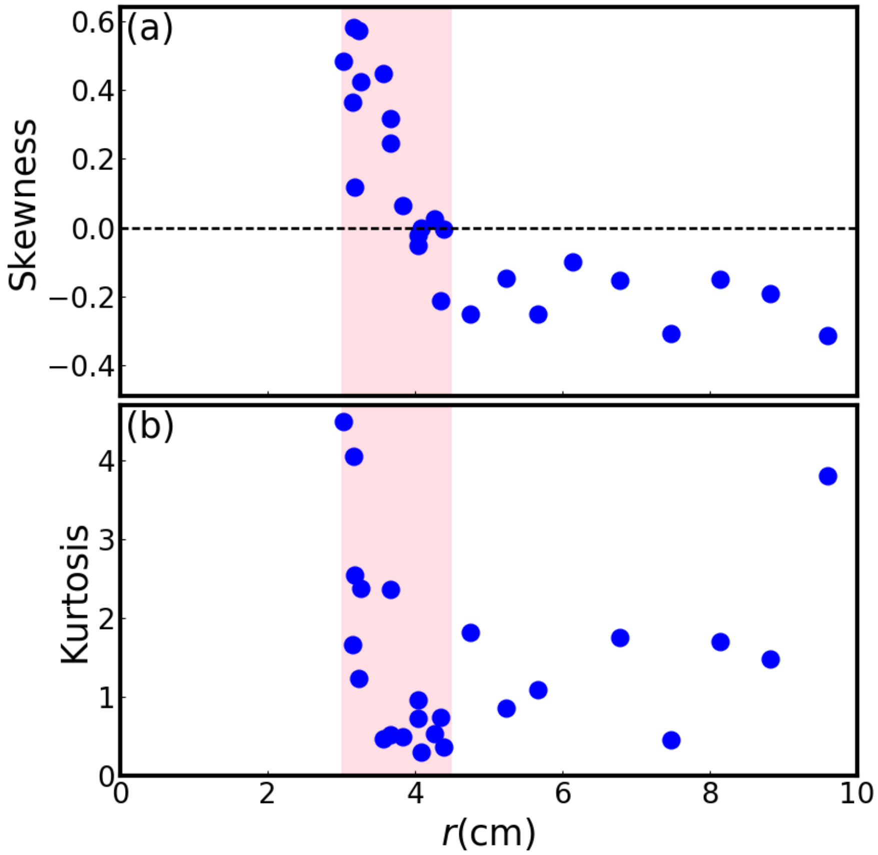

Figure 4.10: Radial profiles of skewness (a) and kurtosis (b) of phase perturbation $\tilde{\phi}$.

Intermittent behavior in the outer region ($4.5 \leq r \leq 10$ cm) is correlated to the abrupt increase in the amplitude of quasi-coherent fluctuation excited in the large gradient region ($3 \leq r \leq 4.5$ cm). Figure 4.11 gives the radial correlations of $\tilde{\phi}$. Figs. 4.11(a) and 4.11(b) show the cross-power spectrum density and cross coherence of fluctuations across the inversion, respectively. Besides, Figs. 4.11(c) and 4.11(d) show the corresponding results of fluctuations both at peripheral region. The strong radial correlation at the mode frequency of 11 kHz is clearly shown not only across the large gradient region (Fig. 4.11(b)) but also at 2–3 cm outside far away from that region (Fig. 4.11(d)) as well.

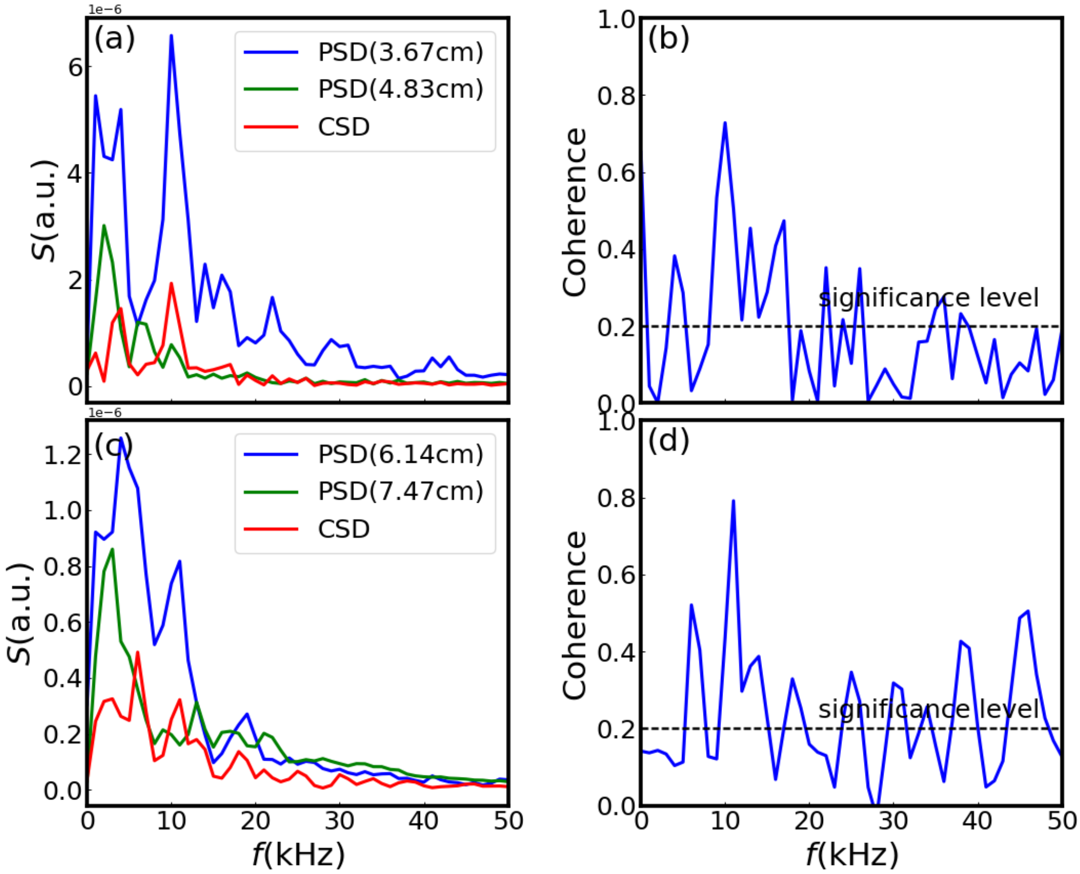

Figure 4.11: (a) Auto- and cross-power spectrum density and (b) cross coherence of phase difference perturbations across the inversion layer. (c) Auto- and cross-power spectrum density and (d) cross coherence of phase difference perturbations at peripheral region.

4.2.2 Long-range correlation of intermittency

Long-range correlation is the key ingredients of the SOC behavior, which can be evaluated from the ACF. The ACFs of phase difference perturbation $\tilde{\phi}$ at $r = 3.16\ \mathrm{cm}$ and $r = 5.32\ \mathrm{cm}$ are shown in Fig. 4.12. The dashed lines are eye-guide lines (exponential decay: $y = e^{-t/\tau}$

and Lorentzian-like long tail: $y = 1/(1 + (t/\tau)^2)$). It can be seen that the ACF of $\tilde{\phi}$ at $r = 3.16$ cm shows a narrow peak when time lag is smaller than 0.1 ms and a slow decay tail when time lag is larger than 0.1 ms, indicating the existence of long-range time correlation. The decorrelation time, which is denoted by the time delay after which the ACF decays lower than $1/e$, is approximately 40 μs. On the contrary, the ACF measured at 5.32 cm drops rapidly with time and shows no long tail, which suggests there is no long-rang correlation at peripheral region.

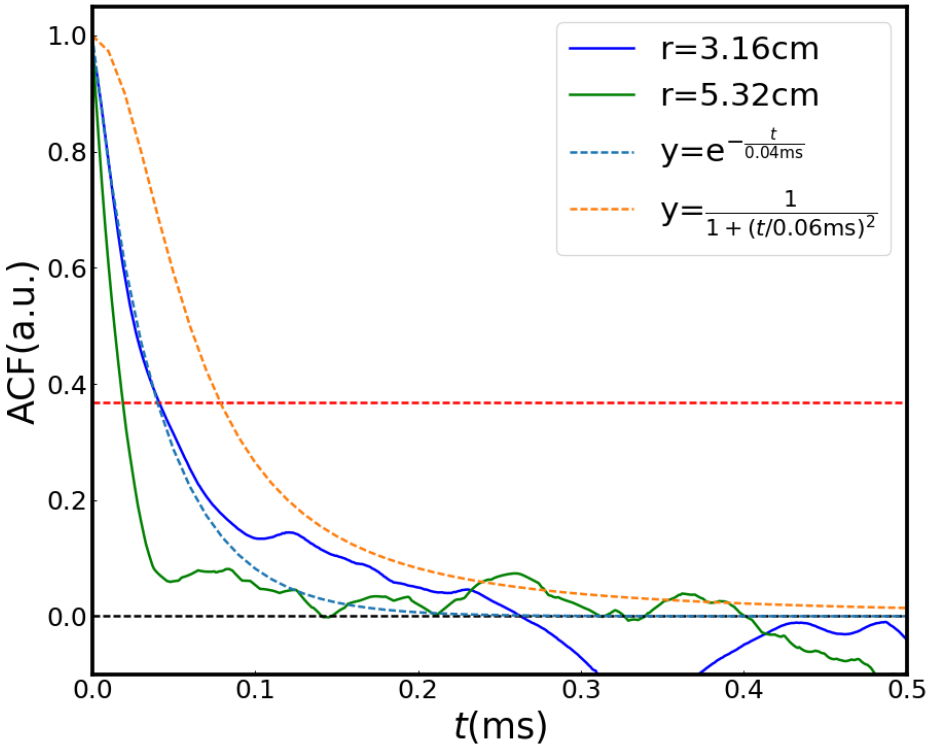

Figure 4.12: Auto-correlation function of phase difference perturbation.

To evaluate the long-range correlation of $\tilde{\phi}$ more accurately, Hurst exponents H are evaluated. As mentioned in section 3.3, it is necessary to test the stationarity of the data samples with structure function method before calculating H. Figure 4.13 shows the structure functions of the phase difference perturbation for different orders ($q = 0.5, 1.0, 2.0, 3.0$) at $r = 4.35$ cm. It is clear that $S_{x,q}(\tau)$ is approximately constant with zero slope for all orders for τ between 50 μs and 3 ms, which indicates that the data are stationary during this period. The data of this period is thus used to calculate Hurst exponents.

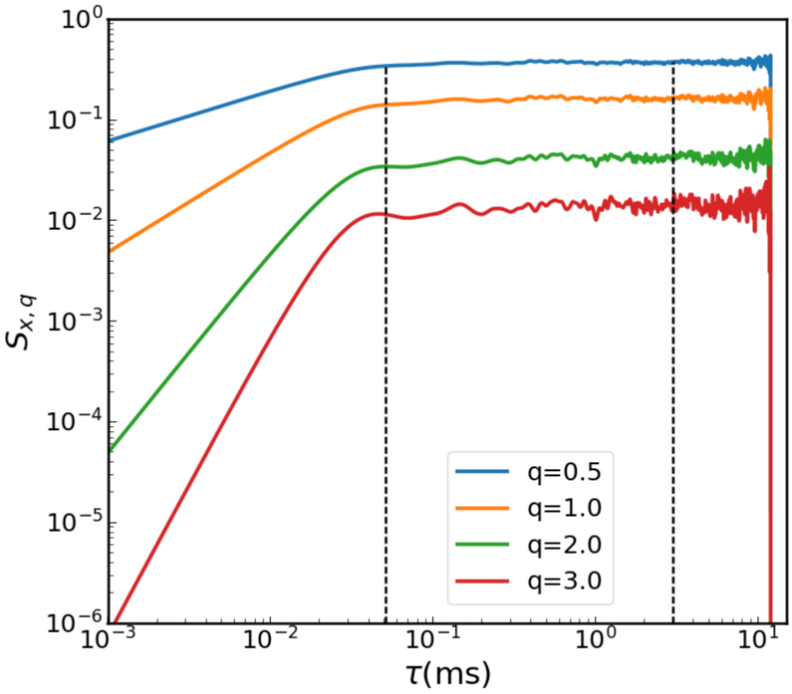

Figure 4.13: Structure functions of phase difference perturbation for different orders.

Both structure functions and R/S methods are used to calculate the Hurst component. Figs. 4.14(a) and 4.14(b) are the cumulative-summed structure functions and R/S values of $\tilde{\phi}$ versus time lag at $r = 4.35$ cm, respectively. From both figures, it is shown that there is a transition at time lag $\tau = 50$ μs. For time lags smaller than 50 μs, the slope of linear fitting of SFs and R/S values gives a Hurst exponent of larger than 0.8. This large H is due to the non-stationarity of phase perturbation and should be neglected. For larger time lags ($\tau > 50$ μs) where the phase perturbation is stationary, $H = 0.740$ and $H = 0.722$ are determined from the slopes of linear fitting of R/S values and SFs, respectively. These two values are consistent with each, indicating the agreement of the two methods for getting Hurst exponents.

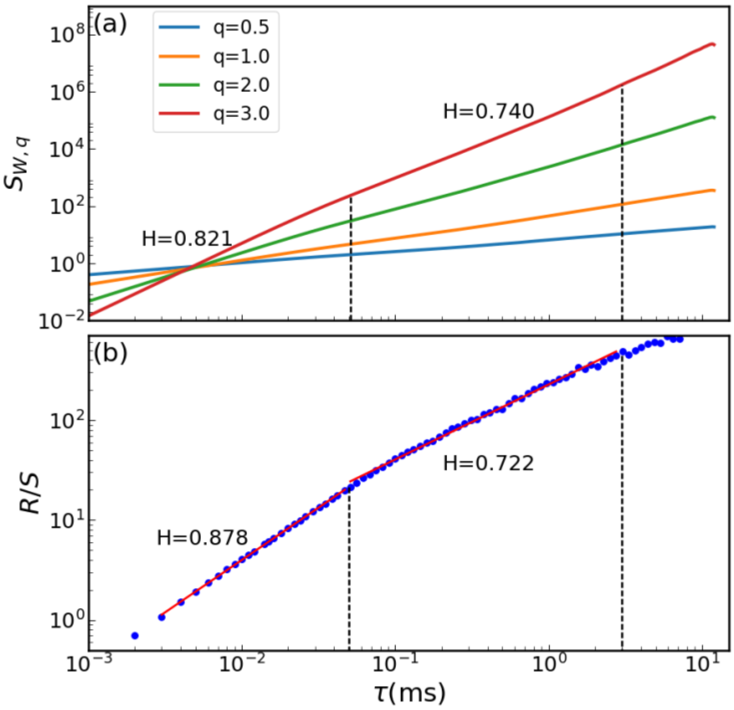

Figure 4.14: (a) Cumulative-summed structure functions and (b) R/S values of $\tilde{\phi}$ versus time lag for calculating Hurst exponents.

After calculating H of all channels, the radial profile of Hurst exponents is obtained and presented in Fig. 4.15. It is clear that at the region where the quasi-coherent fluctuation is located ($3.0 \leq r \leq 4.5$ cm denoted by the pink region), the Hurst exponent is larger than 0.7, and the largest Hurst exponent reaches around 0.8. In contrast, the Hurst exponents out of $r = 4.5$ cm are mostly between 0.6 and 0.7. This result indicates that the density bursts at the quasi-coherent fluctuation region has long-range time correlation and SOC dynamics exist in this region. Since the intermittency originates from the outward boundary of this region (Fig. 4.6), it is thus reasonable to speculate that the origin of intermittent density burst propagation is driven by SOC dynamics when the critical threshold is reached due to the quasi-coherent density fluctuation.

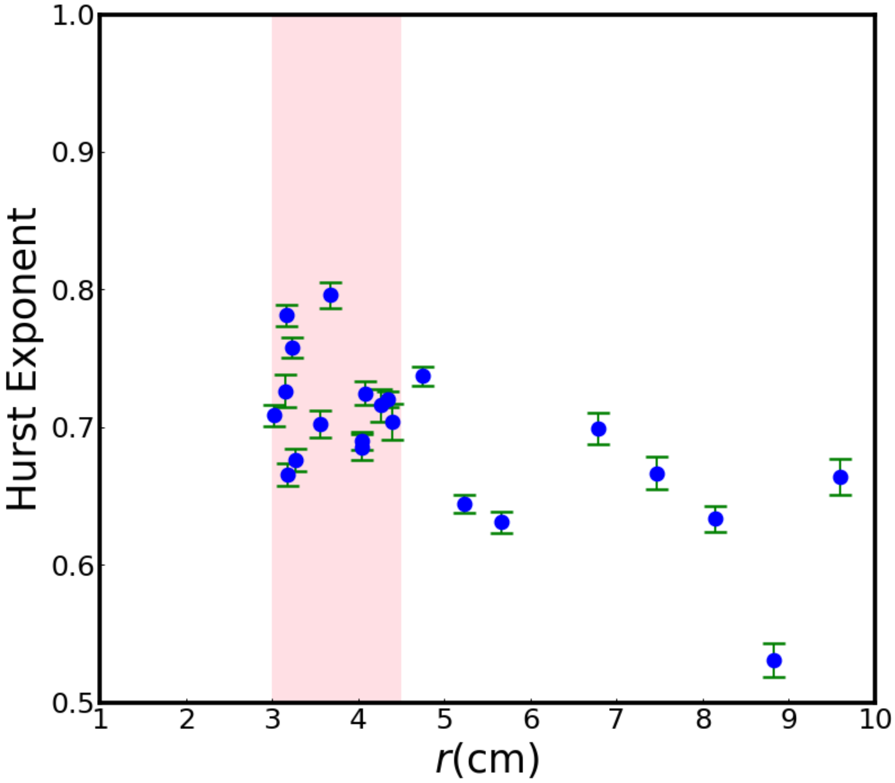

Figure 4.15: Radial profile of Hurst exponents. The error bars indicate the standard deviation of R/S values about the linear fitting.

4.2.3 Discussion

The Hurst exponent inside the quasi-coherent fluctuation region shows a value larger than 0.7, signifying the long-range correlation chapter of the perturbation at this region. Besides, the f^{-1}-type spectrum shows a correlation with the avalanche-like transport [44–48, 124, 125]. Both of them are consistent with plasma transport dominated by SOC dynamics.

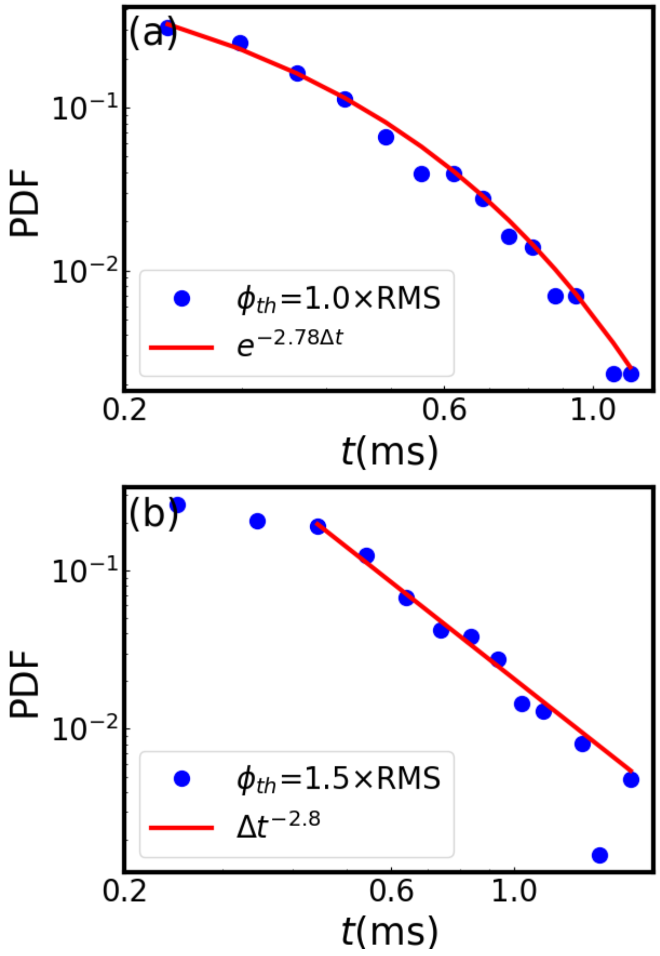

Figure 4.16: PDF of waiting time for intermittent bursts with a threshold of (a) $1.0 \times$ RMS and (b) $1.5 \times$ RMS.

Recently, the statistical analysis of waiting time Δt, which stands for the duration between two adjacent bursts, is used to understand the behavior of SOC dynamics. It is found that in an SOC system, the waiting time of small bursts which are not correlated follows a Poisson distribution ($\mathrm{PDF}(\Delta t) \propto e^{-\alpha\Delta t}$), while that of large bursts which are strongly correlated obeys a power-law distribution ($\mathrm{PDF}(\Delta t) \propto \Delta t^{\alpha}$) [10, 126, 127]. To distinguish the intermittent bursts of different strength in this experiment, the different thresholds are set as $\phi_{th} = 1.0 \times \mathrm{RMS}$ for small events and $\phi_{th} = 1.5 \times \mathrm{RMS}$ for large ones. Because of the short sampling duration and limited data, the data of channels inside $r = 4$ cm (where positive phase bursts are dominant as shown in Fig. 4.10) are selected together for statistical analysis, and the results are given in Fig. 4.16. In both cases the PDFs have a wide distribution, indicating the intermittent bursts are not periodical. It is noted that for small bursts, the distribution of waiting time fits an exponential function well, while the PDF shows a power-law decay for large events at large waiting time ($\Delta t > 0.4$ ms), which gives more evidence on SOC behavior [10, 126, 127].

It is noted that the perturbation at far peripheral region also has a long radial correlation with the localized quasi-coherent fluctuation at the fluctuation frequency (Fig. 4.11). This suggests that the quasi-coherent fluctuation may also contribute to the long radial scale intermittency propagation. Therefore, the correlation between the fluctuation and intermittency generation is worth investigation.

4.3 Ambient turbulence behaviors and nonlinear coupling

For intermittent events, another important property is the interplay between large- and small-scale fluctuations. Behaviors of the ambient turbulence are thus studied in this subsection.

4.3.1 Turbulence envelope behaviors

To obtain the turbulence, a Bessel filter with bandpass frequency from 20 kHz to 50 kHz is applied to the phase difference perturbation $\tilde{\phi}$. Here the frequency range of the turbulence is determined based on the range where the power spectrum is scaled as f^{-2} (Fig. 4.3), i.e. the micro-turbulence range. Besides, after testing several different ranges between 20 kHz and 100 kHz, we found that the turbulent behaviors are almost the same. The PSDs of $\tilde{\phi}$ without and with filtering are shown in Fig. 4.17. The spatial and temporal scales of turbulence are considered to be smaller and shorter than those of quasi-coherent fluctuation. The envelope of this micro-turbulence is calculated with Hilbert transform as shown in Fig. 4.18, where the blue line is original signal and the red line is the envelop of turbulence.

The power spectra and coherence of envelopes of ambient turbulence at $r = 3.83\ \mathrm{cm}$ and $r = 4.09\ \mathrm{cm}$ are given in Figs. 4.19(a) and 4.19(b), respectively. It is clear that even though the spectra are relatively weak, the cross-coherence of the turbulence envelope is significant at the frequency corresponding to the quasi-coherent fluctuation ($f{\sim}11\ \mathrm{kHz}$), which suggests that the ambient turbulence closely correlates to the quasi-coherent fluctuation and the radial nonlinear coupling with the quasi-coherent fluctuation is thus worth investigating. Correlation with low frequency waves ($f \sim 4$ kHz) are also suggested but the low frequency modes seem not to have long radial correlation as discussed later.

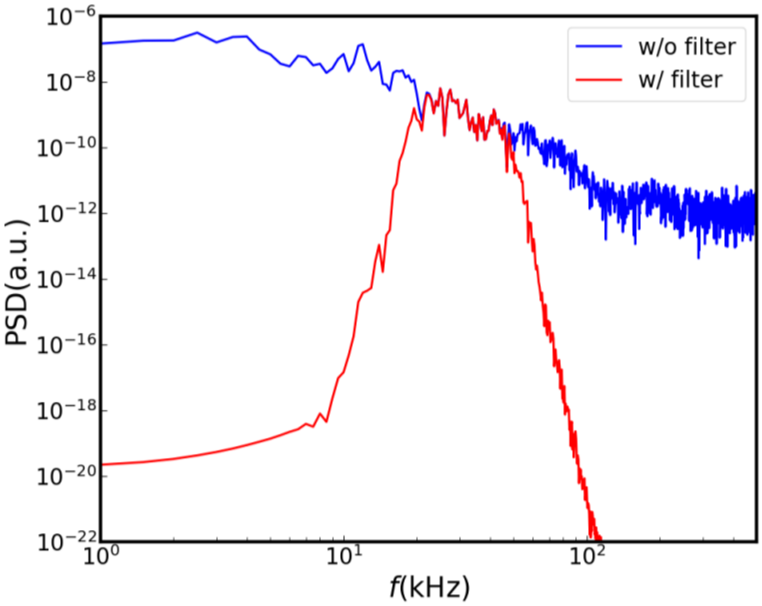

Figure 4.17: PSD of $\tilde{\phi}$ with and without filtering.

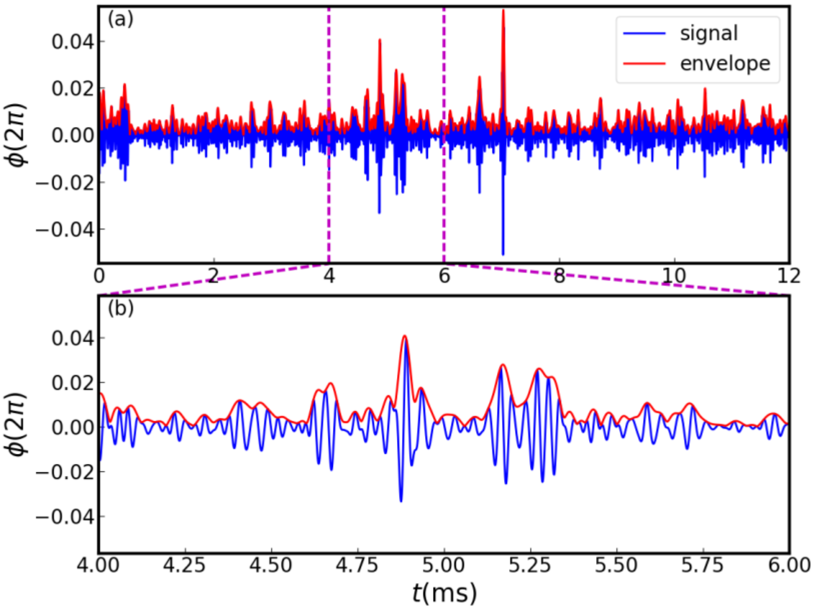

Figure 4.18: (a) Phase difference fluctuation and its envelope and (b) the magnified figure.

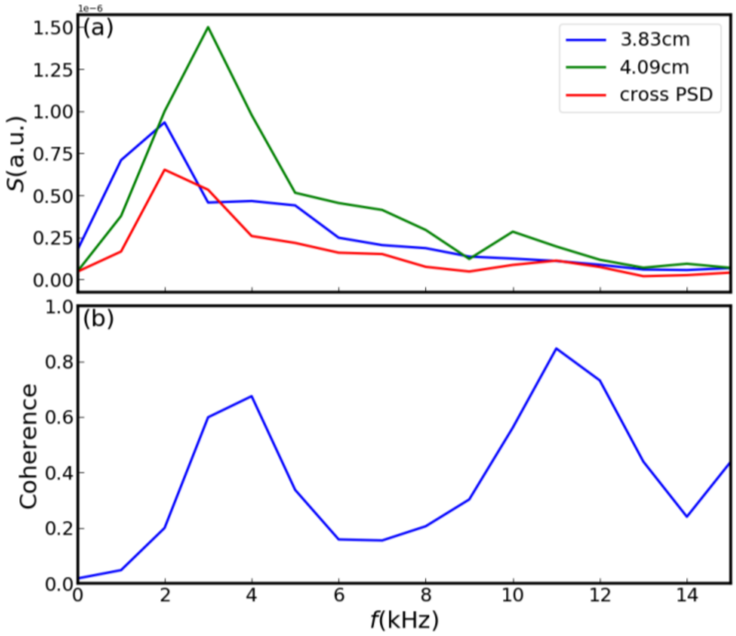

Figure 4.20: (a) auto- and cross-power spectrum density of turbulence envelope. (b) Radial coherence of turbulence envelope

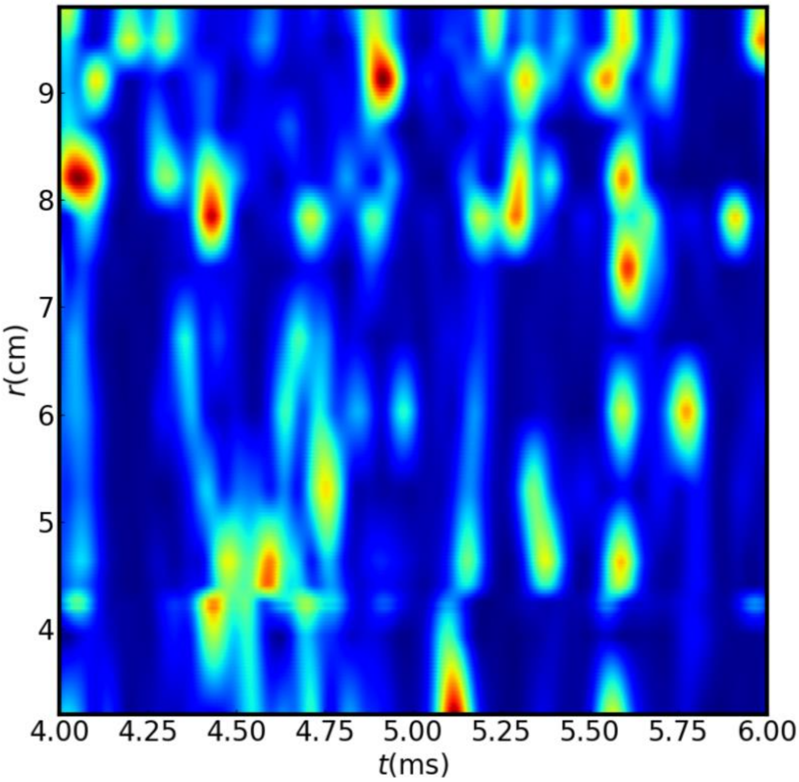

Figure 4.20: Spatial-temporal evolution of turbulence envelope.

It is also noted that the turbulence envelope has the avalanche-like behavior as well. Given in Fig. 4.20 is the spatial-temporal evolution of turbulence envelope and the intermittent inward and outward propagation of the envelope can be clearly observed. This phenomenon is similar with avalanche transport and is associated with the SOC dynamics. However, the scale of turbulence envelope propagation is much smaller than the intermittency phenomenon, which indicates that another mechanism exists for the long radial propagation of intermittent bursts.

4.3.2 Nonlinear three-wave coupling between quasi-coherent fluctuation and turbulence

Fig. 4.21 reveals that the ambient is correlated with the quasi-coherent fluctuation and thus may contribute to the intermittency. To reveal the relationship between ambient turbulence and intermittency, the two-point cross-bicoherence, which is an index of multi-scale coupling at different radii, are calculated. $\phi(t,r_1)$ and $\phi(t,r_2)$ are used as $x_1(t)$ and $x_2(t)$ in Eqs. (3.13) – (3.15) to calculate the cross-bicoherences. We calculate two-point cross-bicoherences in the inner region ($r_1 = 3.23$ cm and $r_2 = 3.83$ cm), in the outer region ($r_1 = 4.83$ cm and $r_2 = 5.32$ cm) and across the inversion layer ($r_1 = 3.23$ cm $r_2 = 5.32$ cm) and the results are shown in Figs. 4.21(a) – 4.21(c). The corresponding summed two-point cross-bicoherences are shown in Figs. 4.21(d) – 4.21(f), respectively. In the inner region, strong nonlinear three-wave coupling between ambient turbulence (20–50 kHz) and the quasi-fluctuation ($f_1 + f_2 = f \sim 11$ kHz) is visible. This means that the ambient turbulence is modulated by the quasi-coherent fluctuation. Although turbulence modulation at lower frequency is suggested in Fig. 4.19 and summed two-point cross bicoherence is significant in the low frequency range, there is no clear peak in the low frequency range as shown in Fig. 4.21(d). The turbulence modulation is also observed in the outer region. The summed two-point cross-bicoherence at $f = 11$ kHz is larger than that observed in the inner region. A small but clear peak is present in Fig. 4.21(c). This indicates nonlinear coupling between ambient turbulence and the quasi-coherent fluctuation across the phase inversion layer exists.

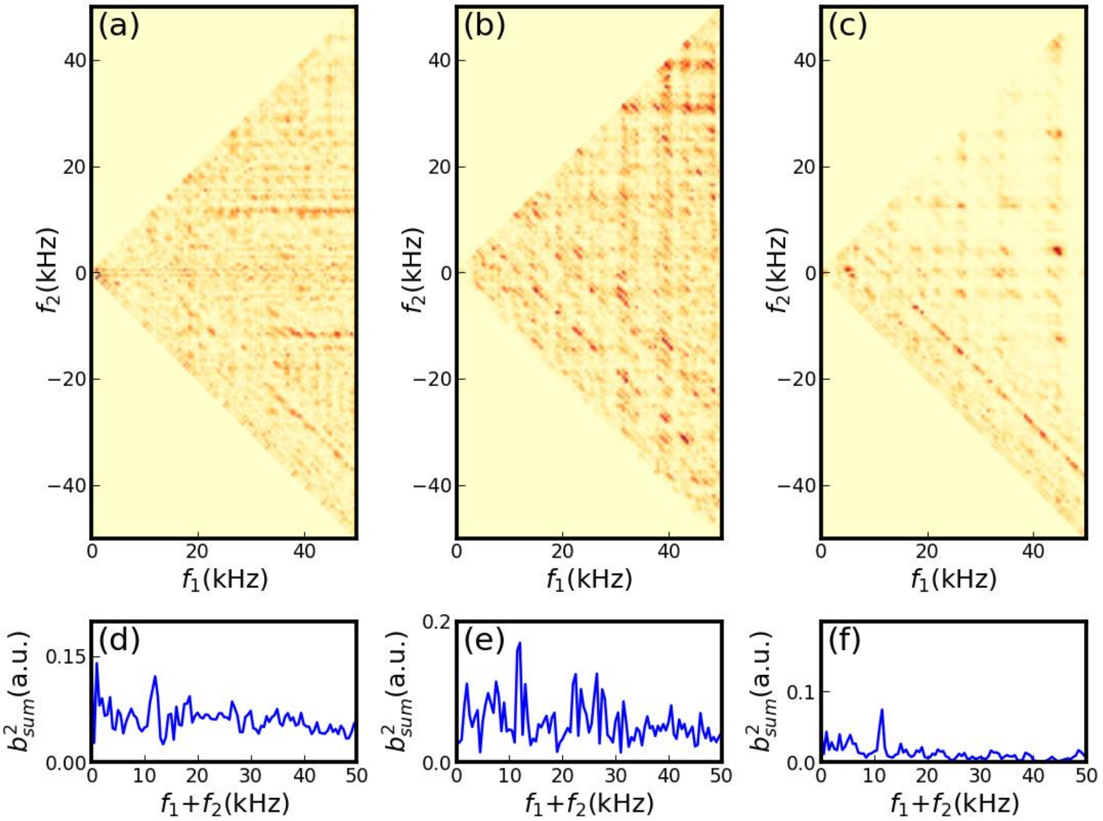

Figure 4.21: Two-point cross-bicoherence of phase fluctuation at (a) $r_1 = 3.23$ cm and $r_2 = 3.83$ cm, (b) $r_1 = 4.83$ cm and $r_2 = 5.32$ cm, (c) $r_1 = 3.23$ cm $r_2 = 5.32$ cm. (d), (e) and (f) are corresponding summed cross-bicoherences.

4.3.3 Discussion

As we can see in Fig. 4.21, the nonlinear three-wave couplings between the ambient turbulence and quasi-coherent fluctuation exist not only across the inversion layer but also at outer region. This indicates that the quasi-coherent fluctuation has a long-radial effect to the ambient turbulence even though itself is localized. The ambient turbulence, which is far away from the fluctuation region, is coupled with the fluctuation and modulated as well. Therefore, after the intermittent density bursts are generated and propagate radially due to the SOC dynamics, the modulated turbulence enhances the density burst and continue the radial propagation. The radial scale of the propagation of density burst is thus elongated and the intermittency is finally generated.

4.4 Conclusion

In short summary, this chapter introduces the setup of intermittency experiment with microwave reflectometers in PANTA in the high heating power case ($P = 6$ kW), and the global intermittency phenomenon along with a localized high-frequency (~ 10 kHz) quasi-coherent fluctuation are observed. By studying the characteristics of the fluctuation and intermittent bursts, the generation mechanism of the intermittency is revealed as follows.

At high heating power case, a large density gradient is formed at

$r \sim 4$ cm, which excites a high-frequency quasi-coherent fluctuation. The fluctuation is localized ($r = 3 - 4.5$ cm) and modulates the local density. The positive and negative density perturbations are separated on different sides of $r = 4$ cm and propagate at opposite direction due to the SOC dynamics. Because of the radially long-scale nonlinear three-wave coupling between the fluctuation and the turbulence, the modulated turbulence enhances the density burst and continue the radial propagation. The global intermittency phenomenon is thus formed.

The high frequency quasi-coherent fluctuation is crucial during the generation of intermittency, and its identification is thus important. However, what the quasi-coherent fluctuation is remains to be a question by now. Identification and discussion of the quasi-coherent fluctuation is left for future work, and reflectometry in conjunction with multi-probe systems will give as more details of spatial structure of the quasi-coherent mode.

The avalanche-like transport of turbulence envelope is observed and worth studying as well. In order to identify the avalanche transport, simultaneous measurement of temporal evolution of density gradient is required. Fast reconstruction of density profile by using the microwave frequency comb reflectometer is one of promising methods, but requires higher accuracy. Such fast reconstruction is now under developing.

Chapter 5

Summary

The turbulence intermittency is a key issue in magnetically confined plasma study, which has a significant influence on non-diffusive transport, plasma confinement and material interaction. Thus, a good understanding of its properties and mechanism is crucial. For this purpose, this thesis focuses on the experimental intermittency studies in linear device PANTA, and advanced microwave reflectometers are developed. The summary of this thesis is as follows:

(i) High-resolution microwave reflectometers are developed

As a diagnostic technique introducing no disturbance to the plasma, microwave reflectometer is now widely used as a support for fusion plasma research. In this thesis, firstly the basic theory of microwave propagation in plasma is described. Then the frequency comb microwave reflectometer and comb sweep microwave reflectometer in PANTA are demonstrated. The comb microwave reflectometer covers a frequency range from 12 to 26 GHz with 29 channels. The extraction method of the phase difference of reflected and incident waves is introduced. With template conditional averaging method, the error of phase difference is reduced. The density profile is thus reconstructed and density perturbation is obtained with the phase difference. Besides, the comb sweep microwave reflectometer is developed for density profile reconstruction, eliminating the half-wavelength uncertainty measured with the comb reflectometer. The comb sweep reflectometer has 17 channels, covering frequency range from 15.5 to 24 GHz. Each channel sweeps a range of 0.4 GHz with a time resolution of 2 μs. The density profile reconstruction method with the system is described and density profile is obtained. The system is proved to be feasible and reliable. The density profile measured with comb reflectometer is modified based on that from comb sweep reflectometer. The density profile reconstructed with different diagnostics agree well with each other.

(ii) Spatial-temporal evolution and statistical characteristics of intermittent features are studied

Turbulence intermittency experiment is performed in PANTA, and global intermittent features is observed with the microwave reflectometers. It is found that at radius $r = 3 - 4.5\ \mathrm{cm}$, where the electron density gradient is largest, a quasi-coherent fluctuation with a frequency of 11 kHz is located. Besides, the global intermittent density burst is observed as well. Statistical analysis is thus performed. Firstly, conditional averaging results show density bump and hole exist in the outer and inner regions, respectively. The outward propagation velocity of the density bump reaches approximately 1.0 km/s. Then, the probability density function shows a deviation of the density perturbation from Gaussian-distribution.

The positive and negative density bursts are dominant in the peripheral and core regions, respectively. The inversion layer is located at around $r = 4$ cm. Besides, the density perturbation around inversion layer shows long-range time correlation, and the waiting time for large density bursts follow power-law distribution, indicating the existence of SOC dynamics. The density perturbation shows a large-radial-scale correlation. The cross-bicoherences indicate the existence of nonlinear three-wave coupling between the localized quasi-coherent fluctuation and the far turbulence.

(iii) Generation mechanism of intermittency is revealed

The generation mechanism of the intermittency is revealed. The location of the quasi-coherent fluctuation is highly coincident with the large density gradient region, indicating it is excited by the gradient. The inversion layer of density bumps and holes is located inside the fluctuation region, suggesting the positive and negative density perturbations are separated. The self-similarity and the long-range correlation inside the fluctuation region indicate the existence of SOC dynamics, which induces the initial meso-scale propagation of density bursts. Because of the nonlinear three-wave coupling, the far turbulence is modulated by the quasi-coherent fluctuation and enhances the density burst propagating from fluctuation region. The meso-scale propagation is thus elongated and the global intermittency is generated.

Even though the statistical characteristics and generation mechanism of the intermittency are preliminarily studied, still many questions remain unknown. The first question is what the high-frequency quasi-coherent fluctuation is. It seems to be excited by the large density gradient and has a large inward wavenumber, but its identification is necessary. Besides, the avalanche-like property of the turbulence envelope is also worth studying, which requires the fast reconstruction of density profile with higher accuracy. Thus, a more stable and accurate comb sweep microwave reflectometer needs to be developed. These works remain to be done in the future.

Acknowledgement

As my 3 years Ph. D study is almost finished, I feel really different from the moment when I just entered Kyushu University. I have learned and changed so much during the part 3 years, which will benefit me all my life. At the end of my thesis, I wish to thank all those who guided me, helped me and inspired me during my doctoral study.

First of all, I am deeply thankful to my supervisor, Professor Shigeru Inagaki. During my doctoral study, he continued to give me help and guidance whenever I needed. He helped me not only to conduct experiments but also to revise papers. He also encouraged me to attend conferences to shear my results. I am deeply influenced by his professional perspective, profound knowledge and careful attitude in science research. It is impossible for me to finish my doctor course without him.

Secondly, I wish to express my thanks to Associated Professor Y. Kosuga and Assistant Professor M. Sasaki, who gave me lots of useful advices during my research. I also wish to appreciate Professor P. H. Diamond who helped me finish the small project during the 9th Festival de Théorie 2017. I would like to express my appreciation to my lab members, especially for Dr. F. Kin, Dr. K. Yamasaki, Mr. K. Hasamada, Mr. Y. Kawachi and Mr. Y. Iwasaki, for their friendly help on my experiments. I have enjoyed the campus life with them.

I also would like to appreciate my parents and my sister. They always stand behind me and give me both financial and spiritual support when I met difficulties.

Finally, I would like to express my special gratefulness to my lovely fiancee, who stays with me all the time. Whenever I feel depressed during my research she always comforts me, making me energetic again. I would never insist on my research without her encouragement.

Bibliography

[1] Hüseyin Gökçekus, Umut Türker and James W. LaMoreaux, *Survival and Sustainability: Environmental concerns in the 21st Century*, Springer, 2011.

[2] https://www.iter.org/sci/Fusion

[3] Heinz Knoepfel, *Energy 2000: An Overview of the World's Energy Resources in the Decades to Come*, Routledge, 2018.

[4] J. Wesson, *Tokamak*s, Oxford University Press, 1997.

[5] J. D. Lawson, *Pro. Phys. Soc. B* **70**, 6 (1957).

[6] M. Shimada, et al., *Nucl. Fusion* **47**, S1 (2007).

[7] https://en.wikipedia.org/wiki/ITER

[8] D. H. J. Goodall, *J. Nucl. Mater.* **111**, 11 (1982).

[9] S. J. Zweben, *Phys. Fluids* **28**, 974 (1985).

[10] Y. H. Xu, et al., *Plasma Phys. Control. Fusion* **47**, 1841 (2005).

[11] S. I. Krasheninnikov, et al., *J. Plasma Phys.* **74**, 679 (2008).

[12] D. A. D'Ippolito, et al., *Phys. Plasma* **18**, 060501 (2011).

[13] S. I. Krasheninnikov and A. I. Smolyakov, *Phys. Plasmas* **10**, 3020 (2003).

[14] P. A. Politzer, et al., *Phys. Plasmas* **9**, 1962 (2002).

[15] J. A. Boedo, et al., *Phys. Plasma* **10**, 1670 (2003).

[16] B. Nold, et al., *Plasma Phys. Control. Fusion* **52**, 065005 (2010).

[17] G. Y. Antar, et al., *Phys. Plasmas* **8**, 1612 (2001).

[18] B. Goncalves, et al., *J. Nucl. Mater.* **337**, 376 (2005).

[19] G. S. Xu, et al., *Nucl. Fusion* **49**, 092002 (2009).

[20] N. Asakura, et al., *J. Nucl. Mater.* **390**, 364 (2009).

[21] H. Tanaka, et al., *Nucl. Fusion* **49**, 065017 (2009).

[22] J. Cheng, et al., *Plasma Phys. Control. Fusion* **52**, 055003 (2010).

[23] O. E. Garcia, et al., *Nucl. Mater. Energy* **12**, 36 (2017).

[24] J. L. Terry, et al., *Phys. Plasmas* **10**, 1739 (2003).

[25] R. Jha, et al., *Phys. Rev. Lett.* **69**, 1375 (1992).

[26] O. Grulke, et al., *Phys. Plasma* **8**, 5171 (2001).

[27] N. Ohno, et al., *Contrib. Plasma Phys.* **46**, 692 (2006).

[28] T. Happel, et al., *Phys. Rev. Lett.* **102**, 255001 (2009).

[29] G. Y. Antar, et al., *Phys. Rev. Lett.* **87**, 065001 (2001).

[30] T. A. Carter, et al., *Phys. Plasma* **13**, 010701 (2006).

[31] V. Carbone, et al., *Phys. Plasma* **7**, 445 (2000).

[32] A. Fredriksen, et al., *Plasma Phys. Control. Fusion* **45**, 721 (2003).

[33] I. Furno, et al., *Phys. Rev. Lett.* **100**, 055004 (2008).

[34] L. F. Burlaga, *J. Geophys. Res.* **96**, 5847 (1991).

[35] V. Angelopoulos, et al., *J. Geophys. Res.* **101**, 4967 (1996).

[36] M. V. Umansky, et al., *Phys. Plasma* **5**, 3373 (1998).

[37] B. LaBombard, et al., *Nucl. Fusion* **40**, 2041 (2000).

[38] B. LaBombard, et al., *Phys. Plasma* **8**, 2107 (2001).

[39] H. Maier, et al., *J. Nucl. Mater.* **266**, 1003 (1999).

[40] D. L. Rudakov, et al., *Nucl. Fusion* **45**, 1589 (2005).

[41] R. A. Pitts, et al., *Nucl. Fusion* **46**, 82 (2006).

[42] M. Greenwald, *Plasma Phys. Control. Fusion* **44**, R27 (2002).

[43] T. Happel, et al., *Nucl. Fusion* **56**, 064004 (2016).

[44] P. A. Politzer, *Phys. Rev. Lett.* **84**, 1192 (2000).

[45] P. Bak, et al., *Phys. Rev. Lett.* **59**, 381 (1987).

[46] T. Hwa and M. Kardar, *Phys. Rev. A* **45** 7002 (1992).

[47] P. H. Diamond and T. S. Hahm, *Phys. Plasmas* **2**, 3640 (1995).

[48] B. A. Carreras, et al., *Phys. Plasma* **3**, 2903 (1996).

[49] X. Garbet and R. E. Walts, *Phys. Plasma* **5**, 2836 (1998).

[50] Y. Sarazin and P. Ghendrih, *Phys. Plasma* **4**, 4214 (1998).

[51] A. Hasegawa and M. Wakatani, *Phys. Rev. Lett.* **50**, 682 (1983).

[52] S. Inagaki, et al., *Sci. Rep.* **6**, 22189 (2016).

[53] N. Dupertuis, et al., *Plasma Fusion Res.* **12**, 1201008 (2017).

[54] S. Oldenburger, et al., *Plasma Phys. Control. Fusion* **54**, 055002 (2012).

[55] T. Kobayashi, et al., *Phys. Plasmas* **22**, 112301 (2015).

[56] T. Kobayashi, et al., *Plasma Fusion Res.* **6**, 2401082 (2011).

[57] K. Hasamada, et al., *Plasma Fusion Res.* **12**, 1201034 (2017).

[58] K. Hasamada, *Multi Time Scale Fluctuation in PANTA*, Master thesis, Kyushu University, Japan, 2017.

[59] K. Miyamoto, *Plasma Physics and Controlled Nuclear Fusion*. Springer, 2006.

[60] A. C. C. Sips, *Reflectometry and Transport in Thermonuclear Plasmas in the Joint European Torus*, Ph.D. thesis, Eindhoven University of Technology, Netherlands, 1991.

[61] J. Sanchez, et al., Broadband Heterodyne Reflectometry: Application to the W7-AS stellarator, *Proc. 1st International Reflectometry Workshop*, Abingdon, United Kingdom, 1992.

[62] E. Mazzucato and R. Nazikian, *Phys. Rev. Lett.* **71**, 1840 (1993).

[63] M. Hirsch, et al., Doppler Reflectometry for the Investigation of poloidally propagating Density Perturbations, *Proc. 4th International Reflectometry Workshop*, Cadarache, France, 1999, report EUR-CEA-FC-1674.

[64] X. L. Zou, et al., Poloidal Rotation Measurement in Tore Supra by Oblique Reflectometry, *Proc. 4th International ReflectometryWorkshop*, Cadarache, France, 1999, report EUR-CEA-FC-1674.

[65] W. A. Peebles, et al., *Rev. Sci. Instrum.* **81**, 10D902 (2010).

[66] T. Tokuzawa, et al., *Plasma Fusion Res.* **9**, 1402149 (2014).

[67] Z. B. Shi, et al., *Rev. Sci. Instum.* **87**, 113501 (2016).

[68] W. L. Zhong, et al., *Nucl. Fusion* **55**, 113005 (2015).

[69] Z. B. Shi, et al., *Rev. Sci. Instum.* **89**, 10H104 (2018).

[70] G. D. Conway, et al., *Plasma Phys. Control. Fusion* **46**, 951 (2004).

[71] P. Hennequin, et al., *Rev. Sci. Instum.* **75**, 3881 (2004).

[72] J. C. Hillesheim, et al., *Rev. Sci. Instum.* **80**, 083507 (2009).

[73] T. Happel, et al., *Rev. Sci. Instum.* **80**, 073502 (2009).

[74] T. Happel, *Doppler Reflectometry in the TJ-II Stellarator: Design of an Optimized Doppler Reflectometer and its Application to Turbulence and Radial Electric Field Studies*, Ph. D. thesis, Universidad Carlos III de Madrid, Spain, 2010.

[75] C. Laviron, et al., *Plasma Phys. Control. Fusion* **38**, 905 (1996).

[76] E. Mazzucato, *Rev. Sci. Instrum.* **69**, 2201 (1998).

[77] L. Cupido, et al., *Plasma Phys. Control. Fusion* **39**, 249 (1997).

[78] A. C. C. Sips and G. J. Kramer, *Plasma Phys. Control. Fusion* **35**, 743 (1993).

[79] S. Hacquin, et al., *Nucl. Fusion* **46**, S714 (2006).

[80] S. Inagaki et al., *Plasma Fusion Res.* **8**, 1201171 (2013).

[81] T. Mizokami, *Development of a Microwave Frequency Comb Reflectometer in PANTA*, Master thesis, Kyushu University, Japan, 2016.

[82] X. L. Zou, et al., *Plasma Phys. Control. Fusion* **33**, 903 (1991).

[83] E. Mazzucato, *Rev. Sci. Instrum.* **69**, 2201 (1998).

[84] W. L. Zhong, *Study on Plasma Turbulence and Transport with Advanced Microwave Diagnosis in Tokamak*, Ph.D. thesis, Southwestern Institute of Physics, China, 2016.

[85] K. W. Kim, et al., *Rev. Sci. Instrum.* **68**, 466 (1997).

[86] G. Wang, et al., *Rev. Sci. Instrum.* **75**, 3800 (2004).

[87] F. Clairet, et al., *Rev. Sci. Instrum.* **72**, 340 (2001).

[88] F. Clairet, et al., *Rev. Sci. Instrum.* **74**, 1481 (2003).

[89] F. Clairet, et al., *Rev. Sci. Instrum.* **81**, 10D903 (2010).

[90] L. Meneses, et al., *Rev. Sci. Instrum.* **77**, 10E927 (2006).

[91] A. Sirinelli, et al., *Rev. Sci. Instrum.* **81**, 10D939 (2010).

[92] P. Varela, et al., *Rev. Sci. Instrum.* **72**, 315 (2001).

[93] F. Clairet, et al., *Rev. Sci. Instrum.* **88**, 113506 (2017).

[94] W. L. Zhong, et al., *Rev. Sci. Instrum.* **82**, 103508 (2011).

[95] S. B. Zhang, et al., *Plasma Sci. Technol.* **16**, 311 (2014).

[96] L. H. Wan, et al., *Plasma Sci. Technol.* **19**, 025602 (2017).

[97] S. H. Seo, *Rev. Sci. Instrum.* **89**, 10H121 (2018).

[98] J. Santos, et al., *Rev. Sci. Instrum.* **74**, 1489 (2003).

[99] J. Santos, et al., *Nucl. Fusion* **52**, 032003 (2012).

[100] B. Y. Zhang, et al., *Plasma Fusion Res.* **14,** 1201131 (2019).

[101] F. Kin, *Experimental Study on Structure Formation of Plasma Turbulence*, Ph.D. thesis, Kyushu University, Japan, 2019.

[102] J. W. Cooley and J. W. Tukey, *Math. Comput.* **19**, 297 (1965).

[103] A. Fujisawa, et al., *Plasma Phys. Control. Fusion* **49**, 211 (2007).

[104] Y. Nagashima, et al., *Phys. Rev. Lett.* **95**, 095002 (2005).

[105] Y. C. Kim and E. J. Powers, *IEEE Trans. Plasma Sci.* **7**, 120 (1979).

[106] K. J. Zhao, et al., *Phys. Plasma* **14**, 122301 (2007).

[107] H. E. Hurst, *Trans. Amer. Soc. Civil Eng.* **116**, 770 (1951).

[108] B. B. Mandelbrot and J. R. Wallis, *Water Resour. Res.* **4**, 909 (1968).

[109] B. B. Mandelbrot and J. R. Wallis, *Water Resour. Res.* **5**, 967 (1969).

[110] B. A. Carreras, et al., *Phys. Rev. Lett.* **80**, 4438 (1998).

[111] B. A. Carreras, et al., *Phys. Plasma* **5**, 3632 (1998).

[112] W. H. Wang, *Study on Edge Plasma Turbulence Long-Range Correlation Characteristics and Poloidal Flow Driven by Turbulent Reynolds Stress*, Ph.D. thesis, University of Science and Technology of China, China, 2002.

[113] C. X. Yu, et al., *Phys. Plasma* **10**, 2772 (2003).

[114] Y. H. Xu, et al., *Phys. Plasma* **11**, 5413 (2004).

[115] H. W. Muller, et al., *Nucl. Fusion* **51**, 073023 (2011).

[116] G. Birkenmeier, et al., *Plasma Phys. Control. Fusion* **56**, 075019 (2014).

[117] G.M. Friesen, et al., *IEEE Trans. Biomed. Eng.* **37**, 85 (1990).

[118] S. Inagaki, et al., *Plasma Fusion Res.* **9**, 1201016 (2014).

[119] Kawachi et al., Observation of quasi-periodic coherent mode with intermittent fluctuation in cylindrical magnetized plasma, *8th Asia-Pacific Transport Working Group*, Leshan, China, 2018, poster A-P10.

[120] Y. Kawachi, et al., *Plasma Fusion Res.* **13**, 3401105 (2018).

[121] B. A. Carreras, et al., *Phys. Plasmas* **6**, 4615 (1999).

[122] N. Gache, et al., Fractal dimension estimators for fractional Brownian motions, *IEEE International Conference on Acoustics, Speech, and Signal Processing (ICASSP-91)*, Toronto, Canada, 1991.

[123] J. M. Beall, et al., *J. Appl. Phys.* **53**, 3933 (1982).

[124] X. Garbet, et al., *Nucl. Fusion* **34**, 963 (1994).

[125] P. Beyer, et al., *Phys. Rev. Lett.* **85**, 4892 (2000).

[126] R. Sanchez, et al., *Phys. Rev. Lett.* **88**, 068302 (2002).

[127] R. Sanchez, et al., *Phys. Rev. Lett.* **90**, 185005 (2003).

Appendix

Experimental Study of Perturbative Particle Transport in the HL-2A Tokamak

For realization of magnetic fusion reactor, achievement of dense core plasma is necessary [A1]. Particle transport in tokamaks and helical devices is however unresolved mystery for over 30 years. It was found to be difficult to explain radial density profile by diffusive transport models [A2, A3]. A turbulent pinch is proposed to explain the profile peeking without central fueling [A4]. Experimental observations indicate the connection between density peaking and turbulent state, which is predicted by turbulent transport theory [A5]. Although the pinch model is consistent with experimental trends, there still are many questions remaining unsolved which may arise from lack of understanding of turbulence. Recently, perturbative method has been proved to be one of the most effective ways to study particle transport in plasma. Particle transport coefficients, i.e. diffusivity and convection velocity are determined [A6-A8], and some progress on transport barriers and transport mechanism have been achieved [A9-A11]. To confirm the non-diffusive nature of particle transport associated with the turbulent pinch, perturbative particle transport experiment has been performed in the HL-2A tokamak with supersonic molecular beam injection (SMBI), and microwave reflectometers [A12] are used as the main diagnostic system to study particle transport.

Perturbative particle transport experiment has been performed in the HL-2A tokamak [A13]. The parameters in this experiment are as follows: major radius $R = 1.65\mathrm{m}$, minor radius $a = 0.4$ m, magnetic field $B_0 = 1.35\ \mathrm{T}$, plasma current $I_p = 170\ \mathrm{kA}$, and background electron density $n_e = 1.4 \times 10^{19}\ \mathrm{m}^{-3}$. Figure A.1 shows the temporal evolution of plasma parameters of a typical discharge, where the electron temperature is measured with an electron cyclotron emission (ECE) radiometer [A14] and the line-average density is measured with a far infrared rays (FIR) laser interferometer [A15]. Plasma current is kept stable from 200 ms to 1700 ms. Neutral Beam (400 kW, co-) is injected at 500 ms, during which the stored energy is obviously increased. The supersonic molecular beam injection (SMBI), which has advantages of deep penetration and high fueling efficiency [A16], is used as perturbative particle source. Electron density is modulated by periodical SMBI (repetition period of 60 ms and pulse width of 2 ms) from 500 ms to 1000 ms as shown in Fig. A.1.

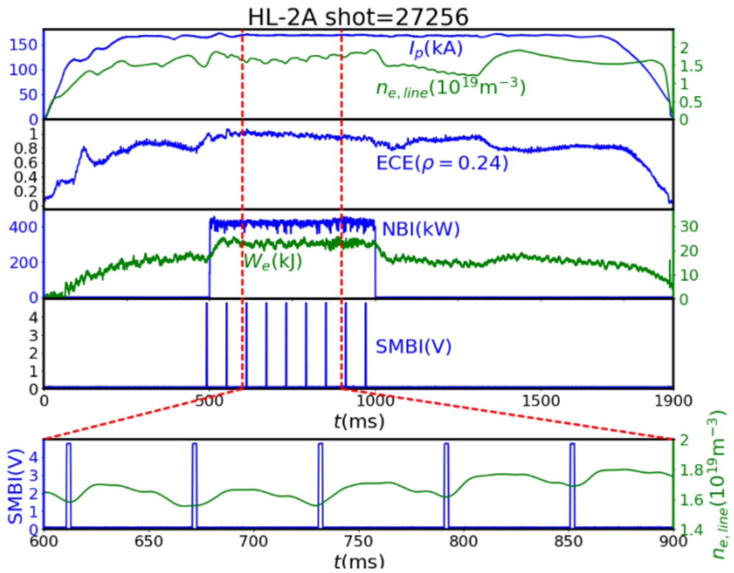

Figure A.1: Typical parameters of perturbative particle transport experiment.

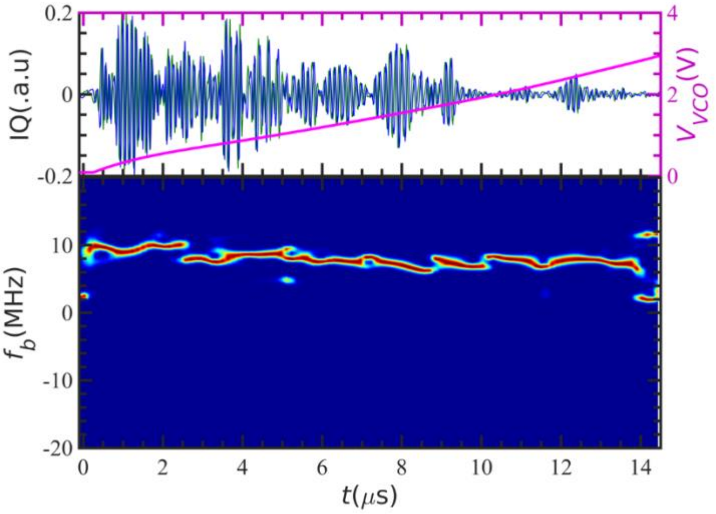

Figure A.2: IQ signals and beat frequency of reflected wave of microwave reflectometer.

A sweeping frequency microwave reflectometer with high temporal resolution (up to 6 μs for a frequency sweep) is used to measure the density profile and trace perturbation [A17]. A dynamic calibration method of voltage controlled oscillator (VCO) is developed and dispersion of the transmission system is taken into account to reduce measurement error [A17]. Figure A.2 shows a temporal evolution of beat frequency extracted from the spectrogram in a sweeping period. The beat frequency keeps mostly stable except for some frequency jump points and thus phase delay is obtained according to this. The phase losses at frequency jump points are modified with numerical method [A18].

Radial profiles and temporal evolution of electron density are reconstructed, which are shown in Figs. A.3(a) and A.3(b). It is clear that the edge density rapidly responses to SMBI fueling and is strongly modulated. Density perturbation after SMBI is $dn_e = n_e(t_0 + dt) - n_e(t_0)$, where t_0 is starting time of SMBI injection and dt is time delay after SMBI injection. The particle source can be estimated by dn_e while dt is short enough, which means the particle transport is negligible. The line-average density measured by FIR at $\rho = 0.1$ is shown as the green line in Fig. A.3(a), where $\rho = r/a$ is the normalized radius. Figure A.3(c) illustrates the radial profile of particle source at 8 ms after SMBI injection (a reason for the choice of 8 ms is explained later). The particle source locates at $\rho = 0.81$ and can be fitted by a Gaussian distribution function.

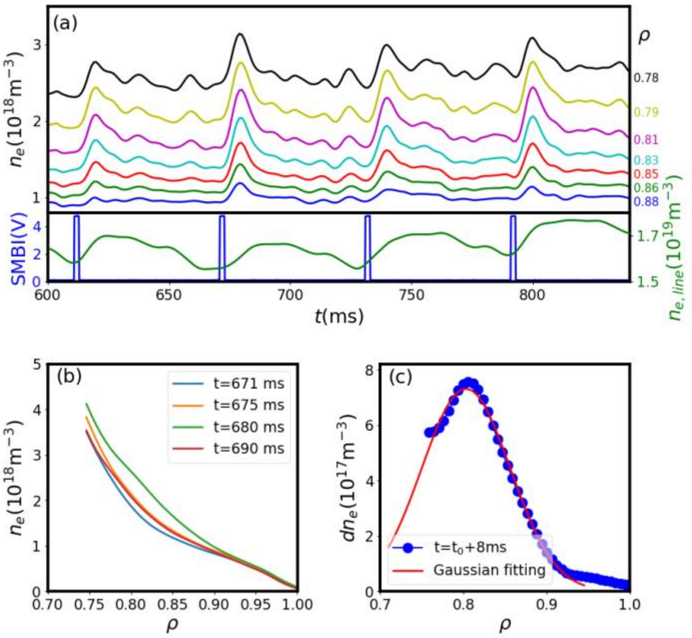

Figure A.3: Temporal evolution of local electron density (a) and radial profile (b), and estimated particle source (c).

Evaluation of transport parameters (e.g. diffusivity and pinch velocity) from amplitudes and phase delays of perturbations, which are given by the FFT analysis, is one of the well-known methods for perturbative particle transport study [A19]. This model presumes diffusive-like flux-gradient relation, however it is not confirmed yet. The flux-gradient relationship should be thus directly analyzed to confirm whether flux is proportional to gradient and whether turbulent pinch exists.

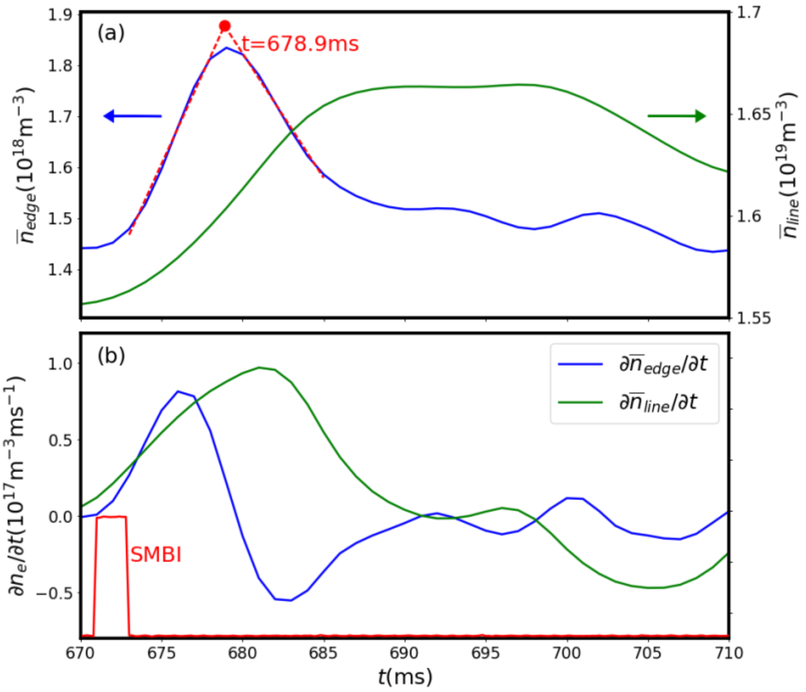

Figure A.4: (a) Temporal evolution and (b) temporal derivative of edge density and line-average density after SMBI injection.

Particle source has a direct influence on spatiotemporal behaviors of electron density perturbation, then spatiotemporal region of source should be distinguished from source-free region. Figure A.4 displays the temporal evolution and temporal derivative of edge density ($\rho > 0.75$) and line-average density after SMBI injection at 671 ms, where edge density is defined as averaged profile of edge density measure with reflectometer. It shows that just after the SMBI injection, edge density rapidly increases from $1.45 \times 10^{18}\ \mathrm{m}^{-3}$ to $1.82 \times 10^{18}\ \mathrm{m}^{-3}$ in 8 ms, and reaches a maximum at 679 ms. Meanwhile, line-average density increases slowly. A linear fitting of edge density evolution also shows the turning point of density growth locates at 678.9 ms, which illustrates that SMBI source is fully ionized and transport is source-free since then. Before 678.9 ms, temporal evolution of density is dominated by particle source.

During source phase, the growth rate of edge density increases rapidly in 5 ms and then returns to zero in 3 ms, but the growth rate of line-average density always keeps increasing slowly and reaches maximum around 682 ms. This phenomenon declares that the particle source induced by SMBI deposits at edge and transports to core, resulting in the rapid growth of edge density and delayed growth of central density during the source phase.

During the source-free phase after 678.9 ms, core and edge regions indicate different transport characteristics. In Fig. A.4 it is shown that while edge density starts to decrease, the core density, which is represented by line-average density, still keeps growing. The growth of core density continues until 685 ms when the growth rate is almost zero. This indicates that there is a strong inward flux from edge to core, which is likely to be inward pinch. During this phase, the density profile should be steepened. From 685 ms to 700 ms, the core density remains almost constant while change in edge density is also small. This suggests that the steep profile stays unchanged due to zero particle flux, i.e. inward flux is balanced by outward flux which may be driven by the enhanced density gradient. After 700 ms, the core density starts to decrease then total flux seems to become outward. During this phase, the inward flux is considered to be suppressed.

The edge density perturbation ($dn_e(t) = n_e(t) - n_e(t_0)$) contours and edge density gradient contours after 671ms are shown in Fig. A.5, where line-average density is shown as the green line. It is clear that edge density evolution experiences three different phases, which is consistent with core transport phases. When the core density still keeps increasing from 679 ms to 685 ms, the edge density decreases rapidly, which again demonstrates that a strong inward particle flux exists in the core region during this phase. Presence of inward flux at the edge is discussed later. It should be noted that during this phase, the density gradient at the edge almost keeps constant, indicating that the inward flux may be driven by pinch. When the core density stops increasing and keeps almost stable from 685 ms to 700 ms, the edge density also slows down decreasing. However, the density gradient gradually decays at this time. The edge density shows some intermittent decays just before decrease in the core density at 700ms.

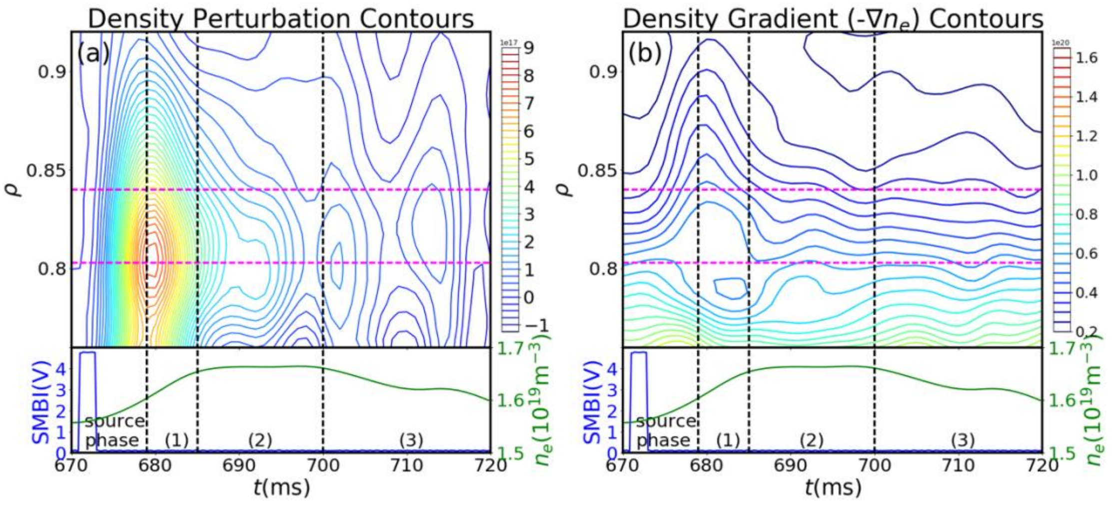

Figure A.5: Contours of density (a) perturbation and (b) gradient.

In order to reveal the transport process better, the flux-gradient relationship is required. The flux perturbation is evaluated from time-depend particle balance equation and written as,

$$-\Gamma = \int_0^r \frac{\partial n_e}{\partial t} dV \qquad (\mathrm{A.1})$$

where particle source perturbation induced by SMBI and change of recycling is separated spatially and temporally. Therefore, particle source perturbation is neglected. Because of the limited waveband, the reflectometer can only cover part of the radial density profile. Thereby, to estimate particle flux, the radial profile is divided into edge part and core part,

$$-\Gamma = \int_0^{r_1} \frac{\partial n_e}{\partial t} dV + \int_{r_1}^{r} \frac{\partial n_e}{\partial t} dV \qquad (\mathrm{A.2})$$

As the density profile and its temporal evolution at core region is unknown, a quadratic-like core density profile is assumed according to the interferometer diagnostic system [A20],

$$n_e(r) = n_e(0)\left[1-\left(\frac{r}{a}\right)^2\right] e^{-(r/a)^2} \qquad (\mathrm{A.3})$$

where $n_e(r)$ is the electron density at radial position r. The core average-density calculated from this model is a function of $n_\mathrm{e}(0)$, while it is obtained experimentally by eliminating contribution of edge density from line-average density, thus the core density profile and flux is obtained.

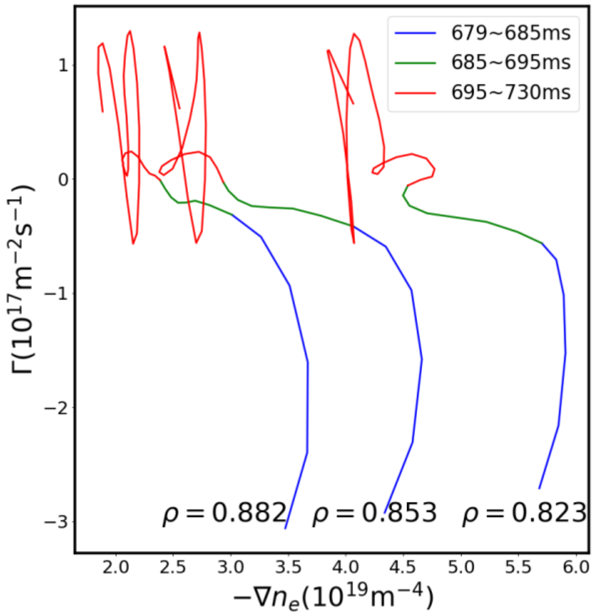

Figure A.6: Flux—gradient dependence at different radial positions.

According to the formula above, the dependence of flux and gradient at different radial positions is given in Fig. A.6, which shows three different processes obviously. Firstly, from 679 ms to 685 ms, the transport is dominated by inward flux, resulting in the decrease of edge density and increase of core density. The inward flux decreases rapidly during this phase while the gradient remains almost unchanged. This indicates that the inward flux is not driven by local density gradient. Instead, it is driven by pinch. From 685 ms to 695 ms, the flux is almost zero. The density gradient is relaxed even though the flux is close to zero, which seems to be diffusive process but negative diffusion ($-\Gamma/\nabla n_{\mathrm{e}} < 0$ and $-\partial\Gamma/\partial\nabla n_{\mathrm{e}} < 0$). After 695 ms intermittent outward flux is dominant, which leads to sudden decrease of both edge and core density.

The first term of the right-hand side of Eq. (A.2) may have errors due to lack of local measurement of core density. However, increment of the core average-density and reduction of edge density during source-free region clearly indicate the presence of inward flux. Therefore, flux-gradient relation shown in Fig. A.6 captures particle transport features of this experiment qualitatively.

Inhomogeneities of magnetic field and temperature are considered to cause turbulent pinch in tokamak [A4]. Magnetic configuration is unchanged in the perturbative experiment and thus observed inward flux is not driven by magnetic field gradient. Concerning temperature gradient, there are no significant changes in the central ECE signal and then temperature gradient perturbation in the core may be negligible small. However, edge temperature is changed by the SMBI. Evaluation of flux-temperature-gradient relation is left in the future work.

Particle transport is studied by perturbative experiment by using SMBI in HL-2A tokamak. Spatiotemporal evolution of edge density perturbation traced with a reflectometer with high temporal and spatial resolution allows us to estimate particle source and flux-gradient relation. This analysis indicates that i) inward particle flux, which doesn't depend local gradient, is driven after the SMBI, ii) weak negative diffusion is suggested at the edge in the stable phase and iii) intermittent process enhances outward flux at the edge. The observed flux-gradient relation is far from diffusive transport picture. An understanding of turbulence-driven flux will have deep impact on our predictability of evolution of density profile, and provide a sophisticated particle control knob of burning plasmas, such as ITER.

[A1] H. Weisen, et al., Nucl. Fusion 45, L1 (2005).

[A2] K. H. Burel, et al., Phys. Fluids B 2, 2904 (1990).

[A3] F. Wagner and U. Stroth, Plasma Phys. Control. Fusion 35, 1321 (1993).

[A4] J. Weiland, A. B. Jarmén and H. Nordman, Nucl. Fusion 29, 1810 (1989).

[A5] C. Angioni1, et al., Plasma Phys. Control. Fusion 51, 124017 (2009).

[A6] K. W. Gentle, O. Gehre and K. Krieger, Nucl. Fusion 32, 217 (1992).

[A7] H. Takenaga, et al., Plasma Phys. Control. Fusion 40, 183 (1998).

[A8] J. P. T. Koponen, et al., Nucl. Fusion 40, 365 (2000).

[A9] W. W. Xiao, et al., Phys. Rev. Lett. 104, 215001 (2010).

[A10] S. Mordijck, et al., Phys. Plasma 19, 056503 (2012).

[A11] W. L. Zhong, et al., Phys. Rev. Lett. 111, 265001 (2013).

[A12] Z. B. Shi, et al., Plasma Sci. Technol. 20, 094007(2018).

[A13] X. R. Duan, et al., Nucl. Fusion 50, 095011 (2010).

[A14] Z. B. Shi, et al., Rev. Sci. Instrum. 85, 023510 (2014).

[A15] Y. G. Li, et al., Fusion Eng. Des. 137, 137 (2018).

[A16] D. L. Yu, et al., Nucl. Fusion 52, 082001 (2012).

[A17] B. Y. Zhang, et al., Nucl. Fusion Plasma Phys. 36, 289 (2016).

[A18] W. L. Zhong, et al., Rev. Sci. Instrum. 85, 013507 (2014).

[A19] S. P. Eury, et al., Phys. Plasma 12, 102511 (2005).

[A20] P. W. Shi, et al., Plasma Sci. Technol. 18, 708 (2016).